

PhD degree in Systems Medicine (curriculum in Molecular Oncology)

European School of Molecular Medicine (SEMM),

University of Milan and University of Naples “Federico II”

Settore disciplinare: BIO/11

**A zebrafish xenograft platform
for semi-quantitative analysis of
individual steps of the metastatic cascade**

Federica Ruscitto

European Institute of Oncology (IEO), Milan

Tutors: Prof. Pier Giuseppe Pelicci

European Institute of Oncology (IEO), Milan

PhD Coordinator: Prof. Saverio Minucci

Anno accademico 2020-2021

Siamo chimici, cioè cacciatori: nostre sono le “due esperienze della vita adulta” di cui parlava Pavese, il successo e l’ insuccesso, uccidere la balena bianca o sfasciare la nave; non ci si deve arrendere alla materia incomprensibile, non ci si deve sedere. Siamo qui per questo, per sbagliare e correggerci, per incassare colpi e renderli. Non ci si deve mai sentire disarmati: la natura è immensa e complessa, ma non è impermeabile all’ intelligenza; devi girarle intorno, pungere, sondare, cercare il varco e fartelo.

PRIMO LEVI, *Il sistema periodico*

Table of Contents

| | |
|---|------------|
| <i>Acknowledgments</i> | <i>IV</i> |
| <i>List of Abbreviations</i> | <i>V</i> |
| <i>Figures and Tables Index</i> | <i>VII</i> |
| 1. Abstract | 1 |
| 2. Introduction | 2 |
| 2.1 Breast cancer | 2 |
| 2.1.1 Epidemiology and classification | 2 |
| 2.1.2 Breast cancer heterogeneity | 4 |
| 2.2 The metastatic process | 7 |
| 2.2.1 Metastasis: general principles | 7 |
| 2.2.2 Dynamics of metastatic evolution..... | 12 |
| 2.2.3 Breast cancer metastatic progression | 14 |
| 2.2.4 Models of metastasis | 15 |
| 2.3 Zebrafish as a model of cancer and metastasis | 19 |
| 2.3.1 Zebrafish: an overview..... | 19 |
| 2.3.2 Cancer modeling approaches in zebrafish..... | 20 |
| 2.3.3 The zebrafish xenograft model..... | 24 |
| 2.3.4 Cell invasion and metastasis in zebrafish xenografts..... | 36 |
| 2.4 Aim | 38 |
| 3. Materials and Methods | 40 |
| 3.1 Animal care and handling | 40 |
| 3.2 Cell culture and manipulation | 41 |
| 3.2.1 Cell lines | 41 |
| 3.2.2 Vectors | 41 |
| 3.2.3 shRNA constructs | 43 |
| 3.2.4 Virus production | 43 |
| 3.2.5 Virus transduction | 44 |
| 3.3 The zebrafish xenograft assay | 45 |

| | |
|---|-----------|
| 3.3.1 Cell preparation | 45 |
| 3.3.2 Xenotransplantation | 45 |
| 3.3.3 Quantification of tumor implantation capacity | 47 |
| 3.3.4 Quantification of metastatic potential | 47 |
| 3.4 Zebrafish whole mount immunofluorescence | 49 |
| 3.5 Histological evaluation of primary tumors..... | 50 |
| 3.6 Imaging and quantification..... | 51 |
| 3.6.1 Stereomicroscopy | 51 |
| 3.6.2 Confocal microscopy | 51 |
| 3.6.3 Image analysis | 53 |
| 3.7 Drug treatment and efficiency evaluation | 53 |
| 3.8 Statistical analysis | 54 |
| 4. Results | 55 |
| 4.1 Establishment of a zebrafish xenograft model of human metastatic BC..... | 55 |
| 4.1.1 Experimental design | 55 |
| 4.1.2 Implantation and local growth are properties of the transformed phenotype | 56 |
| 4.1.3 MDA-MB-231 zebrafish xenografts display same proliferative properties and morphology as in mouse | 58 |
| 4.1.4 Dissemination of mammary cells in the zebrafish host is a property of the transformed phenotype | 61 |
| 4.1.5 Intravenous transplantation of MDA-MB-231 BC cells leads to the development of extravascular metastases in the zebrafish host | 63 |
| 4.2 Optimization of a set of quantitative parameters to analyze the different steps of BC metastatic progression | 68 |
| 4.2.1 Experimental design | 68 |
| 4.2.2 Incidence of metastasis | 69 |
| 4.2.3 Numbers of metastases | 70 |
| 4.2.4 Metastasis size | 71 |
| 4.2.5 Metastatic burden..... | 73 |
| 4.2.6 Frequency of metastasis initiating cells | 74 |
| 4.2.7 Metastasis proliferative index | 75 |
| 4.2.8 Metastasis outgrowth | 76 |
| 4.2.9 Summary | 77 |

| | |
|---|------------|
| 4.3 Zebrafish xenografts as <i>in vivo</i> platform to quantitatively test the pro-metastatic role of candidate genes in BC: a focus on ANGPTL4..... | 79 |
| 4.3.1 ANGPTL4 is not involved in PT implantation and growth | 80 |
| 4.3.2 ANGPTL4 is essential in the step of extravasation of metastatic cells..... | 82 |
| 4.3.2 ANGPTL4 silencing reduces the number of extravasated metastases but does not impact on their size | 84 |
| 4.3.3 ANGPTL4 is a determinant of metastatic burden..... | 87 |
| 4.3.4 ANGPTL4 does not impact on metastasis cell proliferation and outgrowth | 88 |
| 4.3.5 Summary | 90 |
| 4.4 <i>In vivo</i> validation of putative gene-dependencies of BC metastatic progression | 91 |
| 4.4.1 KCNQ1OT1 | 91 |
| 4.4.2 ITGB4 | 94 |
| 4.4.3 LY6E..... | 97 |
| 4.4.4 IFI6..... | 99 |
| 4.4.5 FST..... | 101 |
| 4.4.6 Summary | 103 |
| 4.5 Zebrafish xenografts as a pre-clinical platform for drug sensitivity studies.... | 104 |
| 4.5.1 Zebrafish <i>larvae</i> display drug sensitivity in a 3 day-long assay | 104 |
| 4.5.2. <i>In vivo</i> treatment with autophagy-inducer drugs reverts resistance of MDA-MB-231 BC to Paclitaxel | 106 |
| 5. Discussion..... | 108 |
| 6. References | 119 |

Acknowledgments

I would like to first and foremost thank my supervisors, Prof. Pier Giuseppe Pelicci and Dr. Enrica Migliaccio, who assisted me in the completion of my research project with their extraordinary support and mentorship. I would also like to thank my internal and external advisors, Dr. Stefano Casola and Dr. Rita Fior, for their helpful scientific guidance.

A special thanks to all the members of my laboratory for their precious support and in particular: Dr. Chiara Priami, who guided me with patience and passion since my master thesis internship and shared with me both highs and lows of the project; Giulia De Michele for technical assistance and positive encouragement; Dr. Niccoló Roda, for his generous friendship, his exceptional scientific contribution to this thesis and the many laughs we shared together; Giada Blandano and Alberto Dalmaso, who greatly helped me during the many hours spent at the microscope, and finally all the people who believed in my project, giving me the possibility to collaborate together, namely Dr. Cristina Moroni, Errico D'Elia, Dr. Valentina Gambino and Giorgio Pacecchi.

I also would like to thank all the researchers in the Department I had the opportunity to work with, establishing fruitful collaborations and sharing stimulating scientific discussions and in particular Andrea Castiglioni, Prof. Giuliana Pelicci, Daniela Osti, Dr. Brunella Costanza and Dr. Cecilia Toscani.

My research would have been impossible without the aid of the technological units of the Department and their staff, particularly Dr. Simona Rodighiero and Chiara Soriani for their assistance with image acquisitions and imaging data analysis; Dr. Giovanni Bertalot, Dr. Francesca Montani and Giovanna Jodice for their help with histology and histochemistry experiments.

A special thanks to Andrea, Stefano, Francesca, Chiara, Cecilia, Cristina, Giuseppe and Alessandro, with whom I shared science but also friendship, laughter, joys, thoughts, opinions, complaints, coffees, lunch breaks and several glasses of wine.

Last but not the least, I would like to thank all my friends and family for their precious encouragement throughout my research and in particular Lorenzo, without whose constant support I would not be able to overcome the hardest moments of my PhD journey.

List of Abbreviations

| | |
|-------------|---|
| ANGPTL4 | Angiopoietin-like 4 |
| ATCC | American Type Culture Collection |
| AVG | Average |
| BC | Breast Cancer |
| bp | Base pairs |
| CI | Confidence Interval |
| CisPt | Cisplatin |
| CHT | Caudal Hematopoietic Tissue |
| CRISPR/Cas9 | Clustered Regularly Interspaced Sort Palindromic Repeats/Cas9 |
| CSC | Cancer Stem Cell |
| CTC | Circulating Tumor Cell |
| CV | Caudal Vein |
| CVP | Caudal Vein Plexus |
| DA | Dorsal Aorta |
| DAPI | 4',6-diamidino-2-phenylindole |
| DLAV | Dorsal Longitudinal Anastomotic Vessel |
| DMEM | Dulbecco's Modified Eagle Medium |
| DoC | Duct of Cuvier |
| dpf | Days post-fertilization |
| dpi | Days post-injection |
| DTC | Disseminating Tumor Cell |
| E3 | Embryo water medium |
| ECM | Extra-Cellular Matrix |
| EMT | Epithelial-to-Mesenchymal Transition |
| ER | Estrogen Receptor |
| ER (stress) | Endoplasmic Reticulum (stress) |
| FST | Follistatin |
| GEMM | Genetically Engineered Mouse Model |
| GFP | Green Fluorescent Protein |
| H2B | Histone 2B |
| H&E | Hematoxylin and Eosin |
| HER2 | Human Epidermal growth factor Receptor 2 |
| hpf | Hours post-fertilization |
| IHC | Immunohistochemistry |
| IFI6 | Interferon alpha-Inducible protein 6 |
| I.I. | Intravenous Injection |
| ISV | Intersegmental Vessel |
| ITGB4 | Integrin subunit β 4 |
| KCNQ1OT1 | KCNQ1 Opposite Strand/Antisense Transcript 1 |
| KD | Knock-down |
| LY6E | Lymphocyte Antigen 6 family member E |
| MET | Mesenchymal-to-Epithelial Transition |
| MIC | Metastasis Initiating Cell |

| | |
|----------|---|
| mPDX | Mouse Patient-Derived Xenograft |
| MTD | Maximum Tolerated Dose |
| n | Number of samples |
| NK | Natural Killer |
| ns | Not significant (statistical analysis) |
| <i>p</i> | P value |
| PBS | Phosphate Buffer Saline |
| PBT | Phosphate Buffer Saline – 0.2% Triton |
| PBTT | Phosphate Buffer Saline – 0.2% Triton 0.2% Tween-20 |
| PBTw | Phosphate Buffer Saline – 0.05% Tween-20 |
| PFA | Paraformaldehyde |
| PT | Primary Tumor |
| PR | Progesterone Receptor |
| PTU | N-Phenylthiourea |
| PVS | Peri-Vitelline Space |
| RFP | Red Fluorescent Protein |
| RT | Room Temperature |
| SC | Stem Cell |
| scRNAseq | Single Cell RNA Sequencing |
| SEM | Standard Error of the Mean |
| shRNA | Short hairpin RNA |
| S.I. | Subcutaneous Injection |
| T-ALL | T-cell Lymphoblastic Leukemia |
| TEAZ | Transgene Electroporation in Adult Zebrafish |
| TEM | Trans-Endothelial Migration |
| TGFβ | Transforming Growth Factor-β |
| TME | Tumor Microenvironment |
| TNBC | Triple-Negative Breast Cancer |
| UPR | Unfolded Protein Response |
| VEGF | Vascular Endothelial Growth Factor |
| XT | Xenotransplantation |
| YS | Yolk Sac |
| zPDX | Zebrafish Patient-Derived Xenograft |

Figures and Tables Index

Introduction

Figure 1, page 2

Cancer incidence and mortality in the female population.

Figure 2, page 4

A conceptual representation of tumor heterogeneity.

Figure 3, page 8

Schematic representations of the key steps associated with successful carcinoma metastasis.

Figure 4, page 13

A conceptual representation of the lineage tracing approach.

Figure 5, page 18

Detection of metastases in the mouse model.

Figure 6, page 20

Zebrafish life cycle and larval anatomy.

Figure 7, page 28

Injection sites for cell xenotransplantation in the 2 dpf zebrafish *larva*.

Figure 8, page 31

Use of transgenic reporter zebrafish strains to study interactions with tumor microenvironment.

Figure 9, page 36

Xenotransplantation in adult zebrafish

Table 1, page 22

Transgenic zebrafish models of cancer.

Table 2, page 25

Cancer modeling approaches in zebrafish.

Table 3, page 35

Comparison between patient-derived avatar models.

Materials and methods

Figure 1, page 41

The Tet-Off-H2B-GFP construct.

Figure 2, page 42

The pRSI17-U6-sh-HTS6-UbiC-TagGFP2-2A-Puro plasmid.

Figure 3, page 47

Schematic representation of *larvae* XT procedure.

Figure 4, page 52

Agarose mounting immobilization method for live imaging of zebrafish xenografts.

Table 1, page 43

List of shRNA oligonucleotides used for functional gene validation.

Table 3, page 52

List of the microscopes and their applications.

Results

Figure 1, page 56

Establishment of a rapid zebrafish xenograft assay to study human BC.

Figure 2, page 57

The zebrafish host sustains implantation and growth of only malignant cells.

Figure 3, page 59

MDA-MB-231 human BC cells are viable and actively proliferate in zebrafish xenografts.

Figure 4, page 60

Zebrafish xenografts conserve the same histochemical profile described for MDA-MB-231 cells, showing no differences respect to the murine model.

Figure 5, page 62

MDA-MB-231 human BC cells disseminate outside the PT over time in zebrafish xenografts.

Figure 6, page 64

Intravascular transplantation of MDA-MB-231 human BC cells induce extravasation and metastasis formation in zebrafish xenografts.

Figure 7, page 65

Visual assessment of BC metastatic progression of MDA-MB-231 human BC cells in zebrafish xenografts.

Figure 8, page 66

MDA-MB-231 human BC extravasated cells proliferate at the metastatic site.

Figure 9, page 67

MDA-MB-231 metastasis localization and architecture.

Figure 10, page 68

Optimization of two distinct assays to evaluate metastasis formation.

Figure 11, page 70

Incidence of metastasis formation in zebrafish xenografts for MDA-MB-231 human BC cells.

Figure 12, page 71

Average number of metastasis detected in zebrafish xenografts transplanted with MDA-MB-231 human BC cells

Figure 13, page 73

Distribution of MDA-MB-231 metastases according to their size.

Figure 14, page 74

Human BC MDA-MB-231 metastatic burden in zebrafish xenografts.

Figure 15, page 75

Frequency of metastasis initiating cells in zebrafish xenografts for human BC MDA-MB-231 cell line.

Figure 16, page 76

Frequency of proliferating MDA-MB-231 cells at the metastatic site in zebrafish xenografts.

Figure 17, page 76

Human BC MDA-MB-231 metastatic outgrowth in zebrafish xenografts.

Figure 18, page 81

Analysis of PT engraftment and growth in zebrafish xenografts upon ANGPTL4 silencing.

Figure 19, page 83

Incidence of metastasis formation in zebrafish xenografts for MDA-MB-231 cells upon ANGPTL4 silencing.

Figure 20, page 85

Number of MDA-MB-231 metastases in zebrafish xenografts upon ANGPTL4 silencing.

Figure 21, page 86

Frequency of metastasis initiating cells for MDA-MB-231 cells upon ANGPTL4 silencing.

Figure 22, page 87

Size distribution of MDA-MB-231 metastases in zebrafish xenografts upon ANGPTL4 silencing.

Figure 23, page 88

Metastatic burden of MDA-MB-231 BC cells in zebrafish xenografts upon ANGPTL4 signaling.

Figure 24, page 89

Metastasis proliferation and outgrowth of MDA-MB-231 metastases in zebrafish xenografts upon ANGPTL4 silencing.

Figure 25, page 92

Analysis of PT growth in zebrafish xenografts upon KCNQ1OT1 silencing.

Figure 26, page 93

In vivo validation of metastatic behavior of MDA-MB-231 cells upon KCNQ1OT1 silencing in zebrafish xenografts.

Figure 27, page 95

Analysis of PT growth in zebrafish xenografts upon ITGB4 silencing.

Figure 28, page 96

In vivo validation of metastatic behavior of MDA-MB-231 cells upon ITGB4 silencing in zebrafish xenografts.

Figure 29, page 98

In vivo analysis of PT growth and metastatic behavior of MDA-MB-231 cells upon LY6E silencing in zebrafish xenografts.

Figure 30, page 100

In vivo analysis of PT growth and metastatic behavior of MDA-MB-231 cells upon IFI6 silencing in zebrafish xenografts.

Figure 31, page 102

In vivo analysis of PT growth and metastatic behavior of MDA-MB-231 cells upon FST silencing in zebrafish xenografts.

Figure 32, page 105

Human MDA-MB-231 BC cells display chemosensitivity in just 3 days in the zebrafish host.

Figure 33, page 107

Autophagy-stimulating treatments enhance TNBCs sensitivity to Paclitaxel.

Table 1, page 78

Summary table of quantitative parameters describing human BC metastatic progression in zebrafish xenografts.

Table 2, page 90

Validation of ANGPTL4: summary of quantitative analyses.

Table 3, page 132

Summary table of *in vivo* pro-metastatic genes validation in the zebrafish model.

1. Abstract

Metastatic disease represents the main cause of most cancer-related deaths, yet this process remains one of the most enigmatic aspects of cancer biology. Metastatic progression includes multiple distinct phases, such as invasion, intra- and extravasation, seeding at distant sites, micro-metastasis formation and metastatic outgrowth. Only a deep understanding of each of these steps may offer novel targets to be exploited in a clinical setting. Emerging evidence suggests that metastatization is not a genetically selected trait, but the result of phenotypic adaptation to the unfavorable microenvironmental conditions which cancer cells are exposed to (*e.g.* hypoxia or low nutrients in the primary site or bloodstream). Functional genomic and differential expression screenings allowed to identify numerous potential metastasis genes, that need to be prioritized and validated with appropriate pre-clinical *in vivo* systems, ideally able to recapitulate and explore the entire metastatic cascade. Mouse models present several critical limitations, including the difficulty to visualize and quantify the metastatic phases, except in sophisticated experimental contexts. Therefore, I propose xenotransplantation of human cancer cells in zebrafish *larvae* as a system to evaluate primary tumor implantation and growth and to quantitatively dissect metastatic progression, with the purpose of mapping gene functions in the multistep cascade. First, I set up a robust protocol for subcutaneous and intravenous transplantation of fluorescently labeled cells in zebrafish *larvae*, using the metastatic breast cancer (BC) cell line MDA-MB-231 and non-tumorigenic MCF10A mammary cells as a control. MDA-MB-231 cells survive, proliferate and disseminate in the zebrafish host, developing tumors with conserved histological features and originating extravascular metastases in just 4 days. Using a zebrafish strain with fluorescent vasculature and visually following each fish by live microscopy, I optimized a set of analytical tools to quantitatively investigate incidence, numerosity, size and proliferative index of metastases, as well as measuring frequency of metastasis initiating cells and the severity of metastatic progression. Secondly, I challenged the zebrafish platform by transplanting MDA-MB-231 cells separately interfered for 6 genetic targets, previously identified in our laboratory, as potential novel mediators of BC metastasis. I successfully validated the contribution of 5 out of 6 of these genes in BC metastatization, attributing a specific role in the metastatic cascade for each of them. The identification and *in vivo* validation of this stage-specific determinants of metastasis offers potential new targets to halt metastatic disease, to be further explored in future pre-clinical and clinical studies, paving the way to novel and effective anti-metastatic therapeutic approaches.

2. Introduction

2.1 Breast cancer

2.1.1 Epidemiology and classification

Cancer – defined as an abnormal and malignant accumulation of cells in a specific anatomical site derived from uncontrolled cell divisions – is one of the major causes of death worldwide. With regard to the female population, breast, lung and colorectal cancers are the most commonly diagnosed malignancies, representing the second leading cause of mortality for women in Western countries [Torre *et al.* 2017; Siegel, Miller and Jemal, 2020]

Breast cancer (BC), in particular, is the most frequent (~30% of all new tumor cases in 2020 in female US population) and is responsible for ~15% of cancer-related deaths (Figure 1). BC incidence strongly depends on the ethnicity and the age of the subject, being higher among Black women (who also display a worse prognosis and tend to be diagnosed at younger age respect to other ethnicities) and over 60 years of age [Siegel, Miller and Jemal, 2020]. Several risk factors are associated to the development of this disease, such as: BC family history, often accompanied by inherited mutations in BRCA1 and BRCA2 genes; age at menarche and age at menopause; childbirth; hormone therapies (*i.e.* oral contraceptives and menopausal hormone replacement) and life style factors like obesity, smoke, alcohol consumption and physical inactivity. On the contrary breastfeeding exerts a protective effect [Torre *et al.*, 2017].

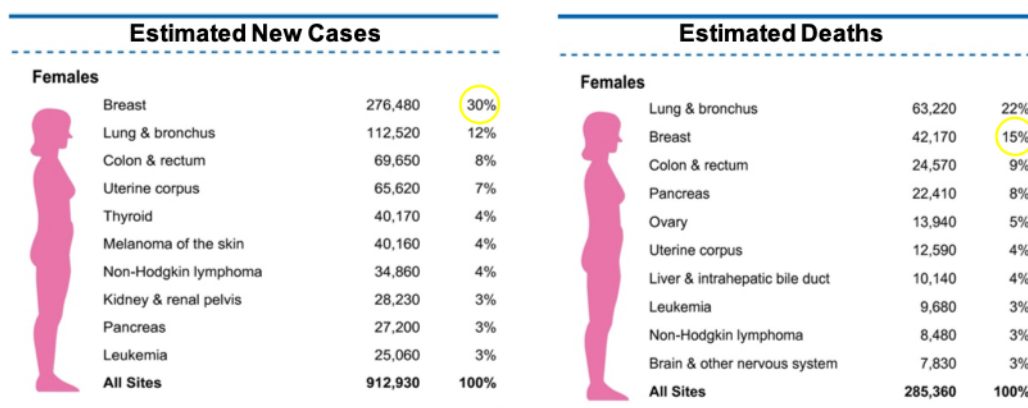


Figure 1 | Cancer incidence and mortality rate in the female population (modified from Siegel, Miller and Jemal, 2020).

BC develops from the tumorigenic transformation of the epithelial cells that compose the ducts and lobules of the mammary gland and is considered a highly heterogeneous

disease that can be classified on the basis of its molecular, histological and pathological characteristics [Malhotra *et al.*, 2010].

Molecular classification

Molecular classification allows to distinguish four distinct BC subtypes: luminal A, luminal B, HER2 and triple-negative, so called on the basis of the expression of specific biomarkers, namely estrogen (ER) and progesterone (PR) receptors, human epidermal growth factor 2 receptor (HER2) and the proliferative marker Ki67. This kind of classification is useful to stratify patients, in order to tailor effective therapeutic regimens according to the patient specific subtype.

Luminal A and B are the most frequent subtypes (50-60% of patients) and express both ER and PR, with luminal A showing the highest levels of expression. On the contrary, luminal B tumors could also express HER2 and display a higher proliferation rate respect to luminal A. Both these subtypes have a good prognosis and can be treated with hormone therapies that prevent estrogen signaling or synthesis (*e.g.* tamoxifen). HER2 tumors (15-20% of patients) overexpress HER2, lack hormone receptors, are highly proliferative and have an intermediate prognosis. HER2 patients are eligible for specific therapies that target HER2 signaling, such as trastuzumab and lapatinib. Triple-negative breast cancer (TNBC), instead, is less frequently diagnosed (10-20% of patients), is highly proliferative and totally lacks ER, PR and HER2 expression, being the subtype with the worst patient prognosis. Chemotherapy (*i.e.* adriamycin, cyclophosphamide and taxol) is the unique available treatment option for TNBC, since the lack of biomarkers prevents the usage of hormonal and targeted therapies. Therefore, TNBC represents the most difficult subtype to cure [Prat *et al.*, 2010; Malhotra *et al.*, 2010].

Histological classification

Histological classification divides BCs into two categories: *in situ* and invasive tumors. *In situ* tumors are located within the mammary gland and are classified as ductal carcinomas when they develop from the epithelial cells of the mammary ducts and as lobular carcinomas when they arise from the secretory lobules. Invasive ductal carcinomas and invasive lobular carcinomas are their invasive counterparts and are able to infiltrate locally in the mammary tissue and metastasize to distant secondary sites [Malhotra *et al.*, 2010].

Pathological classification

Pathological classification defines two clinical features of BC: grade and stage. Comparing the morphology of cancer cells and normal breast epithelial cells, BCs can be

divided into well differentiated (G1, low grade), moderately differentiated (G2, intermediate grade) and poorly differentiated tumors (G3, high grade). A higher grade correlates with the progressive loss of normal mammary cell features and bad prognosis [Elston and Ellis, 1991]. BCs are also categorized into five different stages, according to the TNM classification, that takes into consideration the size of the primary tumor (T), the spreading to regional lymph nodes (N) and the presence of metastases (M). Stage 0 defines pre-cancerous lesions, whereas stage V includes metastatic tumors with bad prognosis, passing through intermediate stages characterized by the progressive increment of primary tumor size and nodal involvement [Giuliano, Edge and Hortobagyi, 2018].

2.1.2 Breast cancer heterogeneity

BC is a highly heterogeneous disease that, as already anticipated, presents tremendously different individual manifestations. The differences among different patients constitute the so called “inter-tumor heterogeneity”, which deeply influences treatment and prognosis. Inter-patient diversity coexists with “intra-tumor heterogeneity”, defined as the set of genetic and phenotypic differences within a single patient’s tumor or metastasis. Intra-tumor heterogeneity depends on both microenvironmental factors (*e.g.* hypoxia, vascularization, interaction with stromal components and immune infiltration) and from intrinsic parameters of the cancer cells themselves, including genetic, transcriptional and metabolic factors.

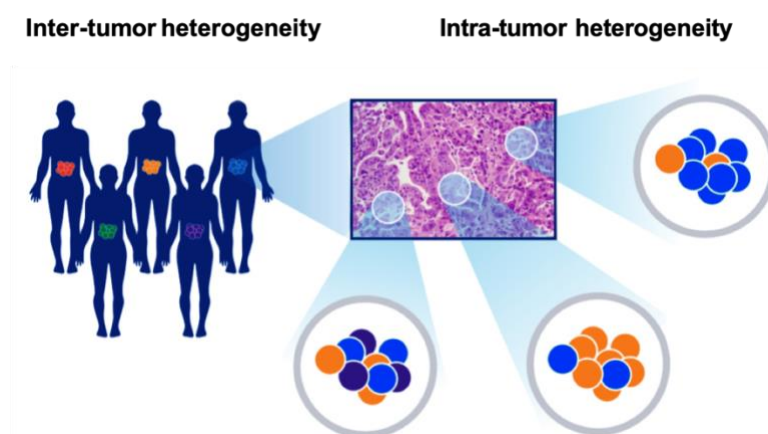


Figure 2 | A conceptual representation of tumor heterogeneity. Inter-tumor heterogeneity comprises the differences among tumors of different patients. Intra-tumor heterogeneity refers to the intrinsic genetic and phenotypic variations among the cells of a single patient. Colors denote the presence of cellular clones with different features.

Notably, intra-tumor heterogeneity represents a hurdle for BC cure, since it confers to cancer cells the ability to adapt to constantly changing conditions, often resulting in

metastatic progression or development of chemotherapy resistance [Lüönd, Tiede and Christofori, 2021]. This condition of phenotypic instability determined by the great reactivity of cancer cells to both external cues and internal stochastic changes is called cell plasticity. Cellular plasticity is at the base of many cancer processes, such as metastasis, that will be extensively described in paragraph 2.2.

Intra-tumor heterogeneity models

We can refer to BC – as well as to other tumors – as a polyclonal system composed by heterogeneous clones, whose genesis from a single “cell-of-origin” can be described by two models: the clonal evolution and the hierarchical (or cancer stem cells, CSCs) model.

The clonal evolution model is based on genetic heterogeneity and proposes that cancer cells derive from a single mutated cell, acquiring distinct additional mutations during tumor progression. This process leads to the development of a tumor mass originated by a single clone but characterized by multiple subpopulations with specific mutations, that have the ability to further proliferate and mutate [Nowell, 1976].

Hierarchical model is based on phenotypic heterogeneity and postulates a hierarchical organization of cancer cells within a tumor, with few self-renewing tumorigenic CSCs at the apex and with partially (*i.e.* progenitors) and full differentiated amplifying cells to constitute the tumor bulk. CSCs, analogous to normal stem cells, have self-renewal capacities and fuel tumor growth by giving origin to phenotypically diverse progenies of differentiated proliferating cells, characterized by distinct gene expression patterns [Martelotto *et al.*, 2014].

The two models are not mutually exclusive and both contribute to BC heterogeneity. For this reason, an integration of the two models that takes into consideration both genetic and phenotypic diversity has been suggested. According to this view, cancer has a hierarchical structure in which CSCs are genetically distinct by the presence of independent oncogenic mutations, subsequently accumulated in their progeny [Clevers, 2011].

Genetic heterogeneity

The mutational landscape of BC is highly heterogeneous. Genomic analysis of different regions of the same tumor and single-cell DNA analysis demonstrated that all subtypes of BC are composed by multiple clones with different mutational profiles (point mutations and copy number variations) that also occupy distinct areas of the primary tumor. This spatial confinement suggests that genetic alterations can occur later in cancer progression and only in a specific subpopulation of cells defining, as a consequence, morphologically diverse portions within the whole tumor mass [Geyer *et al.*, 2010; Patani *et*

al., 2011]. For instance, it has been reported that HER2 tumors present spatial heterogeneity in terms of copy number variations, with areas characterized by higher HER2 amplification respect to others. This kind of tumors poorly respond to trastuzumab, compared to patients with homogeneous levels of HER2 expression [Lee *et al.*, 2014].

Transcriptional heterogeneity

Similarly to what observed for genetic heterogeneity, different regions within a tumor strikingly vary in gene expression patterns. Single-cell sequencing of both murine and human BCs enabled to transcriptionally analyze thousands of cells coming from the same primary mass and to identify clusters of cells characterized by distinct phenotypes, independently from the surrounding cells. Specific cell clusters can indeed express genes associated with proliferation, apoptosis, hypoxia response, epithelial-to-mesenchymal transition (EMT) or other stress response pathways. This transcriptional intra-tumor heterogeneity determines the coexistence in the same mass of both aggressive and highly proliferating cells and dormant-like, slowly proliferating cells that upregulate stress response, hypoxia and EMT programs [Yeo and Guan, 2017; Jackson *et al.*, 2020]. Different regions of the same breast tumor can also differ in the expression of specific membrane markers (*e.g.* EpCAM, CD49f and CD24), ultimately leading to portion of cancerous tissue with either epithelial (EpCAM⁺/CD49f⁺/CD24⁺) or mesenchymal (EpCAM⁻/CD49f⁺/CD24⁻) phenotypes [Keller *et al.*, 2010]. These findings regarding spatial transcriptional and genetic heterogeneity suggest that a single biopsy could be misleading, since it does not depict the disease in its entire complexity, leading to incomplete diagnosis.

Metabolic heterogeneity

BC cells have a significant variable oxygen consumption rate with respect to normal breast epithelial cells from the same patient [Hai *et al.*, 2019]. In addition, cells within the same breast tumor display a hybrid metabolism depending on oxygen availability: normoxic cells preferentially rely on oxidative phosphorylation for their metabolism, whereas hypoxic cells – mostly located in the non-vascularized core of the tumor – activate glycolysis [Vaupel *et al.*, 2005]. It has been also reported that breast CSCs upregulate glycolysis, mitochondrial proteins and protein anabolism enzymes respect to the rest of the tumor [Vlashi *et al.*, 2014].

Heterogeneity as a determinant of drug resistance and metastasis

BC heterogeneity poses a major challenge for clinicians in diagnosis, prognosis and therapy definition. The presence of a resistant cell subpopulation can severely compromise therapy efficacy: following a treatment that eradicates the sensitive cells that compose the

vast majority of the tumor, drug-resistant clones might persist and lead to relapse. Moreover, resistant subset of cells often present metastatic traits (as they express EMT genes), overall worsening the patient's clinical outcome.

Regarding genetic heterogeneity and drug resistance, it has been already mentioned the limited trastuzumab efficacy associated with variable HER2 copy number. Additionally, trastuzumab is also ineffective for tumor subpopulations with activating mutations of the PI3K pathways downstream to HER2 [Berns *et al.*, 2016]. In turn, cells can become refractory also to PI3K inhibitors following the genetic loss of PTEN, canonical antagonist of PI3K [Juric *et al.*, 2015]. Drug resistant phenotype is also closely associated to cell transcriptional plasticity. In both luminal and TNBC, chromatin remodeling events rapidly modify the epigenome allowing the hyperactivation of survival pathways upon drug treatment. Therefore, the use of chromatin remodeling inhibitors may improve the efficacy of traditional therapies, preventing transcriptional heterogeneity [Risom *et al.*, 2018].

Intra-tumor heterogeneity also correlates with BC metastatic spreading. The genetic heterogeneity of hundreds of BC patients of different subtypes has been quantified in terms of mutational (whole exome sequencing) and copy number variation profiles within the TCGA project, showing that the higher is the patient's intra-tumor heterogeneity, the higher is the incidence of distant metastases and bad prognosis [Mroz and Rocco, 2017]. BC progression is also fostered by phenomena of cooperative interaction among heterogeneous clones, known as clonal cooperativity. Minor BC cell clones can drive tumor progression stimulating the growth of all the other cancer cells, through the release of paracrine factors (*e.g.* growth factors and cytokines) able to increase vessel permeability or to recruit pro-metastatic neutrophils. Strikingly, in case the minor clone is outcompeted by the others, the whole mass eventually collapses [Polyak and Marusyk, 2014].

2.2 The metastatic process

2.2.1 Metastasis: general principles

Metastasis is a well-known hallmark of cancer, defined as the development of one or more secondary malignant growths in distant sites respect to the primary tumor mass. Approximately 90% of all cancer deaths are caused by the metastatic spreading of primary tumors, representing a major therapeutic challenge in oncology. However, the molecular mechanisms underlying this complex event are still poorly understood. Metastatic progression is described by a multi-step process known as metastatic cascade, that is

characterized by the following serial events: *i*) EMT and local invasion of the primary tumor in the surrounding tissues; *ii*) intravasation and survival in the circulatory or lymphatic system; *iii*) extravasation through the vascular endothelium into the parenchyma of distant tissues or organs; *iv*) seeding of small cell colonies in such parenchyma, called micro-metastases; *v*) the adaptation of micro-metastases to the foreign microenvironment, facilitating proliferation and formation of clinically detectable lesions [Lambert, Pattabiraman and Weinberg, 2017]. This complex mechanism can be conceptualized into two major phases: the first is the pre-colonization phase, that implies the physical translocation of cancer cells from the primary mass to a distant microenvironment, occurring in a timescale of minutes to hours; the second one is the metastatic colonization phase, which may comprehend a latency period of years, involving a series of events that leads to the formation of an overt metastasis [Massagué and Obenauf, 2016].

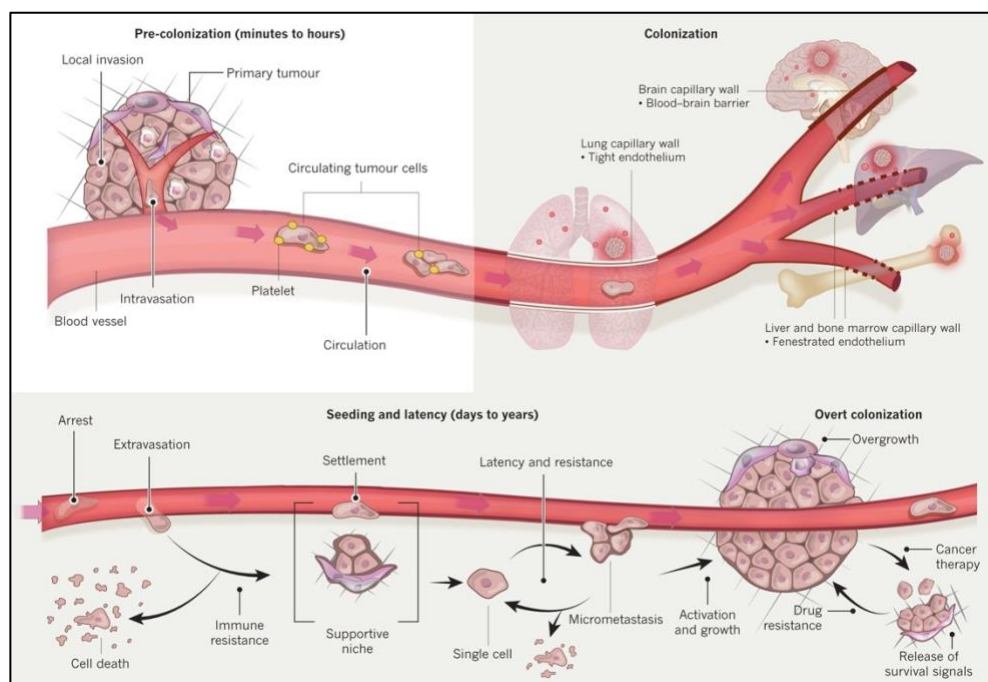


Figure 3 | A detailed view of the metastatic cascade of a solid tumor, divided into pre-colonization phase, which implies local invasion and intravasation, and colonization phase, which comprises the series of events from cell extravasation to the onset of a clinically detectable metastatic lesion (from Massagué and Obenauf, 2016).

Epithelial-to-mesenchymal transition

In order to escape from the primary tumor, cancer cells must acquire the ability to migrate and invade. With regard to carcinomas, epithelial-to-mesenchymal transition (EMT) constitutes the critical initial step of the metastatic cascade, leading to the loss of epithelial features of cancer cells and subsequent acquisition of migratory traits. EMT is a biological program normally exerted by cells during embryonic development and in the repair of adult

epithelial tissues. EMT determines epithelial cells to lose their polarity and break down their cell-to-cell and cell-to-basal lamina junctions, while assuming mesenchymal phenotypes, such as spindle-shape morphology, lack of polarization and migratory capacity. In the pathological context, cancer cells undergo EMT after clonal outgrowth and establishment of a localized tumor mass, gaining metastatic capabilities, such as invasiveness, resistance to apoptosis and the ability to degrade the extracellular matrix (ECM).

EMT is commonly triggered by exogenous paracrine signals (*e.g.* TGF β s, Wnt/ β -catenin signaling, Notch signaling and interleukins) coming from the “reactive” tumor-associated stroma – composed by fibroblasts, myofibroblasts, endothelial and immune cells – that activates master transcription factors, such as SNAIL, SLUG, TWIST and ZEB1. Once activated, these transcription factors orchestrate a number of distinct molecular processes that involve loss of E-cadherin expression, the acquisition of specific mesenchymal markers (*e.g.* N-cadherin, fibronectin and vimentin), cytoskeleton reorganization and production of ECM-degrading enzymes, leading to profound morphological changes. However, these changes are reversible, as demonstrated by the occurrence of the opposite process, the mesenchymal-to-epithelial transition (MET), that occurs when migratory mesenchymal cells have reached their destination [Kalluri and Weinberg, 2009].

Some studies have also reported that EMT endows cells with CSC-like features, implying that the stem-cell state is an integral part in the development of metastases. Mani and colleagues observed that EMT induction in immortalized human mammary epithelial cells results in the acquisition of stem-cell markers and the capacity to form mammospheres (a property of mammary epithelial stem cells) and to differentiate into duct-like structures. On the other hand, stem-like cells isolated from mammary glands and carcinomas express EMT markers, suggesting that CSCs are not always distinct entities but cancer cells can transiently acquire stem cell-like features as a consequence of EMT [Mani *et al.*, 2008]. In addition, it has been reported that the acquisition of a mesenchymal phenotype is also associated to an increased resistance of cancer cells to cytotoxic treatments, including chemo- and radiotherapy [Kurrey *et al.*, 2009].

Intravasation and circulating tumor cells

During carcinoma metastatic progression, individual or clusters of invasive cells with mesenchymal properties enter the vasculature of either neighboring normal tissues or newly formed vessels within the tumor itself. Blood and lymphatic vessels provide highways for cell distribution to secondary organs. In fact, the first clinical indication of metastatic progression and poor prognosis is often the presence of cancer cells in the draining lymph

nodes close to the primary tumor site. Despite the early nodal involvement, cancer cells transfer to distant regions seems to occur almost entirely via hematogenous dissemination, while lymph nodes represent only temporary “pausing” sites or end points for cancer cells [Chambers, Groom and MacDonald, 2002].

Circulating tumor cell (CTC) fate is strongly influenced by the stressors and the interactions they experience while in transit. CTCs encounter multiple physical obstacles, such as hydrodynamic flow, shear forces, oxidative stress and loss of cellular attachment to a substrate, the latter being the cause of a specific program of cell death named anoikis. CTCs are particularly resistant to apoptosis and anoikis, reflecting the heightened resistance to programmed cell death typical of cells that have undergone EMT. CTCs are also vulnerable to the attacks of the immune system, particularly to Natural Killer cells (NK) that, once targeted, proceed to CTCs rapid clearance [Lambert, Pattabiraman and Weinberg, 2017].

While in circulation, cancer cells also establish interactions with several cell types that promote their survival and extravasation. CTCs attract and associate with platelets, which exert a protective role from the insults of the immune system: by the formation of a protective shield around the cell, in fact, platelets mask CTCs from the action of NK cells [Palumbo *et al.*, 2007]. In addition, signaling between CTCs and platelets may prevent MET and the subsequent loss of CTCs invasive traits [Labelle *et al.*, 2011]. Neutrophils promote CTCs survival too via physically entrapment and, similarly to platelets, they inhibit the elimination of CTCs by NK cells [Spiegel *et al.*, 2016].

CTCs anatomical dissemination and homing to a specific organ are strongly influenced by circulatory patterns and structural differences in the capillary wall of each organ. Metastatic tropism is then considered as a passive process, dependent more on vessels layout, rather than on cancer cell biological properties [Chaffer and Weinberg, 2011].

Extravasation

The mechanical entrapment of cancer cells in the capillary bed of a secondary organ causes CTCs to arrest. CTCs may extravasate and infiltrate the foreign organ or proliferate intra-luminally, forming emboli that may eventually cause the rupture of the vessel in which they are lodged, enabling direct access to the tissue parenchyma. As anticipated, vessel configuration strongly contributes to determine where cancer cells will extravasate. As an example, the fenestrated sinusoid capillaries of liver and bone marrow facilitate passive CTCs extravasation, accounting for the high incidence of liver and bone metastases. The passage through the tight junctions of the endothelium of lung capillaries, instead,

necessitates the action of specific “extravasation programs” and complex interactions with other cell types [Chaffer and Weinberg, 2011].

Extravasation requires cancer cells to pass through the endothelial wall via a process called trans-endothelial migration (TEM) [Reymond, d'Água and Ridley, 2013]. In many cases TEM is mediated by platelets and components of the innate immune system. Platelets associated with CTCs trigger TEM by releasing transforming growth factor- β (TGF β) or enhancing vasculature wall permeability through the secretion of adenine nucleotides [Schumacher *et al.*, 2013]. Moreover, the physical interaction of platelets with endothelial cells mediated by selectins is important for the adhesion of CTCs-platelets clusters to the vessel [Köhler *et al.*, 2010].

Similarly, neutrophils – which are recruited by platelet-derived chemokines – adhering to the vessel wall, provide the cells with a physical dock and facilitate their extravasation through the secretion of various metalloproteinases [Spicer *et al.*, 2012; Spiegel *et al.*, 2016]. Also monocytes play a role in cancer cells extravasation. Inflammatory monocytes – which may differentiate into metastasis-associated macrophages – are recruited in response to the release of CCL2 cytokine by carcinoma cells, facilitating vascular permeability, extravasation and seeding in the organ parenchyma [Qian *et al.*, 2011].

In addition to microenvironmental signals, cancer cells undergo TEM via the expression of autocrine enhancers of cell-motility and mediators of vascular permeability, including epiregulin, VEGF, MMPs, COX2 and ANGPTL4 [Massagué and Obenauf, 2016]. In particular, ANGPTL4 (angiopoietin-like 4) expression is induced by stromal TGF β and primes the extravasation of BC cells in the lungs via the disruption of vascular integrity and TEM induction [Padua *et al.*, 2008].

Metastatic colonization

The development of clinically detectable metastatic lesions represents the final and most complex step in the malignant progression of a tumor. Colonization is thought to be a bottleneck of metastasis, as many cancer cells disseminate, but only the 0,01% manages to form metastases [Chambers, Groom and MacDonald, 2002]. The inefficiency of metastatic colonization is sustained by clinical observations. A great number of people who have been successfully treated for their primary tumor never show a relapse after a long period of latency: these patients may harbor a reservoir of indolent disseminated tumor cells (DTCs) or micro-metastatic clusters in distant organs and are considered to have asymptomatic minimal residual disease. For certain type of carcinomas, such as BC, this condition may last even for decades. Colonization inefficiency is due to the fact that cancer cells, once infiltrated in a tissue parenchyma, undergo apoptosis, clearance by NK and cytotoxic T cells

or enter in a quiescent state called dormancy. Such events are determined by the fact that DTCs are poorly adapted to a new and unfavorable microenvironment, which lacks all those familiar ECM constituents, stromal cells, signaling factors and mitogenic cues that had sustained their growth in the primary tumor site [Massagué and Obenauf, 2016].

Despite its biological and clinical relevance, little is known about the mechanisms that trigger and sustain dormancy in the metastatic context, mostly because of the difficulty to study metastatic latency with current experimental models. However, it has been demonstrated in mouse xenografts that members of the TGF β and BMP family, as well as factors present in the peri-vascular niche (*i.e.* the microenvironment surrounding the vasculature where DTC clusters reside) play a role in promoting dormancy [Gao *et al.*, 2012; Ghajar *et al.*, 2013].

Successful colonization assumes that DTCs exit from dormancy, sense and respond to survival and proliferative stimuli, escape immune-surveillance, recruit the necessary supporting stroma and expand till macro-metastasis. To do this, disseminated tumors must possess at least two pre-requisites: *i*) the capacity to seed and maintain a population of CSCs, responsible to re-initiate tumor expansion and *ii*) the ability to thrive in a hostile microenvironment through a program of organ-specific phenotypic adaptation [Massagué and Obenauf, 2016]. Adaptive responses, with regard to BC, will be covered in the paragraph 2.2.3.

2.2.2 Dynamics of metastatic evolution

Interestingly, metastatic progression cannot be considered a genetically-selected trait. This means that no genetic mutations are specifically correlated with metastatic progression. Mutational landscapes of primary tumors and metastases, in fact, are largely overlapping. Metastasis-restricted alterations are exclusively described as passenger mutations (*i.e.* mutations that do not confer selective advantages to cancer cells), suggesting that the genetic alterations that drive the completion of the metastatic cascade are already present in the genome of the CTCs detached from the primary mass, during the early steps of the process [Aftimos *et al.*, 2021].

The high genetic similarity between primary tumors and metastases suggests a polyclonal origin of metastases for a variety of cancer types, where clusters of genetically heterogeneous cells enter the circulation, colonize distant organs and generate a secondary mass similar to the primary tumor [Naxerova and Jain, 2015].

Lineage tracing

Implicit in the aforementioned findings is the notion that genetic heterogeneity displays a minor role in metastatic progression, whereas epigenetic and transcriptional alterations, resulting in distinct phenotypic changes, give a strong contribution to the process. The nature of such changes still remains obscure, therefore their identification represents a compelling clinical need.

Phenotypic determinants can be exclusively studied tracking the cells that moved from the primary tumor towards distant organs by lineage tracing technologies. Lineage tracing consists in the identification of the progeny of a single cell: in the context of a transplantable model of metastasis (see paragraph 2.2.4), cancer cells are engineered in such a way that each cell is identified by a distinct barcode, that is propagated to the daughter cells, generating a clone. Each clone is distinguished from the others on the basis of the barcode [Kretzschmar and Watt, 2012]. Current lineage tracing approaches are based on DNA barcodes that integrate into the genome of the cells, allowing to discriminate a large number of independent clones, with respect to the specific DNA sequence they carry, and to analyze them with single-cell omics techniques [Wagner and Klein, 2020].

Lineage tracing approaches have been applied to study BC progression and demonstrated that BC metastases, yet polyclonal, show specific over-represented clones, present in all metastases regardless of the organ. These clones, on the contrary, are under-represented in the matched primary tumor. This suggests that some clones, although responsible for the process of metastasis, are kept in a slow-proliferative state in the primary tumor and do not contribute to its fitness [Echeverria *et al.*, 2018].

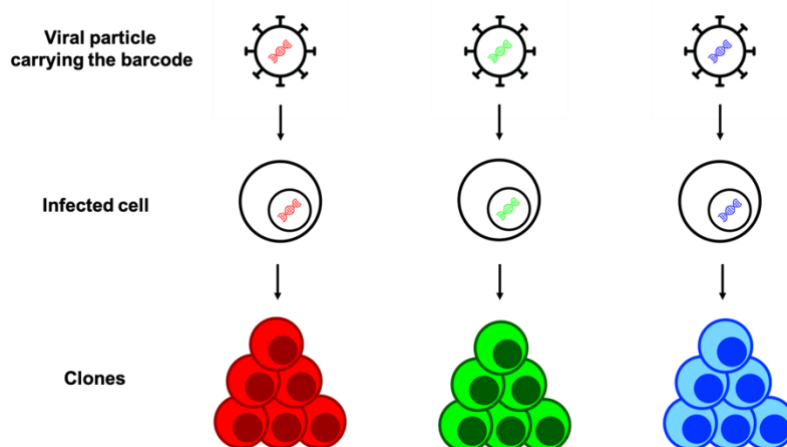


Figure 4 | In lineage tracing experiments, a cellular population is transduced with viral particles carrying distinct barcodes. Cells stably propagate the barcode to the offspring, thereby generating distinct clones. Clones are discriminated on the basis of the barcode (in distinct colors).

2.2.3 Breast cancer metastatic progression

Despite the relevant advances in diagnosis and therapy, metastatic BC remains in most cases incurable. Metastatic disease, in fact, represents the primary cause of mortality for BC patients, with a 5-year survival rate of ~27% [Torre *et al.*, 2017]. Approximately 6% of women have metastatic cancer when they are first diagnosed, while the incidence of metastatic recurrence is estimated between 20-30% [Howlader *et al.*, 2019]. BC preferentially metastasizes to bones, liver, lung and brain as secondary organs, based on the specific subtype: luminal BCs predominantly colonize bones, HER2 BCs metastasize in bones and liver, TNBCs disseminate to bones and lungs, whereas brain represents the least colonized organ across all BC subtypes, mostly because of the difficult extravasation through the blood brain barrier. Patients with brain metastases, followed by liver, display the worst prognosis [Soni *et al.*, 2015]. Regarding primary tumor features, higher risk of metastatic relapse is associated with large tumor size, increased vessel infiltration, hormone receptor negativity and p53 overexpression [Fitzpatrick *et al.*, 2014].

Adaptive stress responses in BC

The high genetic similarity between primary and metastatic BC suggests that the ability to metastasize may be part of the adaptive response of cancer cells to challenging microenvironmental conditions, such as hypoxia, endoplasmic reticulum (ER) stress, lack of nutrients and chemotherapy. As a matter of fact, many studies reported the major role of stress-response pathways in BC metastatic progression.

Hypoxia is a common feature of many solid tumors, including BC. While growing, the cells composing the tumor mass progressively increase their distance from blood capillaries, thereby finding themselves in a hypoxic state. Hypoxia, in turn, limits cell proliferation and promotes angiogenesis, via HIF-1 α stabilization: HIF-1 α regulates the transcription of VEGF, that fosters the sprouting of new leaky and permeable vessels at the tumor site, enabling intravasation [Semenza, 2003]. Hypoxia also stimulates BC cells EMT through the upregulation of the transcription factors SNAIL, ZEB1 and TWIST [Gao *et al.*, 2016]. In addition, hypoxic BC cells promote the expression of the gene ANGPTL4, that controls extravasation from the lung capillaries via the disruption of cell-to-cell junctions [Zhang *et al.*, 2012; Padua *et al.*, 2008].

Nutrient deprivation, as well, generates metabolic stress to BC cells. For instance, glutamine deficiency induces the expression of inflammation and stress-response mediators (*e.g.* ATF4), increasing cell migration [Gameiro and Struhl, 2018]. Similarly, glucose deficiency activates EMT through the induction of oxidative stress and overexpression of

metastasis-associated genes like VEGF [Marjon, Bobrovnikova-Marjon and Abcouwer, 2004]. Moreover, the accumulation of waste products, as lactate, determines the acidification of the TME, that ultimately leads to the upregulation of EMT and stemness-related genes [Sadeghi *et al.*, 2020].

ER stress is caused by several factors, such as hypoxia, lack of nutrients, chemotherapy and oxidative stress, which lead to the accumulation of unfolded proteins in the cells, disrupting cellular homeostasis. In this scenario, cells activate the unfolded protein response (UPR) pathway in order to block aberrant protein synthesis or to induce cell death. UPR activation has a role in BC metastatic progression: the overexpression of UPR mediators is associated to poor patient prognosis and metastatic relapse [Lacunza *et al.*, 2014], whereas their downregulation in hypoxic BC cells inhibits cellular migration and invasion, thus linking the metastatic phenotypes derived from UPR to hypoxia [Nagelkerke *et al.*, 2013].

Ultimately, it has been demonstrated that some chemotherapeutic agents (*e.g.* paclitaxel, carboplatin, doxorubicin, cyclophosphamide) may elicit several adaptive responses in BC cells such as: *i*) the release of inflammatory cytokines that promotes lymphatic vessel sprouting at the tumor site and subsequent lymphatic spreading of cancer cells [Volk-Draper *et al.*, 2014]; *ii*) the acquisition of stem-like invasive phenotypes [Liu *et al.*, 2018] and *iii*) the secretion of extracellular vesicles enriched for paracrine factors that prime pulmonary colonization, via monocytes recruitment or induction of endothelial leakiness [Keklikoglou *et al.*, 2019].

2.2.4 Models of metastasis

Modeling the biological complexity that characterizes metastasis necessarily demands the usage of equally complex experimental systems. A diversity of disciplines, including mathematic modeling, bioinformatics, physics, microscopy and mechanobiology are required to reach a detailed understanding of all the steps of the metastatic process [Malandrino, Kamm and Moeendarbary, 2018]. *In vitro* assays, such as wound healing, trans-well and microfluidic assays, are excellent tools for the cellular characterization of migration, invasion and adhesion events. However, these models lack a faithful recapitulation of TME and the three-dimensional architecture provided by ECM, that deeply influence cancer cell functional properties [Pouliot, Pearson and Burrows, 2013]. Each metastasis model has unique advantages and disadvantages: a single system will unlikely be sufficient to answer all questions. Therefore, the most appropriate model(s) should be chosen based on specific biological or translational issue(s). Among the plethora of different

available experimental systems, animal models – more commonly rodents – are undoubtedly the most appropriate to investigate human metastasis in all its complexity.

Transplantable mouse models of metastasis

Cancer cell lines and tissues transplanted in recipient mice can effectively survive, grow tumors and metastasize. Transplantable models can be divided into two groups: syngeneic or xenograft models. Syngeneic models result from the transplantation of murine cancer cells in animals of the same species and of the same genetic background of the transplanted cell line or tissue. The most important advantage of these models is the conservation of the TME, since the histocompatibility between the recipient host and the transplanted cells eliminates the need for immunosuppression. Therefore, syngeneic models are particularly useful when studying the contribution of the host immune microenvironment in metastatic progression. However, rodent tumors may not fully recapitulate the genetic complexity of human tumors [Khanna and Hunter, 2005].

Xenograft models are derived from the transplantation of human cancer cell lines or tissues into immunocompromised animals to prevent rejection: the resulting tumors are a mosaic of human cancer cells and murine stromal cells. Although xenografts allow to recapitulate several human cell features, they prevent to investigate the role of the immune system in cancer progression, being this aspect their most relevant limitation [Khanna and Hunter, 2005].

Both syngeneic and xenograft models can be generated applying two opposite experimental approaches, that differ in the way the cells are delivered to the recipient. The experimental metastasis approach is referred to as the direct transplantation of cancer cells in the systemic circulation. Following this method, metastases may develop in diverse anatomical regions of the mouse, depending on the specific cell tropism and the injection site. The most common site is the lateral tail vein, which results in lung metastases. Injection in the portal vein or in the spleen leads to the development of liver metastases, whereas intracardiac injection determines the emergence of metastases in the bones and in several other locations. The most evident advantage of this approach is the experimental rapidity and the experimenter's control on the number of cells actually introduced into the blood stream. However, the experimental metastasis strategy totally by-passes the early steps of the metastatic cascade – such as escape from the primary mass and intravasation – and negatively selects specific features of metastasis biology (*e.g.* dormancy). For these reasons, experimental metastases are often described as multiple primary tumors developed in a secondary site [Khanna and Hunter, 2005].

On the other way, the spontaneous metastasis approach is based on the transplantation of cancer cells or tumor fragments subcutaneously (heterotopic site) or orthotopically (*i.e.* injection in the same location from which the tumor was derived). In this setting the emergence of distant metastases is less frequent respect to the experimental metastasis approach but, especially orthotopic transplantation, more closely resembles human cancer features, including metastatic potential, tumor niche, histology, angiogenesis, response to therapy and expression patterns [Bibby, 2004]. Additionally, the spontaneous metastasis approach enables to follow also the early steps of the metastatic cascade. In case of rapidly growing cells, orthotopic transplanted primary tumors are often surgically removed to limit the mortality associated with excessive tumor burden and to extend the time window necessary to observe a metastatic outcome [Khanna and Hunter, 2005].

Genetically engineered mouse models of metastasis

Complementary to transplantable models, genetic engineered mouse models (GEMMs) provide the possibility to study *de novo* tumor and metastasis progression in an immunocompetent organism. Being their generation independent to cultured cells and transplantation systems, GEMMs permit to assess the influence of TME and genetic heterogeneity on tumor behavior. Moreover, all the steps of metastatic cascade are recapitulated and can be experimentally addressed. A great number of GEMMs of several distinct tumors – differing in their penetrance, metastasis incidence and latency – has been developed. As an example, a well-known engineered model of metastatic BC is the MMTV-PyMT mouse, obtained through the mammary gland-specific transgenic expression of the polyomavirus middle T antigen. These transgenic animals give origin to multifocal mammary carcinomas with 100% penetrance and develop pulmonary metastases in 85% of the cases, with a latency of 3 months [Guy, Cardiff and Muller, 1992]. The greatest disadvantage of GEMMs is represented by the elevated costs: due to the variability of tumor and metastasis penetrance and the latency of several months, large numbers of animals are required to be held for long periods of time in order to generate statistically significant data [Khanna and Hunter, 2005].

Imaging metastasis in mouse models

Imaging techniques have a crucial importance in the evaluation of cancer cell fate during metastatic process, as well as representing the cornerstone of diagnosis in clinical oncology. Various approaches to observe metastatic cell clusters and overt metastases in the living animal have been optimized, including bioluminescence, magnetic resonance imaging, positron enhanced tomography scan and intravital microscopy [Khanna and

Hunter, 2005]. Bioluminescence is one of the most used *in vivo* assay for metastasis imaging in the laboratory practice. The assay relies on the detection, with specialized cameras, of photons emitted by cells upon enzymatic reaction catalyzed by luciferase protein, revealing the site of luciferase activity within the body of the animal. Cancer cells, in this case, have to be genetically modified to express luciferase before transplantation. In the case of GEMMs, instead, specific constructs are included in their design. Although not particularly invasive, the bioluminescence assay is laborious, since it requires the administration of luciferin, the luciferase substrate, and the anesthetization and immobilization of the animal. In addition, the approach is limited by the intrinsic properties of light passing through tissues, thus restricting resolution and penetration depth and allowing to obtain only generic anatomical information [Kim *et al.*, 2010].

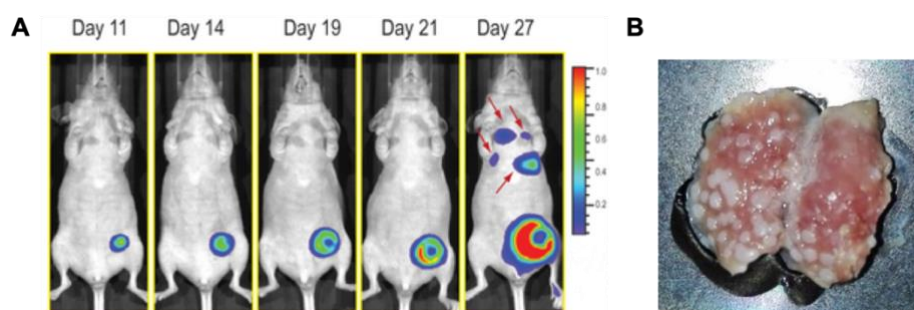


Figure 5 | Detection of metastases in the mouse model. Bioluminescence represents a non-invasive method to follow metastatic evolution longitudinally in the same cohort of mice but it offers a limited resolution (A) (modified from Kim *et al.*, 2010). Metastasis studies in mice often require the sacrifice of the animal and post-mortem organ analysis. The figure shows an explanted mouse lungs. The white nodules are BC metastatic lesions (B) (courtesy of Niccolò Roda).

Intravital microscopy, instead, provides high-resolution and single-cell level visualization of dynamic metastatic events, over extended imaging periods in the living mouse. Intravital imaging is based on the usage of stable optical windows, surgically exposed in specific anatomic regions of the animal (*e.g.* mammary, cranial or abdominal windows), combined with multiphoton microscopy. This method provides both spatial and temporal information about cancer cells behavior and, in association with cell tracing techniques, enables to follow individual cells over time, from metastatic colonization to metastasis outgrowth. However, intravital imaging remains experimentally challenging, requiring expensive equipment and well-trained operators. Thus, the application of intravital imaging is limited only to few specialized laboratories [Ritsma *et al.*, 2012].

Considering this scenario, the development of novel, less laborious, cost-effective and possibly quantitative *in vivo* models of metastasis represents an urgent need. Small vertebrates like zebrafish, for instance, may represent a valuable alternative or complementary model to mouse.

2.3 Zebrafish as a model of cancer and metastasis

2.3.1 Zebrafish: an overview

Zebrafish (*Danio rerio*) is a teleost freshwater fish native of Ganges river and its tributaries in southern Asia. Since 1980s, when Streisinger and colleagues introduced this species as an experimental organism [Streisinger *et al.*, 1981], zebrafish emerged as the model of choice for developmental biology due to its peculiar characteristics. Namely: *i*) developmental processes and genetic programs are conserved with the other species of vertebrates; *ii*) zebrafish is highly fertile, producing abundant offspring (approximately 200 embryos per mating couple every week); *iii*) embryos and *larvae* are transparent and develop externally, allowing for live high-resolution imaging and fast screenings; *iv*) zebrafish development is extremely rapid, with organogenesis completed in 3 days and hatching and autonomous feeding reached within 5 days [Kimmel *et al.*, 1995]; *v*) easy manipulation and cost-effective maintenance. The whole zebrafish genome, which consists of 1.4 Gbp and ~26,000 protein-coding genes, has been sequenced, revealing that 70% of human genes have an obvious ortholog in zebrafish. Moreover, >80% of all human disease-causing genes are conserved in zebrafish, suggesting the use of this fish also for effective modeling of human diseases [Howe *et al.*, 2013; Phillips and Westerfield, 2014]. Life cycle of zebrafish and larval anatomy are illustrated in Figure 6.

Being easily manipulated and offering the possibility to accelerate genetic studies (compared to mammalian models), zebrafish has largely diffused as a model for the investigation of vertebrate gene functions and a wide range of gene editing approaches have been optimized. Modulation of gene expression during development can be successfully obtained via micro-injection into the one-cell stage embryo of *in vitro*-synthesized mRNA molecules (“gain-of-function” approach) or antisense morpholino oligonucleotides (“loss-of-function” approach), enabling the transient overexpression or downregulation of a specific gene [Rosen *et al.*, 2009]. Several systems, including inducible and tissue-specific, are available for the generation of reporter and transgenic strains, in order to study gene expression patterns and ectopic expression of wild-type or mutated genes. Moreover, the CRISPR/Cas9 technique rapidly evolved in the last years and zebrafish knock-out lines obtained through CRISPR-based approaches widely spread since its first application in 2013, being zebrafish the first vertebrate engineered with this technology [Hwang *et al.*, 2013].

Zebrafish is extensively used for drug testing and chemical screenings, thanks to the permeability of embryos and *larvae* to small compounds delivered in fish water. Taking advantage of zebrafish high fecundity, therapeutic, toxic or teratogenic potentials of many

molecules – in different combinations and concentrations – can be tested simultaneously in a large cohort of animals at relatively low cost [Patton *et al.*, 2021].

Considering all the specific advantages offered by this species and the relative ease of genetic manipulation, in the last decades zebrafish has become a popular translational model, giving its contribution to several studies, ranging from genetic diseases to cancer.

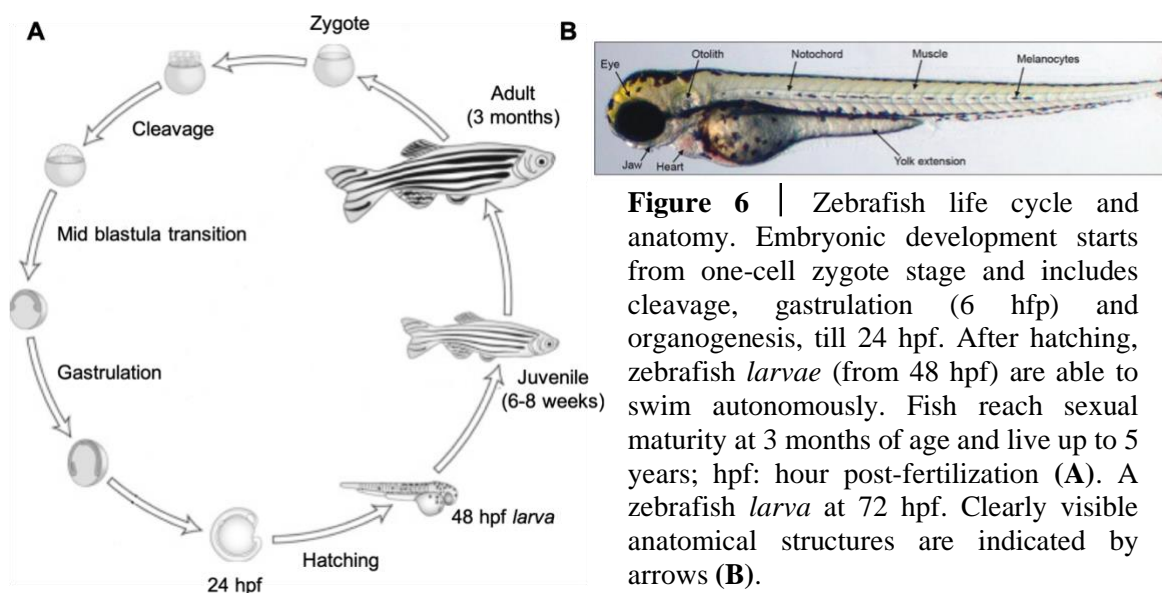


Figure 6 | Zebrafish life cycle and anatomy. Embryonic development starts from one-cell zygote stage and includes cleavage, gastrulation (6 hpf) and organogenesis, till 24 hpf. After hatching, zebrafish *larvae* (from 48 hpf) are able to swim autonomously. Fish reach sexual maturity at 3 months of age and live up to 5 years; hpf: hour post-fertilization (**A**). A zebrafish *larva* at 72 hpf. Clearly visible anatomical structures are indicated by arrows (**B**).

2.3.2 Cancer modeling approaches in zebrafish

Zebrafish has proven to be a powerful organism to study human cancer and a valuable complementary model to other, more traditional, systems. Crucial cancer-related pathways are highly evolutionarily conserved between zebrafish and human, allowing to recapitulate several aspects of the disease at molecular level. In addition, exploiting the use of reporter lines with fluorescently labeled tissues or optical transparent mutant strains (*i.e. casper*), it is possible to evaluate the interplay with TME and to follow cancer formation and dissemination in real-time. As a matter of fact, differently aged animals (from *larvae* to juveniles to adults) offer specific experimental advantages to study distinct cancer phenotypes.

Zebrafish, as well as other teleost fish, spontaneously develop with low incidence any type of cancer, being testis, gut, thyroid, liver, peripheral nerves, connective tissues and branchial glands the most common targets [Feitsma and Cuppen, 2008]. Historically, zebrafish started to be used as a cancer model in order to observe the effect of carcinogens. The exposure to water-soluble chemicals directly dissolved in fish water results in the formation of neoplasia (mainly hepatic carcinomas), which display histological and

molecular resemblance with human tumors, including similarities in genetic signatures involved in apoptosis, DNA repair and cell cycle regulation [Lam *et al.*, 2006]. These pioneering studies – while showing obvious disadvantages, such as low tumor incidence, late onset and heterogeneous genetic background and tumor location – first demonstrated that mechanisms of carcinogenesis are conserved between zebrafish and mammals [Stoletov and Klemke, 2008].

Stable transgenic cancer models

The advent of genetic engineering in the early 2000s dramatically changed the scenario of zebrafish cancer research and paved the way to a more faithful recapitulation of human tumorigenesis. As already mentioned, zebrafish transgenesis requires the introduction of foreign DNA into the genome of the zebrafish zygote and its expression in the cell population of interest. By the usage of tissue-specific promoters, initiation and progression of specific types of cancer can be induced and monitored. In 2003 Langenau and colleagues reported the generation of the first transgenic zebrafish model of T-cell acute lymphoblastic leukemia (T-ALL) by overexpressing the murine form of the oncogene *Myc* under the zebrafish lymphoid specific promoter *rag2*, which brings to the onset of T-ALL as early as 1 month of age [Langenau *et al.*, 2003]. After this foundational study, several other reports of leukemias and solid tumors lines – harboring oncogenic transgenes or oncogenic fusion proteins, including inducible models – rapidly followed. For instance, KRAS-driven models of rhabdomyosarcoma [Langenau *et al.*, 2007] and hepatocellular carcinoma [Nguyen *et al.*, 2016] have been generated, as well as models of pancreatic tumors [Yang *et al.*, 2004], melanoma [Patton *et al.*, 2005] and many others (for a comprehensive overview see Table 1).

Melanoma, in particular, represents a cancer type extensively investigated in zebrafish. A well-known zebrafish model of melanoma has been obtained introducing the mutated *BRAF^{V600E}* transgene (one of the most common genetic alteration in human melanoma) under the control of the melanocyte-specific zebrafish promoter *mitfa*. *BRAF^{V600E}* overexpression, in zebrafish as in humans, is not sufficient to initiate melanoma, but gives origin only to pigmented nevi. However, *mitfa:BRAF^{V600E}* fish carrying an inactivating mutation of *tp53* tumor suppressor gene, develop malignant melanomas with high penetrance [Patton *et al.*, 2005]. This study was the first one to describe that the combination of oncogene activation and loss of tumor suppression, determines cancer in zebrafish, recapitulating what already known from patients. Human melanoma is one of the most genetically abnormal of cancers and *mitfa:BRAF^{V600E};tp53^{M214K}* zebrafish line has a latency of 4-6 months until the disease manifests, suggesting that additional mutations are

required. Therefore, this model has also been used as a basis for a number of *in vivo* genetic screens, aiming to identify novel modulators of melanoma [Ceol *et al.*, 2011].

Table 1 | Transgenic zebrafish models of cancer (modified from Hason and Bartůněk, 2019).

| Cancer type | Genotype |
|---|---|
| T-cell Acute Lymphoblastic Leukemia (T-ALL) | <i>rag2:mMyc</i> <i>rag2:loxP-dsRED2-loxP-eGFP-mMyc</i> <i>rag2:NOTCH1</i> <i>pil:tel-jak2a</i> |
| Acute Myeloid Leukemia (AML) | <i>pul-MYST3/NCOA2-eGFP</i> <i>hsp70:AML1-ETO</i> <i>pHsFLT3-ITD-T2a-eGFP</i> <i>FLT3-ITD-T2a-mRFP</i> |
| Melanoma | <i>mitfa:BRAF^{V600E}</i> <i>mitfa:BRAF^{V600E};tp53^{M214K}</i> <i>mitfa:eGFP-NRAS^{Q16K}</i> <i>hsp70:eGFP-HRAS^{G12V}</i> <i>kita:Gal4xUAS-HRAS^{G12V}</i> |
| Rhabdomyosarcoma | <i>rag2:KRAS^{G12D}</i> |
| Hepatocellular carcinoma | <i>fabp10:LexPR;LexA:eGFPxcryB:mCherry;</i> <i>LexA:eGFP-KRAS^{G12V}</i> <i>fabp10:TA;TRE:Myc;krt4:GFP</i> <i>fabp10:TA;TRE:xmrk;krt4:GFP</i> |
| Pancreatic cancer | <i>ptf1a:eGFP-KRAS^{G12V}</i> <i>ptf10a:Gal4-VP16xUAS-eGFP-KRAS^{G12V}</i> <i>zmyod:MYCN</i> |
| Intestinal cancer | <i>pDs-ifabp:LexPR-Lexop:eGFP-KRAS^{V12}</i> <i>5xUAS:eGFP-P2A-KRAS^{G12D}</i> <i>fabp10a:mCherry-P2A-cyp7a1</i> |
| Testicular cancer | <i>fugu flck-SV40 large T</i> <i>brca2Q658X</i> |
| Thyroid cancer | <i>Tg:BRAF^{V600E}-pA;Tg:TdTomato-pA</i> |
| Ewing's sarcoma | <i>hsp70:EWSR1-FLi1;tp53^{M214K}</i> |
| Neuroblastoma | <i>dβh:eGFP-MYCN</i> <i>dβh:ALKF1174L</i> |
| Myeloproliferative neoplasm | <i>sp1:NUP98-HOXA9</i> |
| Corticotroph adenoma and neoplasm | <i>POMC-PTTG</i> |

Mutant models for cancer research

Loss-of-function studies of tumor suppressor genes in zebrafish is complicated by the fact that many genes have redundant copies, due to a genome duplication event occurred during evolution. However, zebrafish lines carrying targeted mutations of cancer-relevant genes have been generated. *tp53*^{-/-} line is one of the first zebrafish models to be established, because of the pivotal role of *tp53* as a tumor suppressor in human cancer. This line is characterized by the presence of an inactivating mutation of *tp53* (*tp53*^{M214K}), obtained through the usage of the mutagenic agent N-ethyl-N-nitrosourea. These mutant animals are susceptible to a malignant and highly aneuploid subtype of sarcoma, defined as peripheral nerve sheath tumor [Berghmans *et al.*, 2005]. Even though the zebrafish phenotype only partially recapitulates what observed in patients, *tp53*^{-/-} strain serves as a genetic background

to functionally test cooperation with candidate oncogenes, as already described. A more recent *tp53^{del/del}* zebrafish model which carries a loss-of-function deletion allele is able to actually phenocopy human p53 loss-of-function, as it develops a wide spectrum of tumors, including leukemia [Ignatius *et al.*, 2018].

The second most frequently mutated tumor suppressor in human cancer is PTEN, that in zebrafish is present in two distinct forms (*ptena* and *ptenb*), following gene duplication. Fish lacking *ptena* do not present abnormal phenotypes, whereas double mutants are not vital. On the contrary, *ptenb* mutants do not show an embryonic phenotype but develop ocular tumors around 18 months of age, demonstrating that the two forms of the gene have redundant functions in development and distinct roles in tumorigenesis in adult life [Faucherre *et al.*, 2008].

Mutations in the APC (Adenomatous Polyposis Cancer) gene are responsible for the vast majority of colorectal cancer, due to the constitutive activation of the Wnt pathway. While homozygous nonsense mutations in zebrafish *apc* are lethal, heterozygous fish develop intestinal and liver tumors in adult age that display activated Wnt signaling, suggesting that the molecular mechanisms underlying tumorigenesis for colorectal cancer are conserved [Haramis *et al.*, 2006].

The introduction of CRISPR/Cas9 system creates new opportunities for cancer modeling in zebrafish, enabling the rapid generation of stable knock-out lines or more complex genotypes. In a recent study, authors exploited a CRISPR-based platform called MAZERATI (Modeling Approach in Zebrafish for Rapid Tumor Initiation), to determine novel genetic drivers of mucosal melanoma, highlighting the cooperation between SPRED1 and *tp53* loss-of-function with *KIT* oncogenic mutations [Ablain *et al.*, 2018].

Transgene electroporation in adult zebrafish

Since all described methods require the injection of nucleic acids in the one-cell stage embryo, some difficulties in modeling cancer pathogenesis and progression may arise. In genetically engineered models, cancer onset and localization are not always biologically accurate and the evaluation of metastasis could be problematic. Some of these limitations can be addressed with the technique of cancer cell transplantation in both *larvae* and adult fish, that will be extensively discussed in paragraph 2.3.3. Moreover, the introduction of genetic alterations at an early embryonic stage may bring to severe developmental defects. To circumvent this issue, a new method of Transgene Electroporation in Adult Zebrafish (TEAZ) has been optimized. With TEAZ it is possible to inject and integrate DNA constructs directly into adult tissues such as muscles, heart or brain. This methodology was used to

generate adult fish developing aggressive melanoma with extremely early onset (7 weeks) respect to conventional models (4 months) [Callahan *et al.*, 2018].

To summarize, many distinct approaches, such as chemical carcinogenesis, transgenic lines, mutant lines and xenograft models, are currently being used to model human cancer in zebrafish. All these approaches, each with their own advantages and disadvantages, are reported in Table 2.

2.3.3 The zebrafish xenograft model

Besides genetic strategies, another fundamental cancer modeling approach in zebrafish is cancer cell xenotransplantation (XT), as briefly mentioned in the previous paragraph. XT is defined as the transfer of isolated species-specific cells, tissues or organs, to a recipient living organism belonging to a different species. XT technique has been used for many years in developmental, stem cell and cancer biology studies, dating back to the early 1940s [Greene 1938, 1941]. Adult somatic and cancer stem cells are functionally identified via transplantation strategies, based on their ability to self-renew and differentiate even after serial passages in subsequent generations of recipients. In cancer research field, XT is an indispensable tool to tackle several questions: *i*) evaluation of cell tumorigenicity, directly correlated with engraftment capability; *ii*) identification of cells with self-renewal potential within a tumor, through limiting dilution experiments; *iii*) studies of human cancer cell behavior in an *in vivo* context, taking into account the interactions with TME and all the events that cannot be reproduced *in vitro*, as metastasis and *iv*) generation of animal models for virtually any type of cancer, when genetic approaches are not applicable or available, including personalized patient-derived models [Gansner *et al.*, 2017]. Although mouse is considered the gold standard model for XT experiments, zebrafish possesses many favorable traits that make it an extraordinary transplant recipient.

Table 2 | Cancer modeling approaches in zebrafish.

| Technique | Applications | Advantages | Disadvantages |
|--------------------------------------|--|--|--|
| Chemical carcinogenesis | Evaluation of the carcinogenic effects derived from the exposure to chemicals | Easy Large scale Microscopy-based screening owing to transparency | Unspecific Predominance of liver tumors Low incidence Delayed onset |
| Transgenic lines | Study of tumor initiation/progression Large scale transgenesis for functional genetic screenings | Easy manipulation High genetic conservation Use of human genes Inducible and tissue-specific expression | Relatively slow to obtain (months) Different tumor spectrum and localization with respect to humans |
| Mutant lines | Study of the impact of loss-of-function mutations in tumor suppressor genes Large scale mutagenesis for functional genetic screenings | Easy manipulation (CRISPR/Cas9 available) High genetic conservation | Relatively slow to obtain (months) Genetic redundancy Different tumor spectrum and localization than in humans |
| Xenotransplantation in <i>larvae</i> | Development of <i>in vivo</i> models of several types of human cancer Study of cancer cells-microenvironment interactions Metastasis study Drug testing | Rapidity Large scale Few cells required Immune-permissive Use of fluorescent lines Microscopy-based screening owing to transparency | Technically challenging Limited orthotopic transplantation Homeostatic temperatures for cells and <i>larvae</i> are not compatible |
| Xenotransplantation in adults | Development of <i>in vivo</i> models of human cancer in a fully developed organism Study of cancer cells-microenvironment interactions | Use of transparent lines Organs are developed | Technically laborious Immunosuppression needed |
| TEAZ | Development of adult zebrafish cancer models with controlled tumor onset and localization | Rapid onset No effects on development Space-time regulation of tumor initiation | Technically laborious |

Xenotransplantation in zebrafish larvae: advantages and disadvantages

The use of zebrafish as a tool for human cancer XT allows to overcome some of the limitations of the murine model. The benefits provided by zebrafish are more relevant when using recipients at larval stages, thanks to specific characteristics:

- i. Zebrafish *larvae* transparency, combined with cell fluorescent labeling (obtained either via stable expression of fluorescent reporters, as GFP or RFP, or staining with lipophilic dyes, as DiL, DiD, DiO), which allows direct observation of cancer progression *in vivo*, without causing stress or damages to animals;
- ii. The lack of a fully competent adaptive immune system until 4 weeks post-fertilization [Lam *et al.*, 2004] eliminates the need for immunosuppression through chemicals or irradiation, or the necessity to use immunocompromised lines;
- iii. The short time needed to observe engraftment, cancer cell dissemination and micro-metastasis formation (as early as 1 day post-injection – dpi), which makes zebrafish XT assay a promising predictive tool for clinical practice;
- iv. The small amount of cells needed to achieve successful engraftment (from 100 to 2000 cells), which represents an advantage in case of limited amount of primary material (*e.g.* cells from biopsies);
- v. The abundance of offspring and the relative rapidity of the procedure, which allows to perform XT in hundreds of animals in a single round, facilitating high-throughput experiments and the achievement of statistical robustness;
- vi. The high feasibility of live imaging and the presence of well-established transgenic reporter lines with fluorescently labeled components of the host micro-environment (*e.g.* vascular systems, macrophages, neutrophils), which allow to visualize complex cancer cell phenotypes, such as intra- and extravasation or innate immunity response;
- vii. The larval permeability to molecules dissolved in fish water, which makes zebrafish xenografts a perfect model to perform large scale drug testing experiments;
- viii. The low cost of fish husbandry and maintenance;
- ix. The compliance with ethical standards for animal experimentation, exemplified by the “3Rs” (replacement, reduction, refinement), which asks for the use of the animal model with the lower neurological development, whenever possible.

Cancer cell XT is performed via mechanical micro-injection, a procedure analogous to the one used for the delivery of nucleic acids for genetic editing. Human cancer cells can be implanted at early embryonic stages, as blastula (2-5 hours post-fertilization, hpf) or, most commonly in 2 days post-fertilization (dpf) *larvae*: at this stage organ remodeling, via developmental cell migration events, is finished, thus cancer cell migration is likely to be an independent process [Kimmel *et al.*, 1995].

For 2 dpf *larvae*, injection sites are variable and include: the yolk sac (YS), the perivitelline space (PVS), the duct of Cuvier (DoC), the pericardial cavity, the eye and brain ventricles. The choice of the injection site depends on cell type and the cancer cell phenotypes intended to investigate. YS is an acellular lipid compartment that provides nutrients to the fish during development and it is often preferred as injection site due to the relative technical ease of the procedure (Figure 7A). YS constitutes a delimited space, rich in nutrients, where tumor formation and proliferation can be monitored over time. However, being composed of bulk proteins and lipids with no direct vascularization, YS environment could impact negatively on cell survival and evaluation of cell motility is limited. PVS is a “pocket” located at the interface between the periderm and the yolk syncytial layer that can accommodate large amount of cells without communicate directly with vasculature (Figure 7B). Micro-injection in this region is challenging but allows to accurately detect – aside from engraftment and proliferation – all the steps of the metastatic cascade, including early steps like EMT and intravasation [Brown *et al.*, 2017]. Moreover, also tumor neo-angiogenesis can be unambiguously evaluated performing transplantation in this site [Nicoli and Presta, 2007]. DoC is an embryonic vascular structure that runs ventrally across the YS, carrying venous blood to the heart (Figure 7 C). It allows the direct injection of cells into the circulation, where cells are able to survive, migrate, extravasate and undergo MET to invade secondary sites, mostly the caudal region. Therefore, transplantation in the DoC enables to study hematogenous cancer cell dissemination and late steps of the metastatic process [Asokan *et al.*, 2020]. Finally, XT in the eye or brain ventricles is less frequently chosen, only when it is necessary to transplant cells orthotopically, as in case of retinoblastoma [Chen *et al.*, 2015] or glioblastoma [Cam *et al.*, 2020].

Since temperature is a critical environmental parameters for both efficient cancer cell engraftment and correct larval development, zebrafish xenografts are commonly maintained at 34°C – a compromise between zebrafish physiological temperature of 28°C and optimal cell culture temperature of 37°C – enabling human cancer cell proliferation without compromising fish survival. Incubation temperature is one of the most discussed point of zebrafish xenograft assay, representing a drawback of this model: many experts underline the fact that possible metabolic or transcriptional changes may occur to cancer cells and fish may be affected by hyperthermia (*e.g.* activation of immune system, inflammation, malformations, increased mortality) [Pype *et al.*, 2015]. Thus, a correct balance between temperature and incubation time must always be taken into account when performing a zebrafish XT experiment [Cabezas-Sáinz *et al.*, 2020]. Moreover, studies in which maintaining the homeostatic temperature of 37°C is important to oncogenic behaviors are still restricted only to mammals.

Another inherent limitation of zebrafish xenografts is the restricted possibility to perform orthotopic transplantation. The lack of mammalian organs, such as lungs, prostate or breast, limits orthotopic transplantation only to few cancer cell types (*e.g.* human brain tumors in zebrafish brain). As a consequence, the niche of specific human tumors, formed by both cellular and stromal components interacting with cancer cells, is not fully recapitulated in zebrafish and the human disease cannot be mimicked with perfect accuracy.

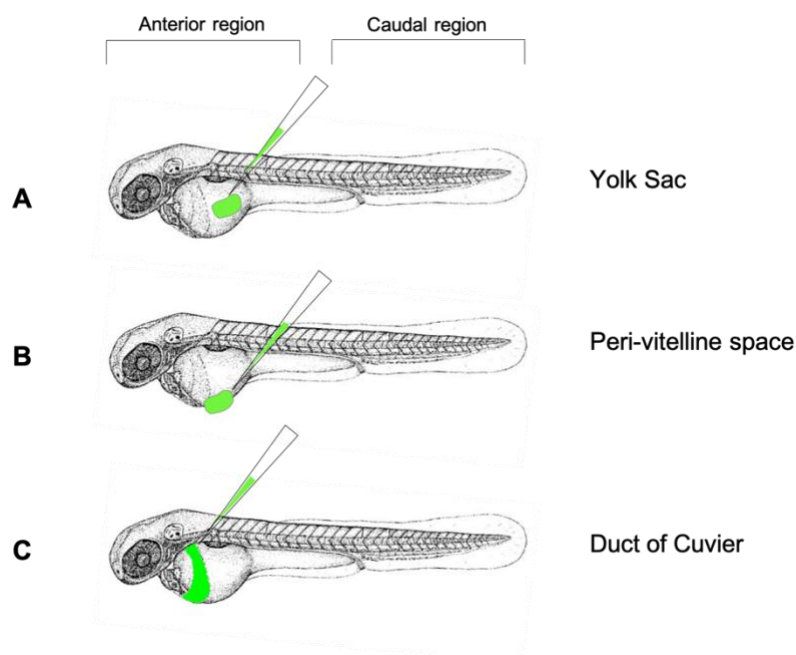


Figure 7 | Representation of the three most frequently exploited injection sites in the zebrafish 2 dpf larva. The yolk sac allows to accommodate cells in a large delimited acellular space but lacks the interactions with host microenvironment (**A**). Peri-vitelline space injection enables to place cells in a pocket between the periderm and the yolk, recapitulating a subcutaneous injection (**B**). Cells injected in the duct of Cuvier are immediately incorporated into the larval circulation. Cells are shown in green (**C**).

Pioneers in zebrafish xenotransplantation

The first studies that report XT of human cancer cells in zebrafish were published between 2005 and 2007. The fundamental work of Lee *et al.* describes the generation of xenografts by transplanting human melanoma cells into embryos at the stage of blastula: authors observed that melanoma cells survive, divide and respond to developmental cues – colonizing their original environment, the skin – but do not form tumors. These observations demonstrated for the first time that zebrafish embryos offer an environment compatible with human cancer cell survival and produce signals necessary to sustain cell migration and integration in zebrafish developmental programs [Lee *et al.*, 2005]. One year later, Haldi and colleagues – always using melanoma cells – optimized parameters for XT, such as injection sites, number of injected cells and incubation temperature and they proposed 2 dpf larvae as recipients, which soon became the standard protocol. Notably, this was the first study to

show that human cancer cells proliferate to form overt tumor masses in zebrafish [Haldi *et al.*, 2006]. Soon researchers focused on the observation of the interaction between transplanted cells and host microenvironment. Nicoli and coworkers first observed that human or murine cancer cells expressing fibroblast growth factor 2 (FGF2) and/or vascular endothelial growth factor (VEGF) induce the formation of new vessels at the tumor site and they were able to quantify this parameter, discriminating between highly and poorly angiogenic cancer cells [Nicoli *et al.*, 2007]. A forerunner study in the field of zebrafish patient-derived xenograft (zPDX) generation is the one published by Marques *et al.* in 2009. They transplanted cancer cell lines and tissue fragments from pancreas, stomach and colon primary carcinomas into the YS of 2 dpf *larvae*, demonstrating the feasibility of implanting primary human tumors in zebrafish. Interestingly, the authors monitored cancer behavior until 3 dpi, observing invasiveness and micro-metastasis formation within 24 hours from the injection [Marques *et al.*, 2009].

During the following years, many independent researchers have refined larval XT technique, extending the variety of cancer cell types transplanted and defining new strategies to obtain quantitative and physiologically-relevant results. Several tools for image-based quantification of specific cancer hallmarks such as proliferation, dissemination, metastasis and angiogenesis have been developed, including ImageJ/Fiji open source and commercial software. Most of the studies have been performed using cancer cell lines, establishing xenografts models of various tumors, such as: melanoma, glioma, glioblastoma, hepatocellular carcinoma, neuroendocrine tumors, Ewing sarcoma, retinoblastoma, leukemia, colorectal, lung, gastric, pancreatic, ovarian, breast and prostate cancers [Costa *et al.*, 2020a].

Tumor microenvironment studies using zebrafish xenografts

An important improvement to the model, aiming at better analyzing the influence of TME on tumor progression, was the use of reporter zebrafish lines. These strains enable non-invasive live imaging and visualization of cancer-host interactions in real-time at single cell level, a condition difficult to achieve in mouse models.

To evaluate the ability of transplanted cells to develop a new tumor vascular network and to follow their ability to disseminate through the blood stream, many transgenic lines with labeled vasculature are available, such as *Tg(fli1:eGFP)*, expressing eGFP under the endothelium-specific transcriptional factor *fli1* promoter [Lawson and Weinstein, 2002] and *Tg(kdrl:GFP)*, expressing GFP under the VEGF receptor promoter [Cross *et al.*, 2003].

Albeit not capable of adaptive immunity, zebrafish *larvae* have a fully competent innate immune system. Exploiting the use of reporter lines such as *Tg(mpx:GFP)*, that

expresses GFP under the neutrophil-specific myeloperoxidase promoter [Renshaw *et al.*, 2006] and *Tg(mpeg1:eGFP)*, expressing eGFP under the macrophage-specific perforin *mpeg1* promoter [Ellet *et al.*, 2011], it is possible to monitor the interactions between neutrophils, macrophages and human cancer cells. One seminal study published in 2012 reported the use of both neutrophil and vasculature transgenic fish transplanted with various cancer cell lines, showing that such immune cells infiltrate both the primary tumor and the micro-metastases. Authors also observed that cancer cells remodel the endothelial cells of the DoC to form *de novo* vessel-like structures, which subsequently develop into functional vasculature. Transient silencing (obtained by morpholino microinjection) of a transcription factor that controls differentiation of zebrafish myeloid cells blocks both tumor angiogenesis and metastasis, demonstrating the direct cooperation of neutrophils in cancer cell progression [He *et al.*, 2012]. Similarly, Britto *et al.* showed that also macrophages have a role in vascularization and that neo-angiogenesis is dependent on the amount of macrophages recruited at the tumor site (Figure 8) [Britto *et al.*, 2018]. Roh-Johnson and colleagues, instead, observed a role for macrophages in melanoma metastatic dissemination: macrophages dynamically interact with transplanted melanoma cells by direct transfer of cytoplasmic content and this interaction positively correlates with cancer cell spreading [Roh-Johnson *et al.*, 2017].

Not only angiogenesis and cell dissemination are influenced by the host immune microenvironment, but a very recent work demonstrated that different human colorectal cancer cell lines display heterogeneous engraftment potentials and growth profiles, depending on cancer cell capacity to interact with macrophages and neutrophils. The authors described and transcriptionally characterized “regressor” tumors as those showing the higher degree of immune cell recruitment, poor engraftment and immune clearance, while “progressor” tumors recruit fewer immune cells, engraft efficiently and grow. Moreover, progressors directly shape the immune TME, polarizing tumor-associated macrophages toward a M2 pro-tumoral phenotype that, in turn, allows the implantation of regressor cancer cells when they are co-transplanted with progressor cells [Póvoa *et al.*, 2021]. Notably, to observe the polarization state of macrophages, cancer cells were injected into another transgenic fish line named *Tg(mpeg1:mCherry-F; tnfa:eGFP-F)*, with double-labeled anti-tumor M1 macrophages, characterized by the fluorescently marked expression of tumor necrosis factor alpha [Nguyen-Chi *et al.*, 2015]. These results open the possibility to use zebrafish xenografts as a living platform to reveal the innate immune TME condition, discriminating between pro- and anti-tumoral macrophages phenotypes states in just 4 days.

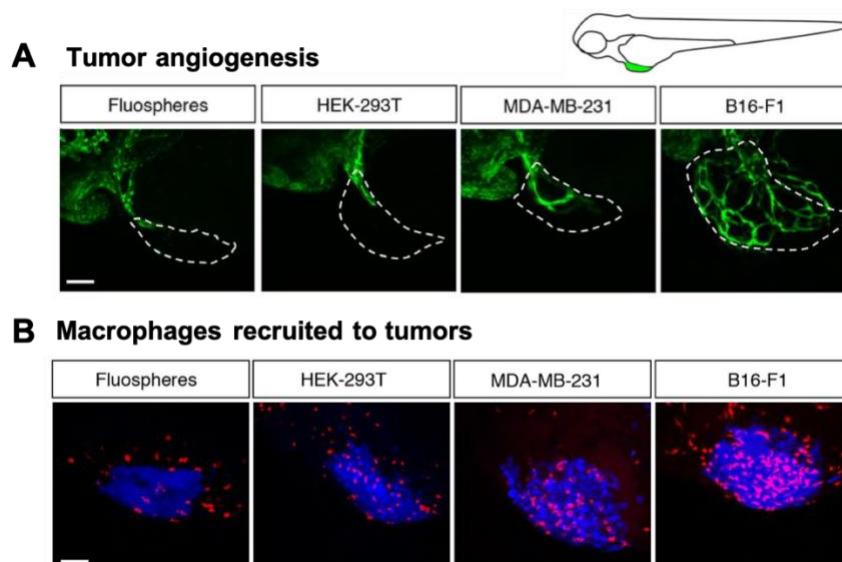


Figure 8 | Use of transgenic reporter zebrafish strains to study interactions with TME. Confocal images of *Tg(fli1:eGFP)* larvae with green blood vessels show neo-angiogenesis in grafted tumors (breast: MDA-MB-231; melanoma: B16-F1), opposite to xenografts transplanted with non-tumorigenic cells (HEK-293T) and fluorescent beads (no cells). In the upper left corner the scheme indicates the location of the graft in green (A). Confocal images of *Tg(mpeg:eGFP)* expressing macrophages in red, display macrophages recruitment to primary tumors. Grafts are shown in blue (B) (modified from Britto *et al.*, 2018).

Drug testing in zebrafish xenografts

The use of fish for toxicity studies and phenotypic drug screenings has a long tradition due to the ease of drug administration, the direct recognition of developmental defects as a readout and the possibility to increase the experimental scale at low cost compared to other *in vivo* models. Although pharmacokinetic processes in zebrafish are still poorly investigated, key enzymes responsible for drug metabolism and pharmacological effects are conserved between fish and mammals, proving a good translatability of the results. Zebrafish *larvae* are also well suited for medium-to-high throughput chemical screenings, since animals can be tested in 96-multi-well plates with automated imaging systems and analysis [Fazio *et al.*, 2020].

Zebrafish xenografts have been frequently used to evaluate effects of anticancer drugs, since they enable to assess drug response both in the living animal and within the human tumor: various types of chemotherapeutic agents, but also small molecule inhibitors (*e.g.* olaparib [Varanda *et al.*, 2020]) and monoclonal antibodies (*e.g.* such as cetuximab [Fior *et al.*, 2017]) have been successfully tested in this model. Drug response is measured by direct imaging of labeled cancer cells in the transparent recipient and subsequent quantification of tumor size, similarly to mouse xenografts. In addition, other more specific parameters such as primary tumor cellularity, expression of proliferative or apoptotic markers and the extent of cancer cell invasion can be measured in zebrafish xenografts,

thanks to the higher resolution achievable with this model. For instance, the chemical inhibition of NF- κ B-activin A pathway leads to a reduction of prostate CSCs pool and decreases metastases in both zebrafish and mice xenografts [Chen *et al.*, 2020]. Other studies on brain tumors, performed on zebrafish xenografts, identified novel druggable targets for glioblastoma therapy [Banasavadi-Siddegowda *et al.*, 2018] and demonstrated the efficacy of combining of traditional chemotherapy (temozolomide) with targeted-therapy (HSP90 inhibitor onalespib) against malignant gliomas [Canella *et al.*, 2017]. Targeted therapies directed against TME are also feasible in zebrafish xenograft and translatable to humans (if the molecular target is conserved across the two species), as demonstrated by the strong suppression of tumor angiogenesis following treatment with VEGF inhibitors, including the monoclonal antibody bevacizumab [Nicoli *et al.*, 2007; Rebelo de Almeida *et al.*, 2020].

Besides demonstrating its utility to test therapy efficiency, the zebrafish xenograft model is also extremely fast, offering the potential to greatly accelerate drug discovery in pre-clinical *in vivo* models. This characteristic, combined with the high statistical power and the low costs, suggests that the use of zebrafish larval xenografts could be compatible with clinical needs and timeframe. As a matter of fact, some research groups are working to optimize the zebrafish xenograft model as a rapid *in vivo* profiling platform to predict patients' sensitivity or resistance to anticancer therapies. One important study used cell line-derived zebrafish xenografts to test current medical guidelines for the treatment of metastatic colorectal cancer, starting from the first-line therapy with antineoplastics (FOLFOX and FOLFIRI) and moving to second- and third-line targeted agents (Cetuximab and Regorafenib), demonstrating that zebrafish xenografts allow to discriminate differential tumor behaviors and drug responses, recapitulating what observed in mice but in an experimental time-window of just 4 days. The authors also generated zPDXs (zebrafish Patient-Derived Xenografts) from 5 different resected human colorectal tumors of known clinical progression and chemosensitivity and treated them according to standard therapeutic protocols: in 4 out of 5 cases they were able to anticipate relapse/no relapse after surgery of the corresponding patient, based on the zPDX readout [Fior *et al.*, 2017]. Notably, this proof-of-concept study paved the way for the introduction of the zebrafish larval xenograft model in precision cancer therapy, as a tool to help oncologists to predict how a specific tumor/patient will respond to a certain treatment.

Zebrafish patient-derived xenografts for precision oncology

Clinical guidelines for the treatment of cancer are based on average rates of drug efficacy observed in oncological patients and still consist for most tumors in conventional surgery, chemo- or radiotherapy. However, given the huge genetic and phenotypic

heterogeneity of cancer, these treatments are not effective for all patients, who undergo a “trial-and-error” approach to set their definitive therapy, being exposed to unnecessary toxicity. The definition of the correct therapeutic protocol becomes even more relevant in case of metastatic tumors, when most of the traditional options are not effective. Precision medicine aims to address the problem of ineffective anticancer cures basing clinical decisions on patient’s unique tumor characteristics. Thus, new adequate tools to make powerful predictions are needed. In this scenario, genomic sequencing, functional *in vitro* assays and drug testing in mouse patient-derived xenografts (mPDXs) are the most diffused strategies, while zPDXs usage is currently expanding (Table 3).

Genomic sequencing technologies allow to associate a patient’s response to specific drugs to the tumor’s genetic and transcriptional profiles. This approach, named pharmacogenomics, is based on the identification of biomarkers for patients’ stratification in specific therapeutic regimens. For instance, BC patients with high levels of expression of estrogen receptor are eligible to be treated with endocrine therapies.

Patient-derived cancer cells can be used to establish 3D cultures as an *in vitro* personalized drug screening platform: organoids derived from freshly collected tumor pieces overall maintain the histological and genetic characteristics of the original tumor, including mutational burden. However this method has a limited predictive power, is time-consuming and lacks the stromal components necessary to mimic proper interactions with TME, that can be exclusively recapitulated in a living organism [Costa *et al.*, 2020a].

The *in vivo* approach is the only alternative that allows to model tumor complex phenotypes, including metastasis, and to evaluate pharmacodynamics and toxicity in the whole organism. PDXs, also known as patients’ “avatars”, are obtained via transplantation of human primary cancer cells into living hosts, most commonly immune-compromised mice. Animals are monitored until the graft – implanted subcutaneously or orthotopically when possible – forms a palpable mass, generally within 1 to 10 months from transplantation and then used for drug testing or explanted and transplanted in other animals for serial passages of *in vivo* amplification. mPDXs conserve both the histopathological features of the original tumor and its genetic heterogeneity [Hidalgo *et al.*, 2014] and they show a high predictive value, as demonstrated by many retrospective studies, involving high numbers of animals [Bertotti *et al.*, 2011; Gao *et al.*, 2015]. Co-clinical studies, instead, consist in the longitudinal treatment of both patients and their matching mPDXs with the same protocol and are designed to guide the choice of a personalized treatment. mPDXs commonly take months to be generated, therefore co-clinical studies are feasible only in case of tumors with a progression rapid enough to be compatible with clinical timeframe and large availability of fresh tumor material from surgery. This is the case reported by Vargas *et al.*, for a patient

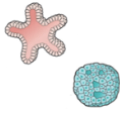


affected by clear cell adenocarcinoma, where corresponding mPDXs predicted response and development of resistance to first-line therapy (gemcitabine/nivolumab) accompanied by relevant changes in gene expression and subsequent response to second-line therapy (paclitaxel/neratinib), before these events took place in the patient [Vargas *et al.*, 2018]. Nevertheless, in most cases the long latency for tumor engraftment, the limited availability of cancer tissues and the high costs constrain the use of mPDXs for clinical decision making.

Concerning the generation of zebrafish patient-avatars, the number of promising studies in this field is growing rapidly, since *larvae* could overcome some intrinsic limitations of the murine model. Marques and colleagues were the first to transplant fragments of human gastric, pancreatic and colorectal cancer in the YS of zebrafish *larvae* [Marques *et al.*, 2009]. Afterwards zPDXs of other tumors were successfully generated and challenged in retrospective studies. Lin *et al.* generated zPDXs of multiple myeloma injecting primary cells from 6 different patients in the PVS, with an engraftment efficiency of 80%. Investigators also treated zPDXs with bortezomib and lenalidomide, observing a positive response in fish avatars obtained from sensitive patients and resistance in those transplanted with metastatic tumors, mirroring each patient's clinical outcome in 4 days [Lin *et al.*, 2016]. However, a broad consensus regarding technical standards for zPDXs generation and analysis is still lacking. Most of the literature data rely on the transplantation of cultured primary human cancer cells in variable anatomical sites, infer tumor growth on the basis of epifluorescence microscopy images and describe assays with different lengths. One co-clinical trial described the generation of zebrafish avatars from 24 patients affected by colon, pancreatic and gastric adenocarcinomas and the evaluation of chemosensitivity for each individual patient. Authors transplanted surgically resected tissue fragments according to the protocol from Marques *et al.* and assessed drug response, in terms of reduction of stained tumor area, in the next 2 days. Additionally, this study set up a mathematical criterion to convert the chemotherapy dosage used in humans to zebrafish *larvae*, solving a critical aspect of this kind of assay [Usai *et al.*, 2020].

Recently, Fior group systematically optimized protocols for the generation of zPDXs, transplanting single cell suspensions obtained from freshly collected colorectal cancer biopsies, setting up a robust battery of analytic parameters (*e.g.* quantification of tumor size via DAPI counting, mitotic index, cell death, angiogenic and metastatic potential) based on high-resolution confocal imaging. As already reported earlier in the paragraph, Fior *et al.* also performed a retrospective drug testing experiment, predicting the clinical outcome for 80% of the patients tested [Fior *et al.*, 2017]. The same research group expanded the procedure and analysis to BC zPDXs [Rebelo de Almeida *et al.*, 2020] and also for the

evaluation of radiotherapy sensitivity in a cohort of 19 colorectal cancer patients [Costa *et al.*, 2020b].

Table 3 | Comparison between patient-derived avatar models.

| Cancer avatar type | <i>In vitro</i> 3D cultures | Mouse PDXs | Zebrafish larvae PDXs |
|----------------------------|---|--|---|
| |  |  |  |
| Duration | 4-5 weeks | Months | 1 week |
| Cost | Low | High | Low |
| N° of cells required | 10 ³ | 10 ⁵ -10 ⁶ | 10 ² |
| N° of avatars | Hundreds | ~5/condition | ~30/condition |
| Single-cell resolution | Yes | No | Yes |
| Patient's TME conservation | No | Low or No | No |
| Dose optimization | Yes | Yes | Yes |
| Retrospective studies | Yes | Yes | Yes |

Xenotransplantation in zebrafish adults

Adult zebrafish develop penetrant and advanced tumors, both via transgenesis and via zebrafish or human cancer cells transplantation. Adult zebrafish offer improved potential for *in vivo* imaging compared to murine models, and for the analysis of CSCs, cancer progression and metastasis analyses. One of the major difficulties of cell transplantation in adults is the opacity of the animals, that limits microscopy resolution. To address this issue, the *casper* zebrafish strain has been generated by mating two pigment mutants called *nacre* and *roy*: these fish lack both melanocytes and iridophores, conserving optical transparency throughout adulthood and allowing for the detection of fluorescent cell engraftment with great sensitivity [White *et al.*, 2008].

As for mice, also adult zebrafish require immune system ablation for long-term implantation and survival of transplanted cells. The generation of adult xenografts involves immunosuppression using gamma radiations [Traver *et al.*, 2004] or chemical treatments [Stoletov *et al.*, 2007]. The first approach is transient, since the host immune system fully recovers and rejects the graft within 30 days from the irradiation. The second approach, while allowing long-term engraftment, requires constant administration of the steroid dexamethasone, adding experimental variability. Moreover, being dexamethasone itself used as an anticancer drug in leukemias and lymphomas, this strategy is not suitable to model this kind of tumors [Fazio *et al.*, 2020]. Recently, a considerable step forward was made by Langenau group, with the development of a stable immunodeficient zebrafish line that efficiently engrafts human patient-derived cancer cells. The authors generated optically clear

adult zebrafish with inactivating mutations in protein kinase DNA-activated catalytic polypeptide (*prkdc*) and in interleukin 2 receptor gamma (*il2rga*), which lack T, B and NK cells. Importantly, these fish can survive at 37°C. This model engrafts a large variety of patients' tumors (rhabdomyosarcoma, glioblastoma, melanoma and BC) for 28 days, displaying growth kinetics, chemo-sensitivity, proliferative and apoptotic indexes similar to those observed for the same tumors in NGS mice [Yan *et al.*, 2019].

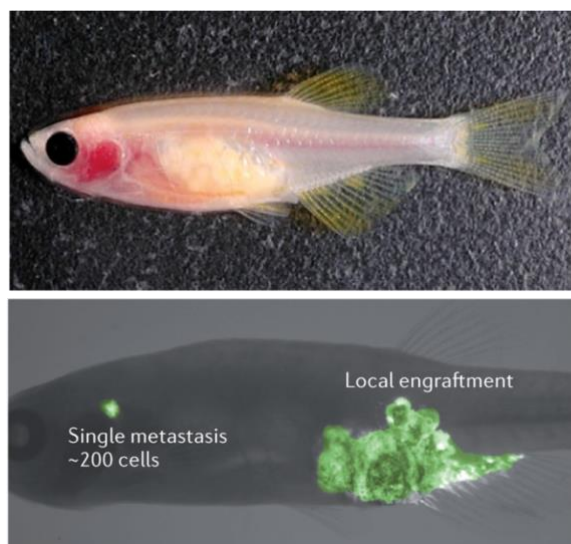


Figure 9 | Tumor engraftment and dissemination in an adult *casper* mutant recipient. Cancer cells express GFP (modified from White, Rose and Zon, 2013).

2.3.4 Cell invasion and metastasis in zebrafish xenografts

The practical and scientific advantages of the larval zebrafish xenograft model for basic cancer biology studies, precision oncology and drug discovery have been extensively described in the previous paragraphs. In addition, the peculiar features of zebrafish xenografts make them eligible also as metastasis model systems. The imaging tools used to investigate metastatic progression in the current existing *in vivo* models are not amenable for long-term monitoring of cancer cells in real-time since they rely, as in case of intravital imaging, on surgical intervention to expose the imaging sites, causing animal stress and survival issues [Ritsma *et al.*, 2012]. Bioluminescence assay, although being non-invasive and representing a valid tool to assess tumor burden, does not provide precise quantification of tumor volume or number of metastatic clusters [Kim *et al.*, 2010]. Moreover, metastasis investigation in mice often requires euthanasia and *post-mortem* organ examination. Zebrafish easy manipulation and transparency at larval stage, coupled with the availability of pigment-deficient mutants, reporter lines with fluorescent vasculature and stable labeling

of cancer cells, provide enough *in vivo* optical resolution for single metastatic cell space-time tracking in real-time and in a time-window of few days.

Dynamics of both solid and leukemic cancer cells dissemination in the zebrafish *larva*, including cell speed and trajectories, have been characterized in detail. The micro-injection in the acellular space termed PVS of 2 dpf *larvae* (see paragraph 2.3.3 - “*XT in zebrafish larvae: advantages and disadvantages*”) recapitulates the entire multistep metastatic cascade, from cell detachment from primary tumor to secondary organ colonization. On the contrary, straightforward intravenous injection mimics only the late metastatic steps (from CTCs survival to overt metastases). With both modalities of injection, CTCs – irrespective of tumor cell type – initially migrate towards the larval tail, moving along the dorsal aorta and the posterior cardinal vein, predominantly arresting in the caudal vein plexus (CVP) [Follain *et al.*, 2018a; Paul *et al.*, 2019; Asokan *et al.*, 2020]. CVP comprises an interconnecting network of sinusoid capillaries that host peri-vascular hematopoietic stem and progenitor cells, constituting the caudal hematopoietic tissue (CHT). CHT is a vascular niche that, similarly to mammalian fetal liver or bone marrow [Xue *et al.*, 2017], sustains hematopoietic stem cell differentiation in zebrafish *larvae* and represents a “hot spot” for metastatic cell homing. Interestingly, the presence of the hematopoietic niche is considered to be one of the factors involved in cancer cells tropism to the bone marrow [Shiozawa *et al.*, 2015]. Moreover, the chemokine CXCL12-CXCR4 signaling axis, which is responsible for hematopoietic stem cell pool maintenance, is conserved between zebrafish and mammals [Ma *et al.*, 2011] and its role in human TNBC metastases has been demonstrated in zebrafish xenografts [Tulotta *et al.*, 2016].

In the first 12 hours post-injection cells tend to passively accumulate in the CHT due to its chaotic topography: the tortuosity of the vessels and their small diameter decelerate blood flow, causing cell arrest [Paul *et al.*, 2019]. High-resolution imaging data also highlighted that CTCs from solid tumors display a change of shape – from round to amoeboid – which helps their migration from the CVP to the intersegmental vessels and the dorsal longitudinal anastomotic vessel, demonstrating the morphological adaptability of metastatic cancer cells to stay motile [Asokan *et al.*, 2020]. Cell arrest in the CVP is not only due to mechanical forces but, as already mentioned, is facilitated by the presence of the larval hematopoietic niche, that constitute a favorable microenvironment for cancer cells, characterized by the presence of myeloid cells. As a matter of fact, it has been reported that the physiological migration of neutrophils between the CHT and the tail fin results in transient collagen deposits that promote cancer cell invasion in this area [He *et al.*, 2012].

Later during metastatic progression (from 1 to 5 dpi) metastatic cells undergo extravasation. Contrary to the murine model, the possibility to image the whole zebrafish

larva with single-cell resolution, enables to visualize the process of exit from the circulatory system into secondary organs. Cancer cells mostly colonize the peri-vascular parenchyma in the CVP and the collagenous fibers of the tail fin, but metastatic clusters can also be found in the eye, brain, gills and muscles [Fior *et al.*, 2017].

Zebrafish xenografts enable to demonstrate that hemodynamic profiles at metastatic sites regulate extravasation: Follain and colleagues observed that the permissive blood flow forces in the CVP promote the stable adhesion of CTCs to the endothelium and endothelial cells themselves engage massive remodeling in order to encapsulate cancer cells and mediate their extravasation [Follain *et al.*, 2018a]. Besides blood flow-mediated adhesion of CTCs and endothelium remodeling, active interaction between cancer cells and adhesion endothelial molecules or extracellular matrix components are required for successful organ-specific extravasation. Considering metastatic BC cells, integrin $\beta 1$ is involved in the extravasation in the CVP, whereas myosin 1B also mediates extravasation in the brain, confirming the capability of discriminating differential organ-targeting cell clones [Paul *et al.*, 2019]. All these studies demonstrate that zebrafish larval xenografts allow to investigate in details the dynamics of metastatic cell dissemination and interaction with the host microenvironment.

In few cases, zebrafish xenografts have also been used as a platform for *in vivo* functional genetics experiments, in order to assess the role of candidate genes in metastatic progression, by silencing or activating their expression in cancer cells prior to transplantation [de Boeck *et al.*, 2016; Tulotta *et al.*, 2016]. Furthermore, zebrafish xenografts have also been exploited to understand the contribution of hypoxia to the early events of metastatic cascade, shedding light on the mechanisms of angiogenesis and adaptive stress response in metastasis [Lee *et al.*, 2009].

2.4 Aim

Metastatic disease is the major cause of cancer-related deaths: the 5-year survival for women with metastatic BC is approximately 30% [Torre *et al.*, 2017]. Being a process biologically distinct from primary tumor growth, metastatization requires studies designed *ad hoc* to unveil the still poorly understood molecular mechanisms underlying the different phases of the metastatic cascade. As a matter of fact, each metastatic step (extensively described in paragraph 2.2.1) may represent a potential vulnerability, offering targets to be explored in the clinical context.

Metastasis studies require the usage of experimental systems ideally capable to mimic and explore all the multiple phases of the metastatic cascade. Since *in vitro* approaches do not fully recapitulate the metastatic process and murine models present several limitations (see paragraph 2.2.4), zebrafish larval xenograft assay is proposed as a valuable system to investigate metastatic progression. Strikingly, in zebrafish *larvae* spatial and temporal features of the metastatic cascade can be tracked in real-time, at cellular resolution, without invasive procedures. Therefore, the first aim of this work is the development and characterization of a robust and extremely rapid zebrafish xenograft model of BC progression and metastasis. This technology has never been applied before in the laboratory where the project was carried out. In detail, the ultimate goal of the study is to exploit the peculiar features offered by zebrafish *larvae* to provide a quantitative dissection of BC multistep metastatic cascade.

Recently, our research group performed an *in vivo* clonal tracking study in order to investigate transcriptional phenotypes during metastatic progression of human BC. By this approach, a detailed description of the clonal architecture of BC primary tumors and metastases was achieved and identified a BC pro-metastatic transcriptional signature was identified. The second goal of the project is the *in vivo* validation of the potential metastasis genetic determinants obtained from the transcriptional signature, using the zebrafish larval xenograft model. In detail, the zebrafish assay optimized in this study enables to map the function(s) of single candidate genes, characterizing their stage-specific role in BC metastatic cascade and testing whether it could represent a targetable vulnerability of the metastatic process.

Furthermore, as a possible future application of the zebrafish larval xenografts model, I aim to set up a rapid and scalable assay to test the efficacy of chemical compounds on xenografted breast tumor in the zebrafish host.

3. Materials and Methods

3.1 Animal care and handling

Zebrafish (*Danio rerio*) from wild-type *AB* and *Tg(kdrl:DsRed)* strains were maintained in the Cogentech zebrafish facility in compliance with national guidelines regarding animal welfare (Italian decree “4th March 2014, n°26”). Adult animals were used exclusively for breeding purposes. Fish were housed in a “Acquatic Habitats” husbandry system, in 3 l water tanks with a density of 0.2 l per fish and water parameters set as follows: temperature=28.5°C, pH=7 and conductivity=500 µS. The circadian rhythm imposed was 14 hours of light and 10 hours of darkness. Fish were fed three times a day with live shrimps of the species *Artemia salina* (MBK) and standard dry food (JBL).

Juvenile zebrafish were introduced in the housing system starting from 6 dpf. Juveniles (from 6 dpf to sexual maturity) were fed three times a day with dry *Artemia salina* shrimps (JBL) and standard dry food (Special Diets Services). Both juveniles and adults were monitored weekly to seek any sign of pain and distress. Suffering animals were euthanized by terminal anesthesia.

All the XT and imaging experiments presented in this study were performed on animals at larval stage. Zebrafish embryos (from zygote stage to 2 dpf) and *larvae* (from 2 dpf to 6 dpf) were obtained by natural mating of adult couples and developing fish were raised in Petri dishes filled with E3 water medium (5 mM NaCl, 0.17 mM KCl, 0.33 mM CaCl₂, 0.33 mM MgSO₄ and 0.05% methylene blue in ddH₂O), at a density of approximately 60 fish per plate. Animals were checked regularly for normal development: embryos and *larvae* showing morphological abnormalities were euthanized by terminal anesthesia. Starting from 18-22 hpf *larvae* were transferred to E3 water supplemented with 0.003% N-phenylthiourea (PTU, Sigma-Aldrich) to inhibit melanin formation and conserve optical transparency. E3 water + PTU was replaced daily. For cancer cell XT, *larvae* were maintained at 28.5°C until 2 dpf and kept at 34°C after XT, until 4 dpi.

3.2 Cell culture and manipulation

3.2.1 Cell lines

Cell lines used in this study were cultured with the purpose of transplantation. All cell lines were purchased from the American Type Culture Collection (ATCC) and cultured at 37°C in a humidified atmosphere containing 21% O₂ and 5% CO₂.

MDA-MB-231 human TNBC cells were cultured in DMEM (EuroClone), supplemented with 10% North American fetal bovine serum (EuroClone), 2 mM L-glutamine (EuroClone) and 100 U ml⁻¹ penicillin-streptomycin (Life Technologies). MDA-MB-231 were split twice a week once they reached 80-90% confluence.

MCF10A normal human breast epithelial cells were cultured in a 1:1 mixture of DMEM (EuroClone) and Ham's F12 containing L-glutamine medium (Gibco) supplemented with 5% horse serum (EuroClone), 50 ng ml⁻¹ cholera toxin (Sigma-Aldrich), 10 µg ml⁻¹ insulin (Roche), 500 ng ml⁻¹ hydrocortisone (Sigma-Aldrich) and 20 ng ml⁻¹ human epidermal growth factor (Tebu-Bio). MCF10A were split three times a week once they reached 80-90% confluence.

HEK 293T human embryonic kidney cells used for lentiviral infections were cultured in DMEM (Euroclone) supplemented with 10% South American fetal bovine serum (EuroClone), 2 mM L-glutamine (EuroClone) and 100 U ml⁻¹ penicillin-streptomycin (Life Technologies).

3.2.2 Vectors

The **Tet-Off-H2B-GFP** lentiviral vector (Figure 1) was kindly provided by Dr. T. Vlachou (Department of Experimental Oncology, European Institute of Oncology, Milan) [Falkowska-Hansen *et al.*, 2010]. It is a 3rd generation lentiviral vector that allows the constitutive expression of H2B-GFP fusion protein under the P_{tight} promoter. Upon doxycycline administration, H2B-GFP expression is repressed but, for the purposes of this study, this vector was used as a fluorescent nuclear reporter in XT experiments.

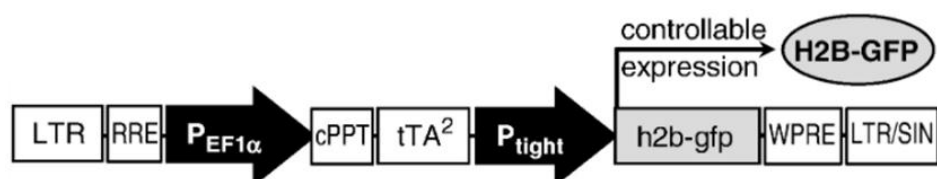


Figure 1 | Schematic representation of the Tet-Off-H2B-GFP lentiviral vector (Modified from Falkowska-Hansen *et al.*, 2010)

The **pRSI17-U6-sh-HTS6-UbiC-TagGFP2-2A-Puro** plasmid was purchased from Collecta and used to knock-down the expression of candidate metastasis-inducing genes in *in vivo* validation experiments (Figure 2). It is a 3rd generation lentiviral vector that allows the expression of a short hairpin RNA (shRNA) under the U6 promoter. This vector contains genes that encode for puromycin resistance and TagGFP reporter under the control of the UbiC promoter.

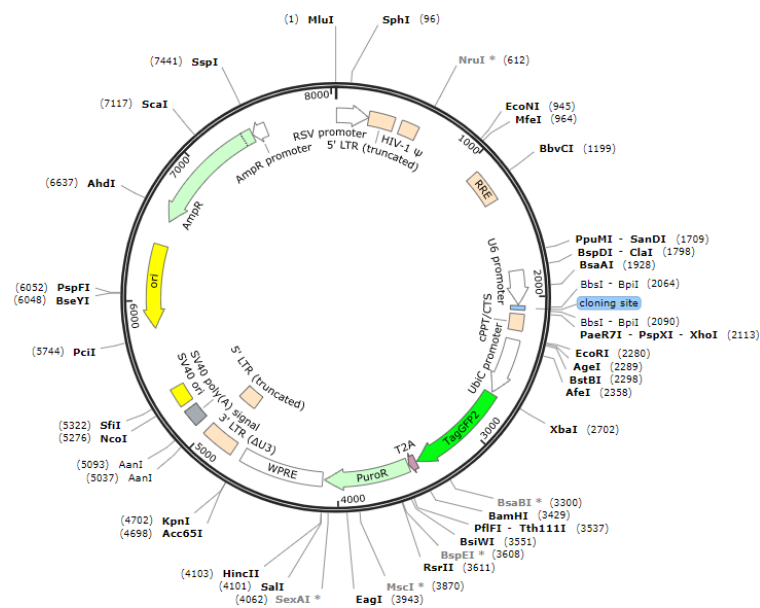


Figure 2 | Map of the pRSI17-U6-sh-HTS6-UbiC-TagGFP2-2A-Puro plasmid.

The **pMDLg/RRE** packaging vector was derived from HIV-1. It expresses the HIV-1 gene GAG (coding for virus structural proteins) and POL (coding for retrovirus specific enzymes) but lacks all the genes responsible for viral pathogenicity. This vector was used in combination with pRSV-Rev and pMD2.G VSV-G for lentivirus production with 3rd generation plasmids.

The **pRSV-Rev** packaging vector was derived from HIV-1. It expresses HIV-1 REV shuttle protein, that facilitates nucleus-to-cytoplasm RNA exportation. This vector was used in combination with pMDLg/RRE and pMD2.G VSV-G for lentivirus production with 3rd generation plasmids.

The **pMD2.G VSV-G** packaging vector was derived from Vesicular Stomatitis Virus. This vector was used in combination with pMDLg/RRE and pRSV-Rev for lentivirus production with 3rd generation transfer plasmids.

All the vectors were transformed and amplified in bacterial *E. coli* Stbl3 competent cells. Plasmid DNA was extracted with NucleoBond Xtra Maxi kit (Macherey-Nagel),

according to the manufacturer's instructions. Quantity and quality of the purified plasmid DNA were checked using NanoDrop ND-100 (Thermo Scientific).

3.2.3 shRNA constructs

Two copies of complementary oligonucleotides (sense and antisense strands) for each shRNA were obtained by Sigma-Aldrich and cloned into pRSI17-U6-sh-HTS6-UbiC-TagGFP2-2A-Puro vector. Sequences are reported in Table 1: gene-specific sequences (in bold) are separated by a standard hairpin loop sequence (in red); scrambled-shRNA was used as a control.

Table 1 | List of shRNA oligonucleotides used for functional gene validation.

| ID | Sequence (forward and reverse) |
|--------------------|--|
| ANGPTL4_sh#1 | ACCGGACGGTGACTCTTGGCTCTGCC GTTAATATTCATAGC GGCAGAGCCAAGAGTCACCGTTTTT CGAAAAAACCGTGACTCTTGGCTCTGCC CTATGAATATTAAC CGGCAGAGCCAAGAGTCACCGTC |
| ANGPTL4_sh#2 | ACCGGGACCACAAGCACCTAGACCAT GTTAATATTCATAGC ATGGTCTAGGTGCTTGTGGTCTTTT CGAAAAAAGACCACAAGCACCTAGACCAT GCTATGAATATTAAC ATGGTCTAGGTGCTTGTGGTCC |
| KCNQ1OT1_sh#1 | ACCGGGGTAGAATAGTTCTGTCTTAG GTTAATATTCATAGC CTAAGACAGAACTATTCTACCTTTT CGAAAAAAGGTAGAATAGTTCTGTCTTAG GCTATGAATATTAAC CTAAGACAGAACTATTCTACCC |
| KCNQ1OT1_sh#2 | ACCGGGCAGTTATTGAAACCTCTAC GTTAATATTCATAGC CGTAGAGGTTTCAATAACTGCTTTT CGAAAAAAGCAGTTATTGAAACCTCTAC GGCTATGAATATTAAC CGTAGAGGTTTCAATAACTGCC |
| ITGB4_sh#1 | ACCGGGAGGGTGTGCATCACCATTGAA GTTAATATTCATAGC TCAATGGTGATGACACCCTCTTT CGAAAAAAGAGGGTGTGCATCACCATTGAA GCTATGAATATTAAC TCAATGGTGATGACACCCTCC |
| ITGB4_sh#2 | ACCGGGGTACATGGTGGGCTTAA GTTAATATTCATAGC CTTAAAGCCCACCATGTGACCTTTT CGAAAAAAGGTACATGGTGGGCTTAA GCTATGAATATTAAC CTTAAAGCCCACCATGTGACCC |
| LY6E_sh#1 | ACCGGGCTTCTCCTGCTGTAACCAG GTTAATATTCATAGC TCTGGTTCAAGCAGGAGAAGCTTTT CGAAAAAAGCTTCTCCTGCTGTAACCAG GCTATGAATATTAAC TCTGGTTCAAGCAGGAGAAGCC |
| LY6E_sh#2 | ACCGGGGCATTGGGAATCTCGTGACA GTTAATATTCATAGC TGTCACGAGATTCCCAATGCCTTTT CGAAAAAAGGCATTGGGAATCTCGTGACA GCTATGAATATTAAC TGTCACGAGATTCCCAATGCC |
| IFI6_sh#1 | ACCGGGAGATGGGTTCCTACTATATT GTTAATATTCATAGCA ATATAGTGAGAACCATCTCTTTT CGAAAAAAGAGATGGGTTCTACTATATT GCTATGAATATTAACA ATATAGTGAGAACCATCTCC |
| IFI6_sh#2 | ACCGGCAACCTCCCAAGTAGGATTAC GTTAATATTCATAGC GTAATCCTACTTGGGAGGTTGTTTT CGAAAAACAACCTCCCAAGTAGGATTAC GCTATGAATATTAAC GTAATCCTACTTGGGAGGTTGC |
| FST_sh#1 | ACCGGGTGTGGTGGACCAGACCAATA GTTAATATTCATAGC TATTGGTCTGGTCCACCACCTTTT CGAAAAAAGTGTGGTGGACCAGACCAATA GCTATGAATATTAAC TCTGGTTCAAGCAGGAGAAGCC |
| FST_sh#2 | ACCGGAGTTGAGACTTGTAGACATTT GTTAATATTCATAGC AAATGTCTACAAGTCTCAACTTTTT CGAAAAAAGTTGAGACTTGTAGACATTT GCTATGAATATTAACA AAATGTCTACAAGTCTCAACTC |
| Scrambled sequence | ACCGGATATCTCGCAATGTTGGTGT GTTAATATTCATAGCA ACACCAACATTGCGAGATATTTTT CGAAAAAATATCTCGCAATGTTGGTGT GCTATGAATATTAACA ACACCAACATTGCGAGATATC |

3.2.4 Virus production

Packaging and delivery vectors were used for the production of 3rd generation lentiviral particles using calcium phosphate transient transfection. All transfections were performed using HEK293T cells at 70% confluence in 100 mm Petri dishes.

For the production of lentiviral particles containing the H2B-GFP reporter gene 10 μg of Tet-Off-H2B-GFP were mixed with 3 μg of pMD2.G VSVG, 5 μg of pMDLg/RRE, 2.5 μg of pRSV-Rev 3rd generation packaging vectors and CaCl_2 to a final concentration of 0.5 M.

For the production of lentiviral particles containing shRNAs 10 μg of pRSI17-U6-sh-HTS6-UbiC-TagGFP2-2A-Puro, in which a single gene-targeting shRNA was cloned, were mixed with 4 μg of pMD2.G VSVG, 5 μg of pMDLg/RRE, 3 μg of pRSV-Rev 3rd generation packaging vectors and CaCl_2 to a final concentration of 0.5 M.

The mix was added drop-wise to 500 μl of 2X HBS. HEK293T medium was supplemented with chloroquine to a final concentration of 25 μM to increase transfection efficiency. After 15 minutes of incubation at room temperature, the mix was added to the plates and incubated overnight (16 hours). Fresh medium was added to each HEK293T plate and lentiviral supernatant was harvested after 24 hours. Supernatant was filtered through a 0.22 μm filter in order to be used for cell transduction.

3.2.5 Virus transduction

Stable H2B-GFP transduction

In order to perform transduction with lentiviral particles carrying the H2B-GFP vector, 2×10^6 MDA-MB-231 and 1.5×10^6 MCF10A cells per plate were seeded the day before the infection in 100 mm Petri dishes in order to obtain approximately 70% confluence the morning after. MDA-MB-231 and MCF10A cells were infected by replacing the standard medium with the lentiviral supernatant in presence of 10 $\mu\text{g ml}^{-1}$ polybrene (Sigma-Aldrich) and were incubated for 4 hours. A second overnight infection round without polybrene was subsequently performed. GFP expression was assessed after 24 hours and GFP^{high} cells were selected by FACS-sorting and subsequently expanded *in vitro* to obtain stable fluorescently-labeled MDA-MB-231-GFP⁺, and MCF10A-GFP⁺ cells. Homogeneity of GFP expression among cells was conserved by frequently checking fluorescence levels during cell expansion passages and by performing FACS-sorting of GFP^{high} cells when needed.

Stable shRNAs transduction

Stable MDA-MB-231-GFP⁺ cells at 70% confluence were transduced with pRSI17-U6-sh-HTS6-UbiC-TagGFP2-2A-Puro lentiviral particles carrying either the single gene-targeting shRNA of interest or the scrambled construct, in a single round of infection with MOI (multiplicity of infection) equal to 0.5, in presence of 10 $\mu\text{g ml}^{-1}$ polybrene. Selection

of stable clones expressing the shRNA was performed through 72 hour-long selection with $1.5 \mu\text{g ml}^{-1}$ puromycin.

3.3 The zebrafish xenograft assay

3.3.1 Cell preparation

MDA-MB-231-GFP⁺ and MCF10A-GFP⁺ cells were harvested at 70% confluence and cell viability and number were assessed by trypan blue exclusion method. Cell preparations with <80% of viable cells were discarded. Cells were resuspended at a concentration of 1×10^5 cells μl^{-1} in either complete medium (MDA-MB-231-GFP⁺ cells) or in complete medium supplemented with 2 mM EDTA (MCF10A-GFP⁺), to prevent cell clumps. Cells were kept on ice for 1-2 hours during XT.

In functional validation experiments, the extent of gene knock-down was assessed by qPCR by comparing shRNA-infected cells with scrambled-infected cells. RNA was extracted with Quick-RNA Miniprep Kit (Zymo Research) and cDNA was generated with the ImProm-II Reverse Transcription System (Promega), according to the manufacturer's instruction.

3.3.2 Xenotransplantation

Zebrafish embryos were obtained by natural mating and selected at 0-4 hpf by removing unfertilized and abnormal embryos. Animals were left to grow at 28.5°C for 2 days, until they reached the elected stage for XT. Prior to injection, 2 dpf larvae were manually dechorionated and anesthetized with 0.016% tricaine in E3 water medium supplemented with PTU. Tricaine stock solution (4 mg ml^{-1}) is prepared dissolving 400 mg of tricaine powder (Ethyl-3-aminobenzoate methane-sulfonate salt, MS-222, Sigma-Aldrich) in 97.9 ml ddH₂O and 2.1 ml of 1 M Tris pH 9, adjusting pH at 7.4.

XT was performed under an Olympus SZX9 stereomicroscope using the pneumatic Picospritzer III micro-injector (Parker Instrumentation). Customized micro-injection needles were prepared pulling GC100T-15 borosilicate glass capillaries (1,0 mm outer diameter/0,78 mm inner diameter; Harvard Apparatus) using a P-97 micropipette puller device (Sutter Instruments) and the following customized parameters: heat=505; pull=60; velocity=60; time=100; air pressure=300. Injection capillary was loaded with 10 μl of cell suspension and installed on a manual micromanipulator (Narishige) in order to ensure fine

movements. The tip of the needle was manually broken off with fine tweezers in order to obtain a tip opening diameter of 5-10 μm .

Anesthetized *larvae* were displayed flat in a lateral orientation on a 3% agarose bed. Each *larva* was injected with 5 nl of cell suspension, approximately corresponding to 500 cells. The definitive number of cell to be injected in a single fish was determined by transplanting variable cell amounts (250-500-1000 cells) and choosing the number that allowed the formation of a primary tumor without causing excessive mortality. The volume of cell suspension to be transplanted (5 nl) was set before each round of transplantation by injecting cells on a concave glass slide filled with mineral oil: the diameter of the spherical drop was measured at a given magnification using a graduated scale inserted in the ocular lenses of the microscope and it was used to calculate drop volume.

Cells were microinjected with two different modalities:

- *intravenous injection*: transplantation into the circulatory system was performed by approaching the dorsal side of the *larva* with 45°-angled injection needle. The needle was inserted into the initial point of the DoC, where the vessel starts broadening over the YS. Cell were correctly transplanted when the volume within the duct transiently expanded, immediately after the injection pulse.
- *subcutaneous injection*: correct subcutaneous transplantation into the PVS was performed by approaching the dorsal side of the *larva* with 45°-angled injection needle and pointing the needle tip at the site of injection. PVS is a “virtual” pocket placed ventrally respect to the central axis of the fish. The needle was inserted gently in the space directly below the periderm, without penetrating in the YS, and cells were injected with minimal air pressure. Cell were correctly transplanted when the volume of the pocket transiently expanded, immediately after the injection pulse.

Considering the variability in post-transplantation death and in successful cell engraftment, approximately 100 *larvae* per condition were transplanted in a single round of injection. Following transplantation, *larvae* were transferred to E3 water + PTU, left to recover at 28.5°C for 30 minutes, then observed and selected for correct transplantation with a Nikon SMZ25 stereomicroscope. Dead, abnormal, non-injected or mis-injected *larvae*, were discarded. To reduce variability, *larvae* transplanted with insufficient or too high tumor loads were eliminated. Correctly injected xenografts were transferred to a 34°C incubator for the remaining experimental time-window, to meet the optimal temperature requirements for fish and mammalian cells.

At 1 dpi fish were subjected to a second rapid screening and dead or abnormal xenografts were discarded. Remaining animals were anesthetized and arrayed in 48-multi-

well plates for subsequent analyses. Each xenograft was kept separated from the others to allow for longitudinal analyses.

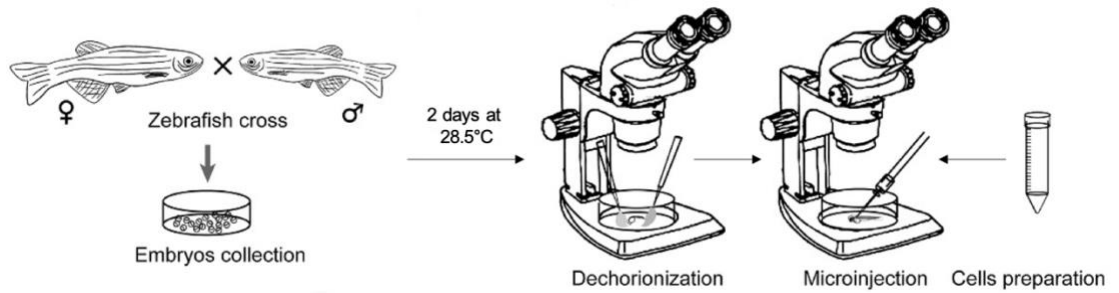


Figure 3 | Schematic representation of *larvae* XT procedure (modified from Ren *et al.*, 2017a)

3.3.3 Quantification of tumor implantation capacity

The percentage of both subcutaneously and intravenously injected xenografts that showed the presence of a primary tumor mass at the injection site was calculated at 4 dpi as follows:

$$\textit{Tumor implantation} (\%) = \frac{\textit{no. of xenografts with a tumor mass at 4 dpi}}{\textit{total no. of xenografts at 1 dpi}} \times 100$$

3.3.4 Quantification of metastatic potential

Metastatic potential was assessed on living *Tg(kdrl:DsRed)* xenografts with fluorescent vasculature, transplanted either in the PVS (subcutaneously) or in the DoC (intravenously), to distinguish between early and late metastatic events. Each xenograft was kept separated from the others in 48-multi-well plates, anesthetized and analyzed in order to quantify incidence, number and size of metastases, where a metastasis was defined as a cluster of at least 5 associated cells. Xenografted *larvae* were longitudinally analyzed at both 1 and 4 dpi.

The *incidence of metastasis* defines the number of xenograft that develop metastases and it was calculated as follows:

$$\textit{Incidence of metastasis} (\%) = \frac{\textit{no. of xenografts with at least one metastasis}}{\textit{total no. of xenografts}} \times 100$$

Overall frequencies of metastatic colonization were used to calculate two specific indexes, named Early Metastatic Potential (EMP) and Late Metastatic Potential (LMP),

according to the work of Fior and colleagues [Fior *et al.*, 2017]. Considering that maximum metastatic potential is reached with the intravenous transplantation, a possible reduction of metastasis in fish injected subcutaneously would indicate the effort to go through the early metastatic phases. Therefore, EMP and LMP were measured as follows:

$$LMP(\%) = \frac{\text{intravenously injected larvae with metastases}}{\text{all intravenously injected larvae}} \times 100$$

$$EMP(\%) = \frac{\frac{\text{subcutaneously injected larvae with metastases}}{\text{all subcutaneously injected larvae}}}{\frac{\text{intravenously injected larvae with metastases}}{\text{all intravenously injected larvae}}} \times 100$$

The quantification of the *average metastasis number* per xenografts takes into consideration all living xenografts.

The percentage of cancer cells endowed with metastatic properties was defined as the *frequency of metastasis initiating cells* and it was calculated at 4 dpi as follows:

$$Frequency\ of\ metastasis\ initiating\ cells\ (\%) = \frac{AVG\ no.\ of\ metastases}{AVG\ no.\ of\ cells\ in\ the\ primary\ tumor} \times 100$$

The *metastasis cellularity* is a parameter that indicates metastasis distribution with regard to their size in three categories defined as follows:

- Category 1: 5-10 cells (micro-metastases);
- Category 2: 10-20 cells (mid-size metastases);
- Category 3: >20 cells (overt metastases).

$$Metastasis\ cellularity\ (\%) = \sum_{Cat3}^{Cat1} \frac{\text{no. of metastases in a category}}{\text{total no. of metastases}} \times 100$$

The *metastatic burden* is an index that accounts for both the number and the size of metastases in a single xenograft. A size score was assigned to each of the category defined above: 0.5 for micro-metastasis (5-10 cells); 0.75 for mid-size metastasis (10-20 cells); 1.5 for overt metastasis (>20 cells). Size scores were arbitrarily chosen on the basis of their relevance in a hypothetical clinical context. Assuming that the score of each metastasis (S_i) in a single xenograft should be weighted by the total metastasis number in that xenografts (N), we introduced a coefficient whose value escalates as a sigmoidal function of metastasis number in a xenograft. Therefore, metastatic burden index was obtained applying the following equation :

$$\mathbf{Metastatic\ burden} = 1 + \sum_{i=1}^N S_i \times \frac{e^N}{K + e^N}$$

where S_i is the score of the i -th (from 1 to N) metastasis in a given xenograft and K corresponds to a constant calculated considering that the coefficient for the sigmoidal curve should be equal to 0.9 at the 90° percentile of metastasis number (corresponding to the 6 metastases/xenograft for MDA-MB-231 cells). In case of no metastases, the minimum value of the index is 1, which allows to calculate the increment of metastatic burden over time:

$$\mathbf{Metastatic\ burden\ increment\ (FC)} = \frac{\mathbf{metastatic\ burden\ at\ 4\ dpi}}{\mathbf{metastatic\ burden\ at\ 1\ dpi}}$$

3.4 Zebrafish whole mount immunofluorescence

For *ex vivo* analyses, zebrafish xenografts were euthanized with terminal anesthesia and fixed for 2 hours at room temperature (RT) in 4% paraformaldehyde in PBS (PFA, Sigma-Aldrich). For long-term storage, fixed *larvae* were dehydrated in a solution of methanol/PBS at increasing concentration (25%-50%-75%) and conserved in 100% methanol at -20°C.

For whole-mount immunofluorescence, xenografts were rehydrated in 75%-50%-25% methanol/PBS solutions and washed in either PBT (PBS + 0.2% Triton) or PSB-TT (PBS + 0.2% Triton + 0.2% Tween-20). Detergent concentration varied according to the increasing thickness of *larvae* from 1 to 4 dpi. 1 and 4 dpi xenografts were permeabilized by incubation in ice cold acetone for 15' or 30' respectively, rinsed in PBT or PBTT and transferred in 24-multi-well plates for 2 hours at RT in a blocking solution (1% bovine serum albumin + 5% donkey serum + 0.05% triton in PBS). Xenografts were incubated overnight at 4°C with primary antibodies diluted in blocking solution. Primary antibodies are listed below:

| Antigen | Working concentration | Commercial information |
|------------------------------|-----------------------|---------------------------------------|
| Ki67 | 1:100 | Rat, SolA15, Thermo Fisher Scientific |
| Human HLA | 1:100 | Rabbit, EP 1395Y, Abcam |
| Activated Caspase 3 (Asp175) | 1:100 | Rabbit, #9661, Cell Signaling |
| β-Galactosidase | 1:100 | Mouse, E2U2I #27198, Cell Signaling |
| LC3 | 1:100 | Rabbit, # ab48394, Abcam |

After several washes in PBT or PBTT, xenografts were incubated overnight at 4°C with secondary antibodies and DAPI (1:1000; Sigma-Aldrich) in blocking solution. Secondary antibodies are listed below:

| Antigen | Working concentration | Commercial information |
|----------------|------------------------------|---|
| Rat IgG | 1:400 | Donkey, Cy TM 3-conjugated, Jackson ImmunoResearch |
| Rabbit IgG | 1:400 | Donkey, AlexaFluor® 647, Jackson ImmunoResearch |
| Mouse IgG | 1:400 | Donkey, AlexaFluor® 647, Jackson ImmunoResearch |
| Rabbit IgG | 1:400 | Donkey, Cy TM 3-conjugated, Jackson ImmunoResearch |

After extensive washes in PBTw (PBS + 0.05% Tween-20), xenografts were post-fixed with 4% PFA for 20' at RT, washed in PBTw and flat-mounted with lateral orientation on glass slides in glycerol mounting medium (Sigma-Aldrich).

3.5 Histological evaluation of primary tumors

Zebrafish xenografts at 4 dpi were fixed for 2 hours at RT in 4% PFA in PBS and with lateral orientation in 2% low-melting-point agarose in PBS (EuroClone), prior to paraffin embedding. Fresh mouse MDA-MB-231 xenografts were formalin-fixed and paraffin-embedded with LogosJ Processor (Milestone). Mouse samples were a courtesy of the Molecular Pathology Unit of the European Institute of Oncology.

Samples were sectioned at 3 µm and stained with hematoxylin and eosin every five slides. Immunohistochemistry staining was performed using Bond III IHC auto-stainer for fully automated immunohistochemistry (Leica Biosystems). Heat-induced epitope unmasking was performed at 100°C for 20' using Tris-EDTA at pH9 (Bond Epitope Retrieval Solution 2) for all antigens, with the exception of human Nuclei antigens, which was unmasked in sodium citrate at pH6 (Bond Epitope Retrieval Solution 1). All the antibodies were diluted with Bond Primary Antibody Diluent. Bond IHC Polymer Detection Kit was used for chromogenic reaction. All IHC reagents were purchased from Leica Biosystems and used accordingly to manufacture's instruction. Images were acquired with Aperio ScanScope XT instrument at 20x/0.75 N.A. (Leica Biosystems) magnification. Primary antibodies are listed below:

| Antigen | Working concentration | Commercial information |
|----------------|-----------------------|-----------------------------|
| Human Nuclei | 1:200 | Mouse, MAB4383, Millipore |
| Ki67 | 1:200 | Rabbit, SP6 ab16667, Abcam |
| Cytokeratin 5 | 1:1000 | Rabbit, EP1601Y, Abcam |
| Cytokeratin 18 | 1:100 | Mouse, sc-51582, Santa Cruz |

3.6 Imaging and quantification

3.6.1 Stereomicroscopy

In order to quantify tumor implantation and metastatic potential, 1 and 4 dpi living xenografts were arrayed in 48-multi-well plates, immobilized with few drops of 0.0016% tricaine in E3 water + PTU and analyzed with a Nikon SMZ25 stereomicroscope. Xenografts were observed with 1x/N.A. 0.15-W.D. 60 mm Planapo objective, using a 50x zoom. Samples were excited with Lumencor SolA SE U-nIR fluorescent illuminator in order to detect GFP and DsRed signals from cancer cells and zebrafish endothelium respectively.

3.6.2 Confocal microscopy

Confocal imaging was performed with a Leica SP8 AOBS microscope.

For *live imaging*, 1 and 4 dpi xenografts were anesthetized with 0.0016% tricaine in E3 water + PTU and immobilized in a lateral orientation in 0.8% low-melting point agarose dissolved in E3, on a glass-bottom chamber slide (35 mm dish with 14 mm glass diameter; MatTek). E3 water + PTU supplemented with tricaine was then added to the imaging chamber to keep *larvae* anesthetized over the course of the acquisition and prevented the sample from drying out. Z-stacks tile scan images of the whole *larva* were acquired with a 10x/0.3 N.A. dry objective. Magnifications of the anterior and caudal portions of the *larva* were acquired with a 25x/0.95 N.A. water immersion objective, with 5 μ m z-stack interval, in resonant scanner modality. Samples were simultaneously excited with 488 nm and 561 nm lasers to acquire signals from GFP⁺ cancer cells and DsRed⁺ zebrafish endothelial cells. Transmitted light was also recorded. Merging of image tiles was obtained using the *Mosaic Merge* function of the Leica LasX software.

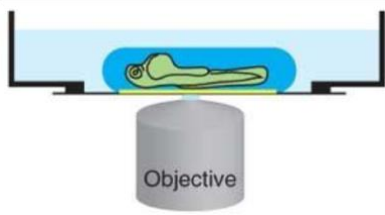


Figure 4 | Agarose mounting immobilization method for live imaging of zebrafish xenografts. The *larva* is placed in the center of a 35 mm glass-bottom dish (yellow line) and embedded in low-melting point agarose (navy blue). The *larva* is covered with E3 water supplemented with tricaine (light blue) to prevent the sample from drying out (modified from Renaud, Herbomel and Kissa, 2011).

For *ex vivo* imaging (whole-mount immunofluorescence), 1 and 4 dpi fixed xenografts were mounted in lateral orientation on a glass slide in glycerol mounting medium, with the glass coverslip facing the objective. Z-stack images were acquired with a 25x/0.95 N.A. water immersion objective with 2 μm z-stack interval, in resonant scanner modality. Samples were sequentially excited with 488 nm laser to acquire signals from GFP⁺ cancer cells, 405 nm laser to acquire DAPI stained nuclei, 561 nm and 633 nm lasers to acquired signals from antigens respectively marked by CyTM3-conjugated and by AlexaFluor[®] 647-conjugated secondary antibodies.

A complete overview of the microscopes used in this study and their applications is reported in Table 3.

Table 3 | List of the microscopes and their applications.

| Microscope | Application |
|------------------------------------|--|
| Olympus SZX9 stereomicroscope | Xenotransplantation Agarose inclusion for histological analysis Sample preparations for <i>in vivo</i> and <i>ex vivo</i> confocal imaging |
| Nikon SMZ25 stereomicroscope | Screening of transplanted fish after injection Quantification of tumor implantation and metastatic potential at 1 and 4 dpi |
| SP8 AOBS Leica confocal microscope | Whole-mount IF on zebrafish xenografts Representative live images of zebrafish xenografts |
| Aperio ScanScope XT | H&E/IHC on zebrafish and mouse tumor xenograft sections |

3.6.3 Image analysis

For the sake of visual clearness, all z-stacks images underwent brightness/contrast adjustments and noise filtering with Fiji/ImageJ software. Maximum intensity projections of confocal images of living xenografts were obtained with Leica LasX software.

Quantification of primary tumors cellularity and proliferative index were performed on confocal z-stack IF images with Arivis Vision 4D 3.5.0 software, using a customized pipeline. Images were first subjected to a denoising step via “*particle enhancement*” and “*gaussian filter*” functions and then segmented via “*blob finder*” option on the GFP channel. All the segmented objects that met given requirements of volume and sphericity were considered as GFP⁺ nuclei. A value of Ki67 fluorescent intensity for each GFP⁺ cell was then calculated. For each image, I set a mean intensity threshold for the Ki67 channel above which a cell was considered Ki67⁺. Proliferative index (%) was computed as the number of Ki67⁺ cells over the total number of GFP⁺ cells.

Primary tumor volume was measured in confocal z-stack IF images considering the sum of nuclear GFP and human HLA membrane signals, using a customized Fiji/ImageJ pipeline. Volume was obtained by quantifying the area occupied by the primary tumor for each stack, computing the sum of all the areas and multiplying for the z-step. Mitotic figures and activated caspase 3 positive cells were manually quantified in all slides. All the analysis pipelines were optimized in collaboration with the Imaging Unit staff of the European Institute of Oncology.

3.7 Drug treatment and efficiency evaluation

Several Cisplatin concentrations (from 0 to 35 μM in E3 water) were tested on non-injected *larvae* for 3 consecutive days at 34°C. 23 μM was defined as maximum tolerated dose (MTD), since it did not cause mortality or abnormal phenotypes in 80% of tested animals. Cisplatin was kindly provided by the European Institute of Oncology Pharmacy as 1 mg ml⁻¹ clinical formulation.

Dose-response curves were defined also for Paclitaxel (clinical formulation), PI3K-inhibitor LY294002 (#S1105, Selleckchem) and the mTORC1-inhibitor Everolimus (RAD001, #S1120, Selleckchem), identifying 100 nM, 20 μM and 10 μM respectively as working concentration.

Zebrafish *larvae* were injected with MDA-MB-231-GFP⁺ cells at 2 dpf as previously described. Drugs were administered starting from 1 dpi to zebrafish xenografts with comparable tumor size. Approximately 50 xenografts were randomly distributed to control

or treatment groups, arrayed at a density of 5 fish/well in 24-multi-well plates. Drugs were replaced daily until 4 dpi.

3.8 Statistical analysis

GraphPad Prism software (version 9.2.0) was used for statistical analyses. All datasets were tested for normal distribution. Normally distributed datasets were analyzed with unpaired *t* test or one-way analysis of variance (ANOVA) followed by post-hoc test for multiple comparisons. Non-normally distributed datasets were analyzed by Mann-Whitney test or Kruskal-Wallis tests, followed by post-hoc test for multiple comparisons. Pairwise Chi-square test or *z* score test (<https://www.socscistatistics.com/tests/ztest/>) were used to analyze the differences between categorical distributions. Results are expressed as AVG±SEM or median±95%CI. P values (*P*) <0.05 were considered to be statistically significant (ns= not significant; **p*<0.05; ***p*<0.01; ****p*<0.001; *****p*<0.0001).

4. Results

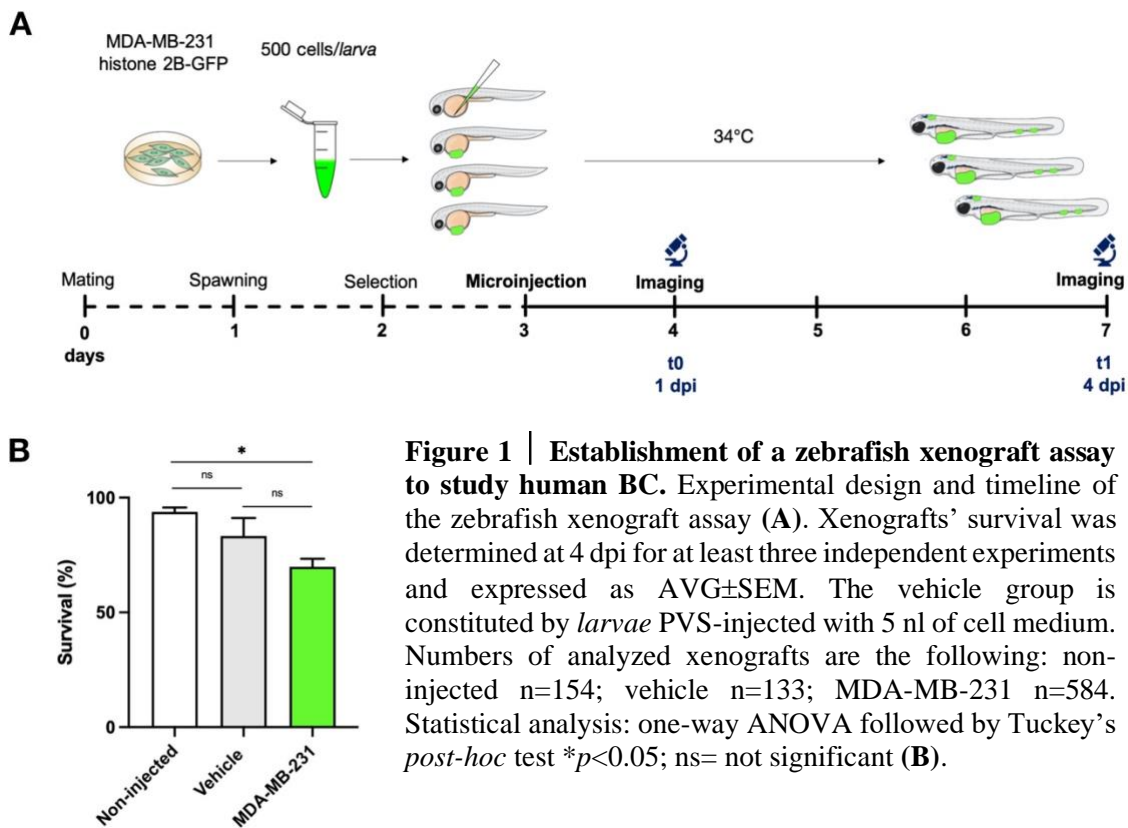
4.1 Establishment of a zebrafish xenograft model of human metastatic BC

4.1.1 Experimental design

The xenotransplantation (XT) procedure involves microinjection of ~500 human MDA-MB-231 cells in the PVS of 2 dpf zebrafish *larvae*. Injection in the PVS, a “virtual” pocket located between the periderm and the YS, resembles the “subcutaneous” transplantation performed in mice. The MDA-MB-231 cell line, established from a TNBC patient and highly tumorigenic and invasive in murine models [Iorns *et al.*, 2012], was stably engineered to express the histone 2B-GFP reporter fusion protein. Due to their nuclear fluorescent signal, viable cells were detectable throughout the transparent larval body and easily counted. Stable transgenesis was preferred respect to cell labeling using a vital dye, since it allows the maintenance of GFP expression through cell divisions and the unequivocal distinction of viable cells from dying ones or debris. On the contrary, lipophilic membrane dyes dilute during proliferation, have a restricted half-life and cannot be used as a reliable counterstaining. *Larvae* are incubated at 34°C for the entire length of the experiment and analyzed at 1 and 4 dpi. Considering the 3 days required for mating of adult fish, spawning, collection and selection of fertilized embryos prior to transplantation, my zebrafish xenograft assay has a total length of 7 days. Experimental design and timeline are illustrated in detail in Figure 1A.

First, I investigated whether zebrafish *larvae* tolerate the invasive manipulations required by the XT procedure and the increased incubation temperature, assessing their survival at 4 dpi (Figure 1B). Examination of anesthetized animals under the stereomicroscope revealed that ~70% of MDA-MB-231-injected fish survive till the end of the assay without showing visible developmental abnormalities, confirming that *larvae* tolerate the procedure. The rate of survival of MDA-MB-231 or vehicle injected xenografts was similar (69.8 ± 3.55 vs. $83.3 \pm 7.3\%$; $p=0.1706$), whereas it is slightly, yet significantly, reduced respect to non-injected *larvae* maintained in the same conditions (69.8 ± 3.55 vs. $93.8 \pm 1.9\%$; $p=0.0125$), possibly due to the combination of mechanical stress and formation of cell clumps in larval capillaries. Mechanical stress of the microinjection and non-physiological temperature *per se*, however, did not appear to have a negative effect on

survival, as demonstrated by the comparison of survival rates between the two control groups (83.3±7.3% vs. 93.8±1.9%; $p=0.4587$).



4.1.2 Implantation and local growth are properties of the transformed phenotype

Once mastered the cell microinjection procedure and optimized the experimental parameters, I tested whether only the transformed cells implant after XT, comparing MDA-MB-231 with MCF10A not-transformed mammary epithelial cells. MCF10A cells were engineered to express the fluorescent nuclear reporter H2B-GFP (MCF10A-GFP⁺) and, as for MDA-MB-231, ~500 MCF10A-GFP⁺ cells were transplanted in the PVS of 2 dpf wild-type *larvae*.

Implantation potential of human cancer cells in zebrafish *larvae* was quantified as the percentage of xenografts which developed a cell mass at the injection site (≥ 30 cells) at 4 dpi, over total numbers of microinjected *larvae*. For the highly tumorigenic MDA-MB-231 BC cell line, I observed positive tumor implantation in ~83% of the animals (82.6±3.8%). Average volume of primary tumors (PTs) at 4 dpi was $1.12 \times 10^6 \pm 0.11 \mu\text{m}^3$, with an average number of cells equal to 211 ± 15 (Figure 2C). I further confirmed

successful implantation of MDA-MB-231 cells by immunohistochemistry analysis of human nuclei in 4 dpi xenografts (Figure 2B), exploiting a common histological marker to identify human cells in xenograft models.

On the contrary, MCF10A cells never originated a tumor mass, with only a modest percentage of fish ($18.1 \pm 9.03\%$) showing cell aggregates (between 5 and 30 living cells; Figure 2A). In both cell lines, *larvae* that did not develop a PT within 1 dpi remained tumor-free up to 4 dpi. Therefore, implantation potential reflects the tumorigenic origin of injected cells, recapitulating their behavior in mouse xenografts.

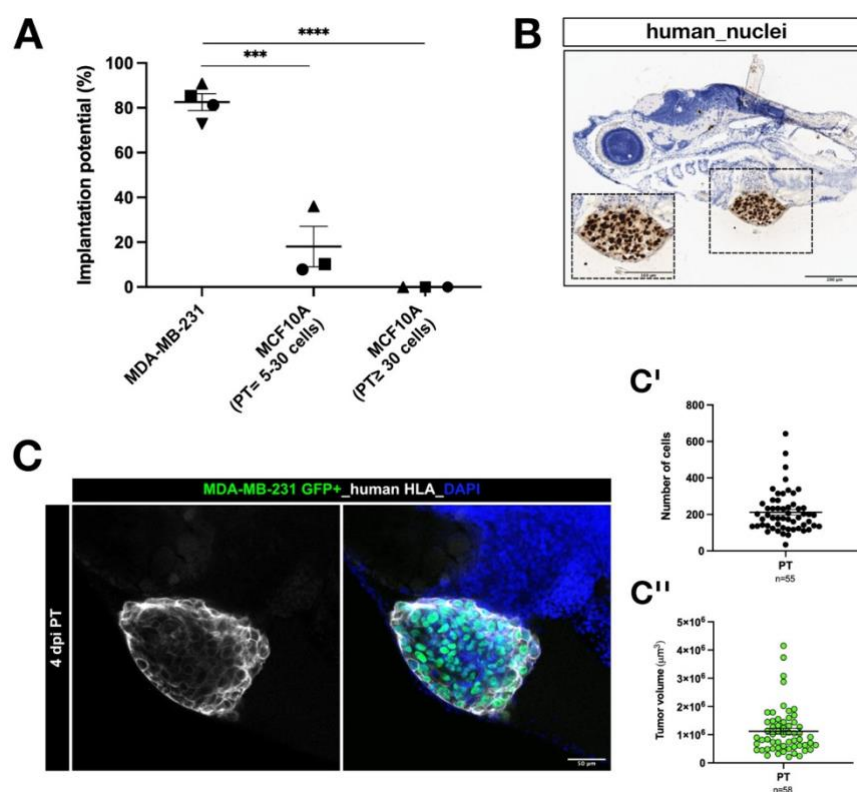


Figure 2 | The zebrafish host sustains implantation and growth of only malignant cells. Implantation potential was measured at 4 dpi. Results are expressed as $\text{AVG} \pm \text{SEM}$ for at least three independent experiments; each symbol in the dot plot represents a single experiment. Numbers of analyzed xenografts are the following: MDA-MB-231 $n=172$; MCF10A $n=43$. Statistical analysis: one-way ANOVA followed by Tukey's *post-hoc* test (**A**). Representative image of immunohistochemical staining for anti-human nuclei on 4 dpi MDA-MB-231 xenografts, scale bar= $200 \mu\text{m}$; dashed box: magnified area, scale bar= $100 \mu\text{m}$; $n=17$ (**B**). Representative confocal image of whole-mount immunofluorescence staining for human HLA on 4 dpi PTs. Green: human BC cell nuclei; white: human BC cell membranes; blue: DAPI; scale bar= $50 \mu\text{m}$. The image represents a single plane (**C**). MDA-MB-231-GFP⁺ cells count was performed on z-stack confocal images with Arivis Vision 4D 3.5.0 software. Results are expressed as $\text{AVG} \pm \text{SEM}$ for at least three independent experiments; each symbol in the dot plot represents a single xenograft; $n=32$ (**C'**). PT volume was measured with Fiji/ImageJ. Results are expressed as $\text{AVG} \pm \text{SEM}$ for at least three independent experiments; each symbol in the dot plot represents a single xenograft; $n=58$ (**C''**). *** $p < 0.001$, **** $p < 0.0001$

4.1.3 MDA-MB-231 zebrafish xenografts display same proliferative properties and morphology as in mouse

After showing that zebrafish *larvae* allow the successful establishment of human breast tumors, I evaluated whether MDA-MB-231 cells are viable and retain their proliferative capacity upon grafting into the zebrafish host. To this end, I analyzed expression of the proliferative marker Ki67 and the presence of mitotic figures in PTs by whole-mount immunofluorescence on both 1 and 4 dpi xenografts. Percentages of GFP⁺/Ki67⁺ nuclei were measured on confocal z-stack images, performing three-dimensional objects segmentation and count, while mitosis were quantified manually in each stack. 1 dpi PTs showed a high proliferative potential, with >60% of Ki67⁺ cells, thus demonstrating that MDA-MB-231 cells actively proliferate since the first hours post-transplantation (Figure 3A, upper panel). At 4 dpi, MDA-MB-231 cells still expressed Ki67 (Figure 3A, lower panel), although with a lower proliferative index ($30.5 \pm 2.9\%$ at 4 dpi vs. 61.6 ± 3.7 at 1 dpi; $p < 0.0001$; Figure 3B). Frequencies of Ki67⁺ cells in zebrafish PTs are similar to those observed upon injection of the same cells in mice (~40-45%).

Likewise, percentages of mitotic figures were relatively high at 1 dpi and decreased at 4 dpi ($4.02 \pm 0.56\%$ vs. $1.03 \pm 0.13\%$; $p < 0.0001$; Figure 3C). The significant reduction in cell proliferation observed at 4 dpi respect to 1 dpi might reflect the acquisition of a more quiescent phenotype over time, as also observed in mice xenografts (unpublished data from our laboratory).

Remarkably, the grafted MDA-MB-231 PTs showed very-low frequencies of cells expressing the apoptotic marker activated-caspase 3 ($0.75 \pm 0.14\%$ at 4 dpi, Figure 3D) that, together with their high proliferative potential, demonstrates a very low level of basal cell death for this cell line in zebrafish xenograft PTs (Figure 3D). These results also suggest that the decreased incubation temperature does not negatively impact on cancer cell survival in the host. Thus, upon engraftment in the zebrafish *larva*, MDA-MB-231 human BC cells are viable, actively proliferate and manifest modalities of growth similar to those reported in mouse xenografts.

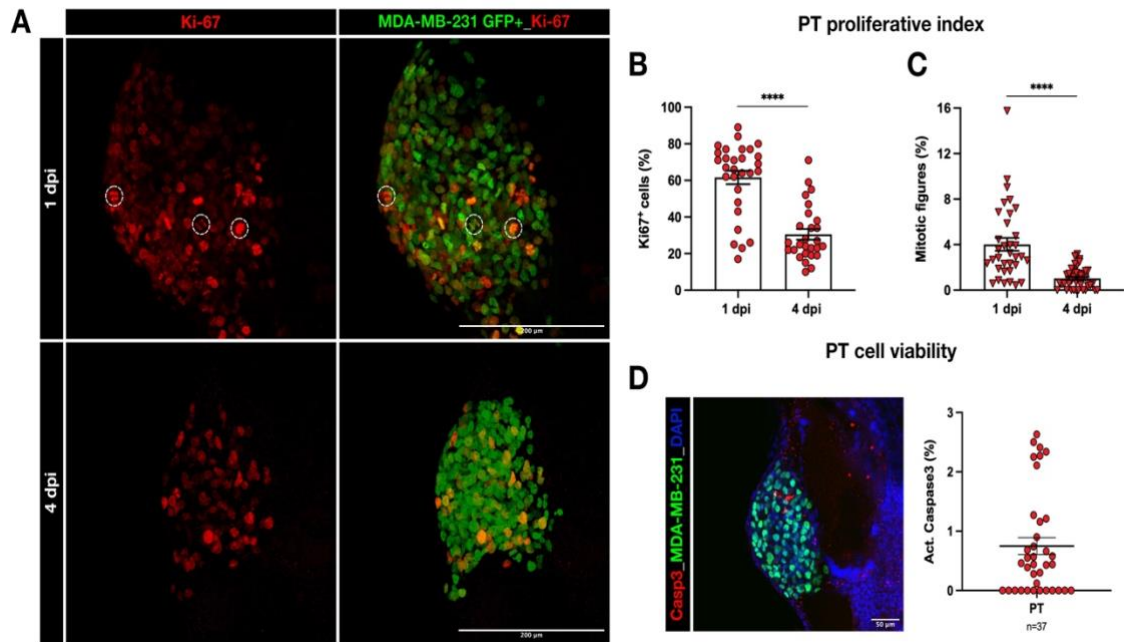


Figure 3 | MDA-MB-231 human BC cells are viable and actively proliferate in zebrafish xenografts. Representative confocal images of whole-mount immunofluorescence staining for Ki67 on 1 dpi and 4 dpi PTs. Circles highlight mitotic figures. Green: human BC cell nuclei; red: Ki67; scale bar= 200 μ m. All images are z-stacks maximum projections and were acquired at the same magnification (A). Quantification of % Ki67 was performed using Arivis Vision 4D 3.5.0 software. Results are expressed as AVG \pm SEM of at least three independent experiments. Each dot represents a xenograft. Numbers of xenografts analyzed are: 1 dpi, n=29; 4 dpi, n=27. Statistical analysis: Mann-Whitney test (B). Mitotic figures were quantified slide by slide. Results are expressed as AVG \pm SEM of at least three independent experiments. Each dot represents a xenograft. Numbers of xenografts analyzed are: 1 dpi, n=34; 4 dpi, n=42. Statistical analysis: Mann-Whitney test (C). Representative confocal images of whole-mount immunofluorescence staining for activated-caspase 3 on 4 dpi PTs; green: human BC cell nuclei; red: act. caspase 3; blue: DAPI. scale bar= 50 μ m. The image represents a single plane. Apoptotic cells were quantified slide by slide; Results are expressed as AVG \pm SEM. Each dot represents a xenograft; n=37 (D). **** p <0.0001.

Finally, I investigated whether breast tumors grafted in zebrafish *larvae* maintain the immunohistochemical and morphological features described for MDA-MB-231 tumors growing in mice. I performed hematoxylin and eosin staining and immunohistochemistry on paraffin-embedded samples obtained from 4 dpi zebrafish xenografts and 4 weeks mouse xenografts. MDA-MB-231 cells gave rise to poorly differentiated adenocarcinomas in both zebrafish and in mice (Figure 4A-A''), with comparable frequencies of Ki67⁺ cells (Figure 4B-B''). Zebrafish and murine PTs showed similarly high levels of expression of the luminal epithelial marker cytokeratin 18 (Figure 4C-C') and no expression of the basal marker cytokeratin 5 (Figure 4D-D'). Thus, zebrafish xenografts of MDA-MB-231 cells retain the same morphology and BC marker expression of the mouse counterpart.

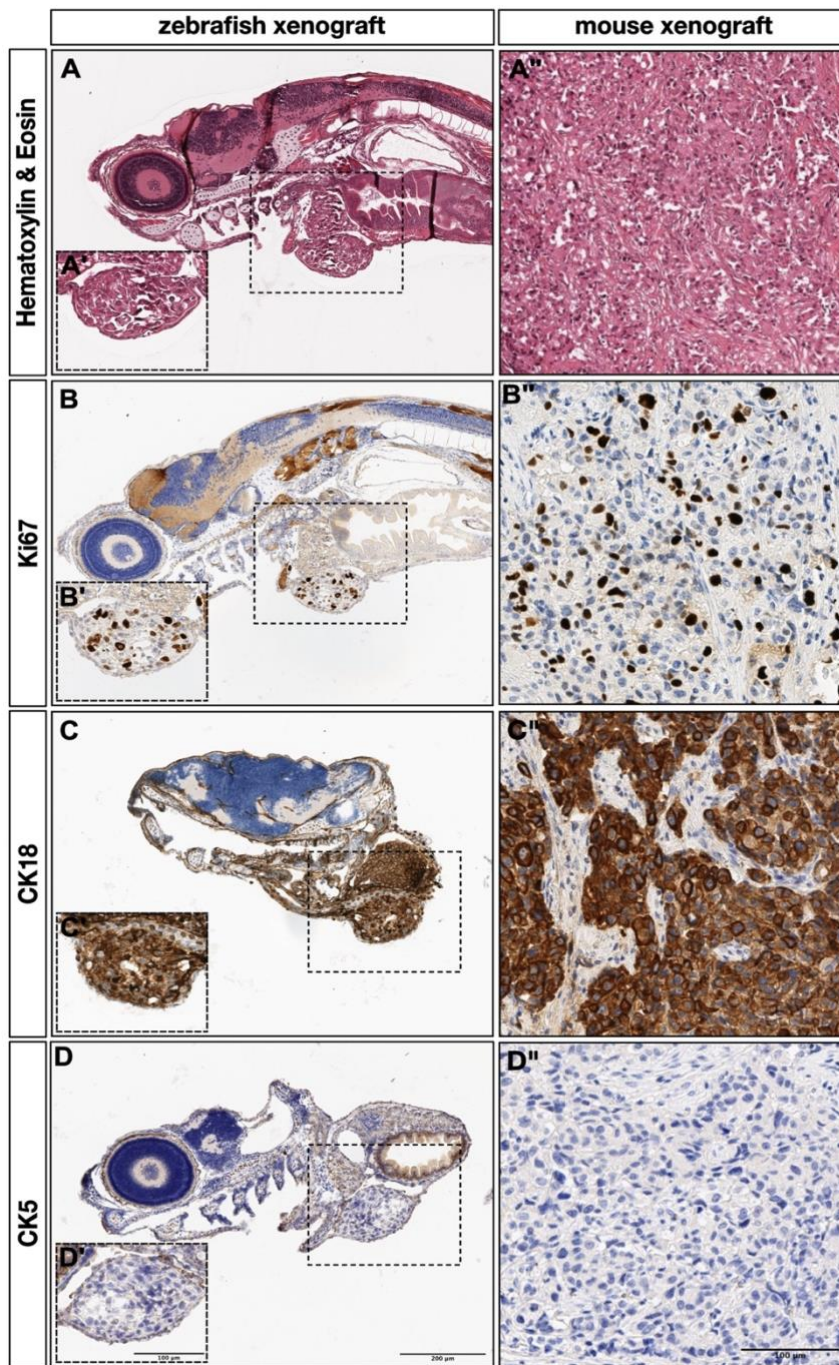


Figure 4 | Zebrafish xenografts conserve the same histochemical profile described for MDA-MB-231 cells, showing no differences respect to the murine model. Histological analysis of PTs of 4 dpi MDA-MB-231 zebrafish xenografts (**left**) and MDA-MB-231 mouse xenografts (**right**), performed on histological sections. H&E staining; n=20 (**A-A''**). IHC for Ki67; n=10 (**B-B''**), cytokeratin 18; n=5 (**C-C''**) and cytokeratin 5; n=5 (**D-D''**). **A-D**: Zebrafish anterior portions; scale bar= 200 μ m. **A'-D'**: magnified areas depicting zebrafish PTs; scale bar= 100 μ m. **A''-D''**: mouse xenografts; scale bar= 100 μ m.

4.1.4 Dissemination of mammary cells in the zebrafish host is a property of the transformed phenotype

Dissemination is a critical hallmark of cancer. Thus, I investigated frequency of seeding at distant sites in zebrafish xenografts and whether it represents a specific feature of malignant cells. I injected MDA-MB-231-GFP⁺ or MCF10A-GFP⁺ cells in the PVS, imaged each *larva* at 1 and 4 dpi, and quantified disseminated cells. GFP-nuclear signal was used as counterstaining. Notably, due to their optical clarity and small size, zebrafish *larvae* enable unrivalled *in vivo* cellular resolution even at low magnification.

Visual inspection of *larvae* showed sparse cells in the eye, head, blood vessels and caudal hematopoietic tissue (CHT), a region that represents a “hot spot” for cancer cell homing [Tulotta *et al.*, 2016; Paul *et al.*, 2019]. Disseminated cells were few at the earliest time point in both cell types, while they increased progressively over time in the cephalic and caudal areas only for MDA-MB-231 xenografts, while PT grew in volume (Figure 5A,B upper panels).

In contrast, numbers of MCF10A disseminated cells dramatically decreased at both the injection site, where they almost completely disappeared as early as 1 dpi, and in the rest of the body (Figure 5A,B lower panel). MCF10A disseminated cells presented pyknotic and fragmented nuclei, typical features of apoptotic cells. These cells were excluded from counting (Figure 5A'-A'').

Quantification of cell numbers revealed a dramatic difference between MDA-MB-231 and MCF10A xenografts at both 1 and 4 dpi (Figure 5C-D). High metastatic BC cells persisted in the host outside the injection site till the end of the assay (median at 4 dpi: 54 cells with 95%CI [37,93]), whereas the fluorescent signal of normal epithelial cells progressively regressed (median at 4 dpi: 5 cells with 95%CI [1,6] cells; $p < 0.0001$). These findings confirm that non-malignant MCF10A mammary cells fail to engraft and survive in zebrafish *larvae*, as in the murine model. Furthermore, this simple assay allows to assess the overtime dissemination efficiency of a cell line, which correlates with its metastatic potential.

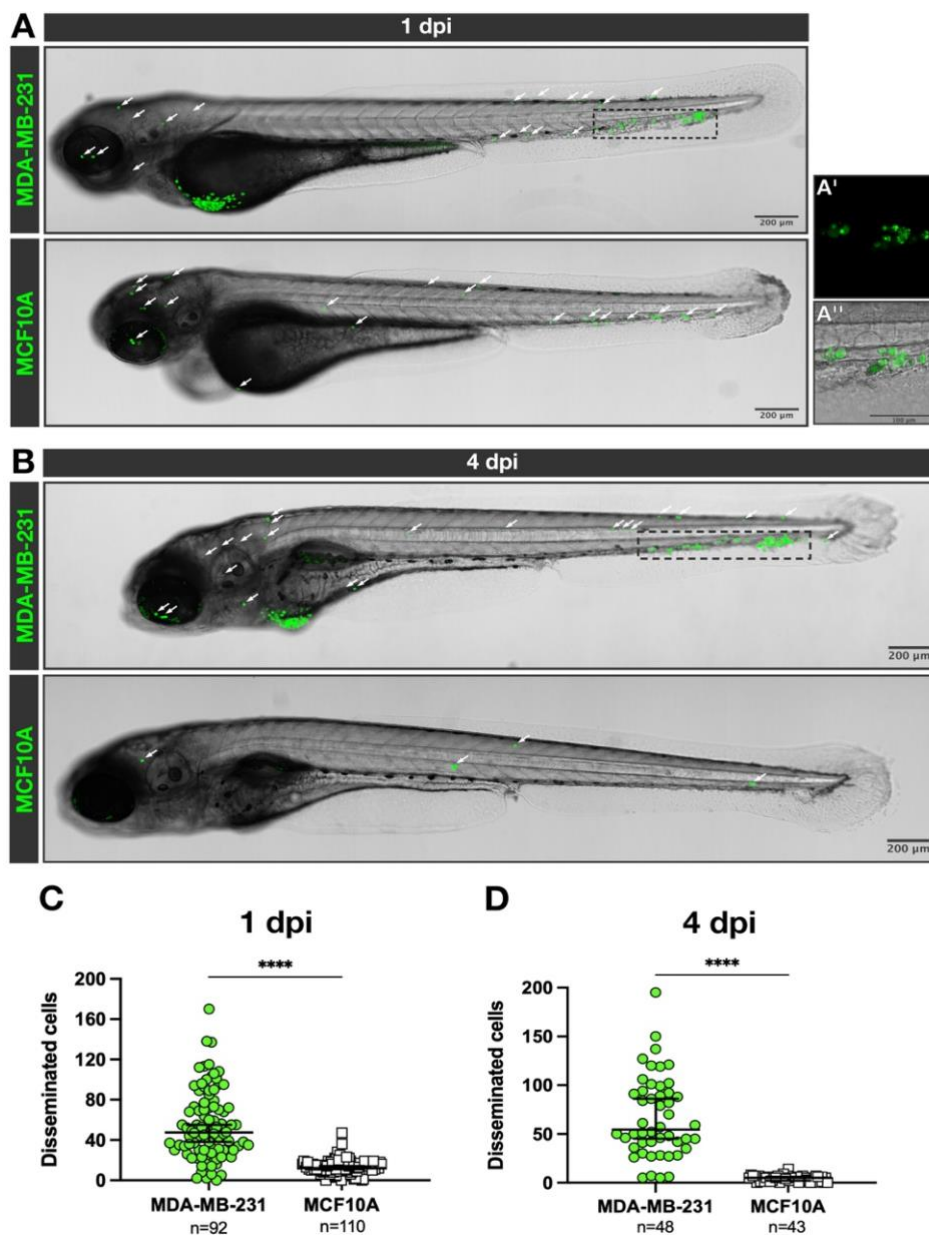


Figure 5 | MDA-MB-231 human BC cells disseminate outside the PT over time in zebrafish xenografts. Representative z-stack confocal images of live xenografts show the invasive behavior of MDA-MB-231 cells at 1 dpi (**A, upper panel**) and 4 dpi (**B, upper panel**). Dashed boxes: CHT; scale bar= 200 μ m. MCF10A cell dissemination in 1 dpi (**A, lower panel**) and 4 dpi (**B, lower panel**) xenografts show a decrease in disseminated cells, which also present apoptotic features (**A'-A''**). Scale bar= 200 μ m (whole view); 100 μ m (magnification). Disseminated cells were quantified with the stereomicroscope at 1 dpi (**C**) and 4 dpi (**D**). Results are expressed as median \pm 95%CI of at least three independent experiments. Each dot represent a xenograft. Number of xenografts analyzed for MDA-MB-231 cells are: 1 dpi n=92; 4 dpi n=48. Number of xenografts analyzed for MCF10A cells are: 1 dpi n=110; 4 dpi n=43. Statistical analysis: Mann-Whitney test; **** p <0.0001.

4.1.5 Intravenous transplantation of MDA-MB-231 BC cells leads to the development of extravascular metastases in the zebrafish host

I then assessed metastatic formation in zebrafish xenografts upon transplantation of MDA-MB-231-GFP⁺ cells directly in the circulation of 2 dpf *larvae* (~500 cells per fish). I imaged each *larva* separately at 1 and 4 dpi and I checked the presence of metastatic lesions, considering as a metastasis every extravasated cell cluster consisting of at least 5 cells. I quantitated numbers of metastases per fish, average numbers of metastases (including also the xenografts that did not develop any metastases) and the incidence of metastasis, expressed as the percentage of xenografts with at least one secondary mass over the total number of xenografts.

Already at 1 dpi, MDA-MB-231-injected fish presented 1 to 5 metastases per *larva* (Figure 6A upper panel, B-B''), with an average number of 1.03 ± 0.13 (Figure 6E; only ~54% of fish showed metastases) and an incidence of $53.8 \pm 4.2\%$ (Figure 6D). Metastases were mostly located in the caudal region and, less frequently, in the trunk, optic cup and brain. At 4 dpi I observed a significant increment in metastasis incidence ($53.8 \pm 4.2\%$ vs. $76.8 \pm 5.9\%$; $p=0.0014$; Figure 6D), a two-folds increase of average metastasis number (1.03 ± 0.13 vs. 2.32 ± 0.2 ; $p=0.0002$; Figure 6E), with numbers of metastases/fish ranging from 1 to 8.

MCF10A-GFP⁺ cells were injected in the circulation with the same modalities described above for MDA-MB-231, as a control. At 1 dpi, most injected cells were found in the caudal blood vessels as single cells, as already described in paragraph 4.1.4 (Figure 6A lower panel, C), with very few small micro-metastatic clusters (Figure 6E) observed in $17.3 \pm 4.8\%$ of injected fish (Figure 6D). At 4 dpi, both disseminated single cells and clusters almost completely disappeared, again demonstrating that in zebrafish larval xenografts MCF10A cells do not survive in circulation, neither are able to form metastases. MDA-MB-231 cells, on the contrary, conserve their highly metastatic phenotype, thereby providing a xenograft model to study metastatic BC progression *in vivo* in an extremely short time-window.

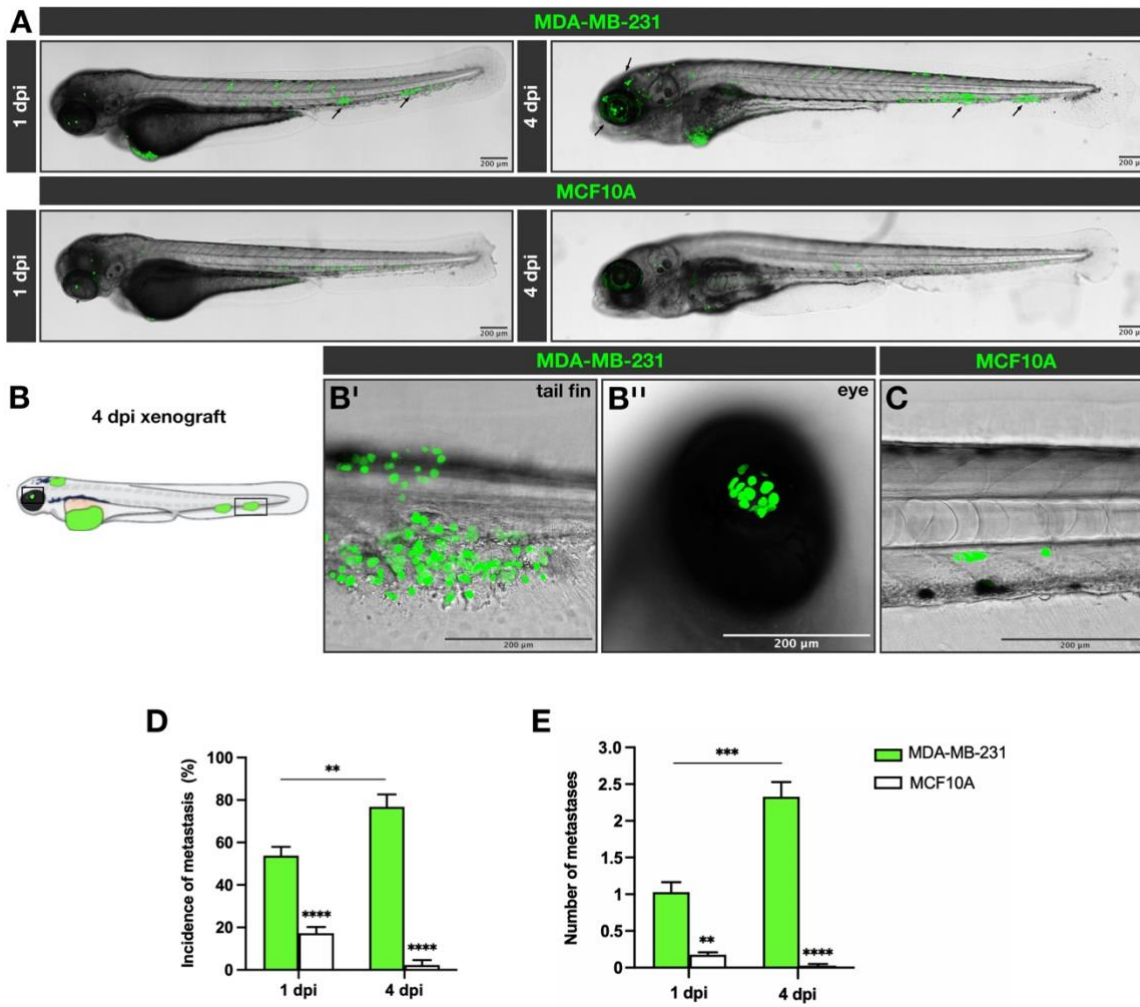


Figure 6 | Intravascular transplantation of MDA-MB-231 human BC cells induces extravasation and metastasis formation in zebrafish xenografts. Representative z-stack confocal images of live xenografts at 1 dpi and 4 dpi show that metastatic MDA-MB-231 cells are dispersed throughout the fish body and form metastases as indicated by arrows (**A, upper panel**), whereas for MCF10A few clusters of cells are observed at 1 dpi but none are detected at 4 dpi (**A, lower panel**). Scale bar= 200 μ m. Magnifications display metastases and extravasated clusters in MDA-M-231 (**B-B''**) and MCF10A (**C**) xenografts. Scale bar= 200 μ m. Incidence of metastasis calculated at 1 dpi and 4 dpi for both cell lines. (**D**). Metastases were counted at 1 dpi and 4 dpi and normalized over the total number of live xenografts at each time point (**E**). Results are expressed as AVG \pm SEM for at least three independent experiments. Numbers of xenografts analyzed are the following: MDA-MB-231 1 dpi n=270, 4 dpi n=288; MCF10A 1 dpi n=294; 4 dpi n=39. Statistical analysis: one-way ANOVA followed by Tuckey's *post-hoc* test. ** p <0.01, *** p <0.001, **** p <0.0001.

In addition, to facilitate visual identification of MDA-MB-231 cells in the vessels of zebrafish xenografts, I took advantage of the transgenic reporter strain *Tg(kdrl:DsRed)*, expressing a red fluorescent vascular marker (Figure 7A-B). Immediately after transplantation, cells hematogenously disseminated. Confocal images of live xenografts at 1 dpi showed the presence of circulating tumor cells (CTCs) along the dorsal aorta (DA), the caudal vein (CV), the intersegmental vessels (ISVs) and the dorsal longitudinal anastomotic vessel (DLAV), mainly arresting in the CHT (Figure 7A', A''). As mentioned, CHT is the zebrafish vascular hematopoietic organ at larval stage. Although many CTCs regressed

without extravasating, I observed MDA-MB-231 BC cells extravasating from ISVs since 1 dpi (Figure 7A'). At 4 dpi, MDA-MB-231 cells extravasated mainly from the ventral side of CHT, forming peri-vascular secondary masses and, at the level of the posterior end of the *larva*, metastatic cells penetrated in the fibers of the tail fin (Figure 7B', indicated by arrow).

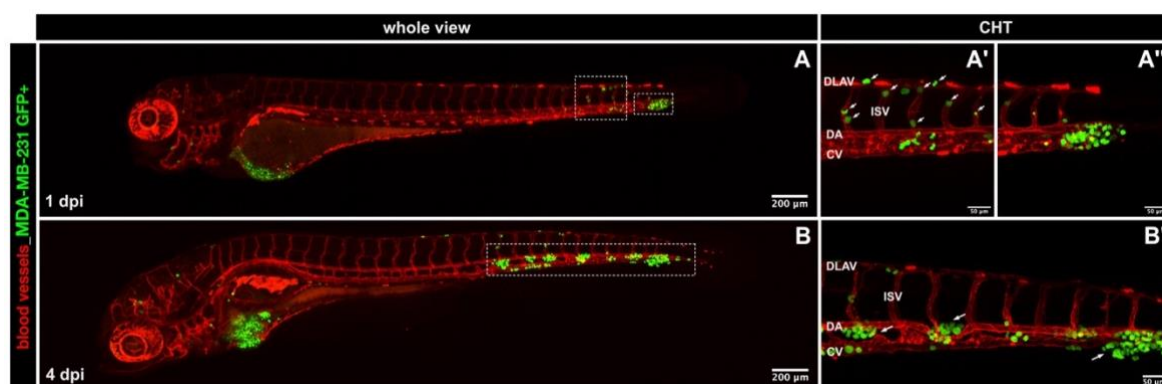
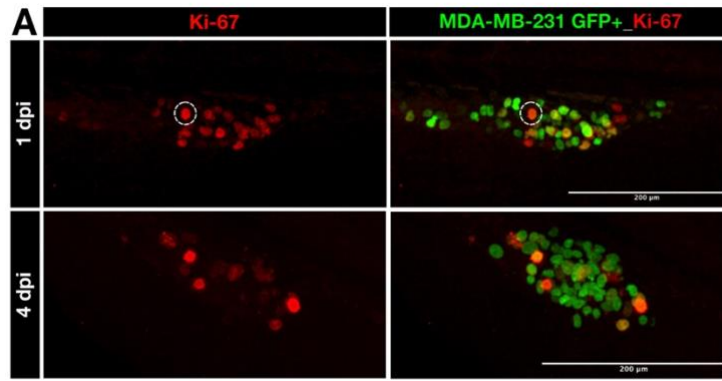


Figure 7 | Visual assessment of BC metastatic progression of MDA-MB-231 human BC cells in zebrafish xenografts. Representative z-stack confocal images of live *Tg(kdrl:DsRed)* fish representing the whole view of 1 dpi (A) and 4 dpi (B) MDA-MB-231 xenografts. Vessels are displayed in red and human BC cells in green. Dashed box: magnified areas. Scale bar= 200 µm. Magnification of CHT of 1 dpi (A', A'') and 4 dpi (B', B'') xenografts. Scale bar= 50 µm. CHT: caudal hematopoietic tissue; DLAV: dorsal longitudinal anastomotic vessel; ISV: intersegmental vessel; DA: dorsal aorta; CV: caudal vein.

Finally, I characterized metastases *ex vivo* in fixed animals by whole-mount immunofluorescence of Ki67 marker and quantification of mitotic figures (based on GFP fluorescence). I exclusively checked proliferation of larger metastases that have successfully seeded in the parenchyma of the secondary site, without undergoing massive apoptosis or immune clearance. At 1 dpi, I detected ~60% Ki67⁺ cells (60.3±3.3%), among which 4.3±1.2% mitotic figures, suggesting that metastatic expansion of MDA-MB-231 is the consequence of proliferation of extravasated cells at the metastatic site (Figure 8A upper panel-C). At 4 dpi, metastatic cells still presented a good rate of proliferation, although – similarly to what observed in PTs – the percentage of Ki67⁺ cells decreased to 35.3±1.9% ($p < 0.0001$), with 2.4±0.4% of mitotic figures (Figure 8A lower panel-C).



Metastasis proliferative index

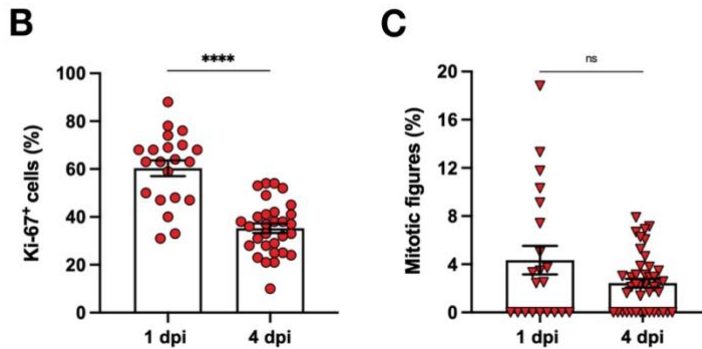


Figure 8 | MDA-MB-231 human BC extravasated cells proliferate at the metastatic site. Representative z-stack confocal images of whole-mount immunofluorescence staining for Ki67 on 1 dpi and 4 dpi metastases. Circles highlight mitotic figures. Green: BC cell nuclei; red: Ki67; scale bar= 200 μ m. All images are z-stacks maximum projections and were acquired at the same magnification (A). Quantification of % Ki67 was performed using Arivis Vision 4D 3.5.0 software. Results are expressed as AVG \pm SEM of at least three independent experiments. Each dot represents a xenograft. Numbers of xenografts analyzed are: 1 dpi, n=21; 4 dpi, n=30. Statistical analysis: *t* test (B). Mitotic figures were quantified slide by slide. Results are expressed as AVG \pm SEM of at least three independent experiments. Each dot represents a xenograft. Numbers of xenografts analyzed are: 1 dpi, n=21; 4 dpi, n=42. Statistical analysis: Mann-Whitney test (C). *****p*<0.0001; ns= not significant.

Immunofluorescence staining against the human MHC class I subunit (human HLA antibody) showed unequivocally the human origin of metastases and highlighted their architecture and localization. MDA-MB-231 cells, besides colonizing the peri-vascular parenchyma of the CHT (Figure 9A-A'), formed secondary masses in the caudal muscles (Figure 9B-B'') and penetrated the avascular collagenous fibers of the tail fin. Membrane staining revealed that MDA-MB-231 cells were able to invade this site by emitting filopodia-like protrusions at the invasive front (Figure 9C'-C'').

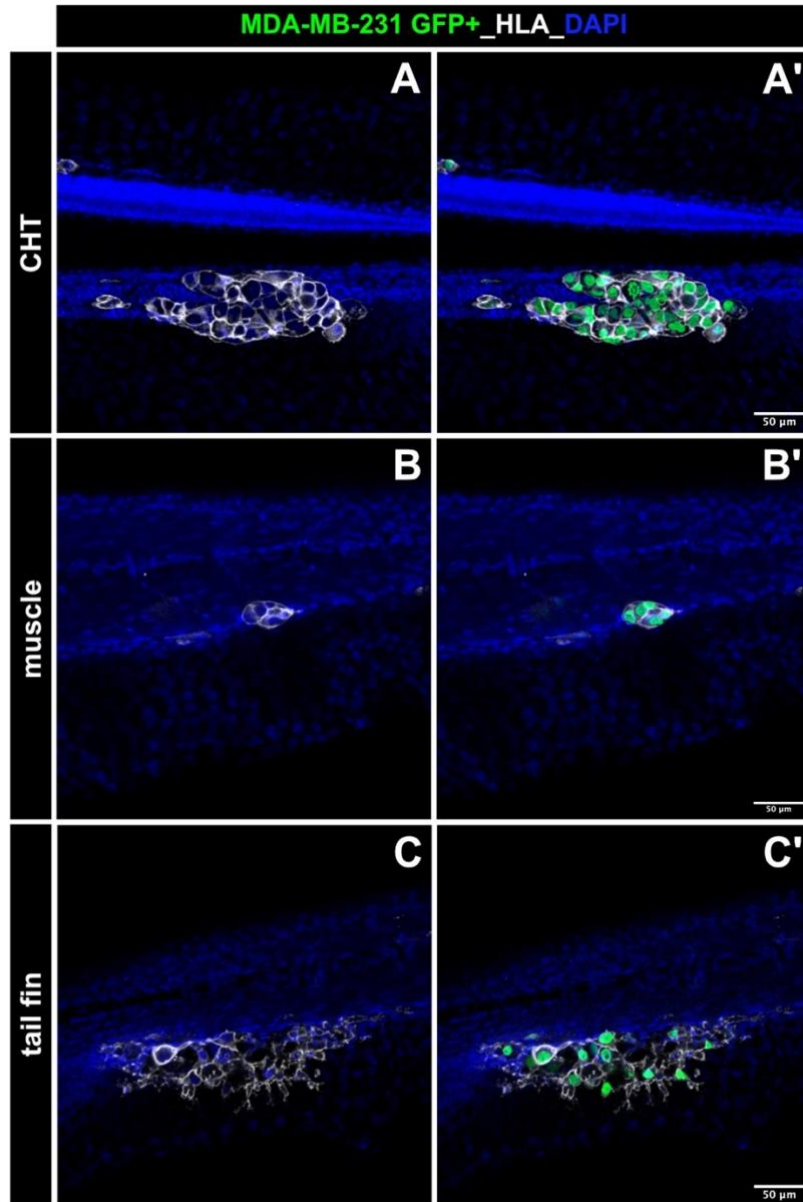


Figure 9 | MDA-MB-231 metastasis localization and architecture. Representative z-stack confocal images of whole-mount immunofluorescent staining for human HLA on 4 dpi xenografts show the presence of metastases in the CHT (**A-A'**), in the muscle (**B-B'**) and in the tail fin (**C-C'**) Green: human BC cell nuclei; white: human BC cell membranes; blue: DAPI; scale bar= 50 μ m. All images have the same magnification and represent a single plane.

4.2 Optimization of a set of quantitative parameters to analyze the different steps of BC metastatic progression

4.2.1 Experimental design

Once established a robust zebrafish xenograft-platform to model human BC progression, I exploited its peculiar characteristics to define a set of tools for the quantitative analysis of the metastatic cascade of human breast tumors.

As mentioned in paragraph 2.3.3, the injection site in the zebrafish *larva* determines which specific metastatic stage can be most properly investigated. Therefore, I designed and compared two distinct experimental procedures – local and intravenous injections – in order to discriminate respectively, early (invasion and intravasation) and late (extravasation and colonization) phases of BC metastatic progression. Taking advantage of *Tg(kdrl:DsRed)* fish, I separately injected ~500 MDA-MB-231 cells/*larva* either in the blood stream, performing cell transplantation in the DoC, or subcutaneously, performing transplantation in the PVS. Immediately after PVS injection, animals are observed at the stereomicroscope to eliminate all the fish that presented tumor cell leakage in the vessels. Live xenografts are then analyzed at 1 and 4 dpi, while kept separated from each other in 48-multi-well plates. Experimental design and timeline are reported in Figure 10.

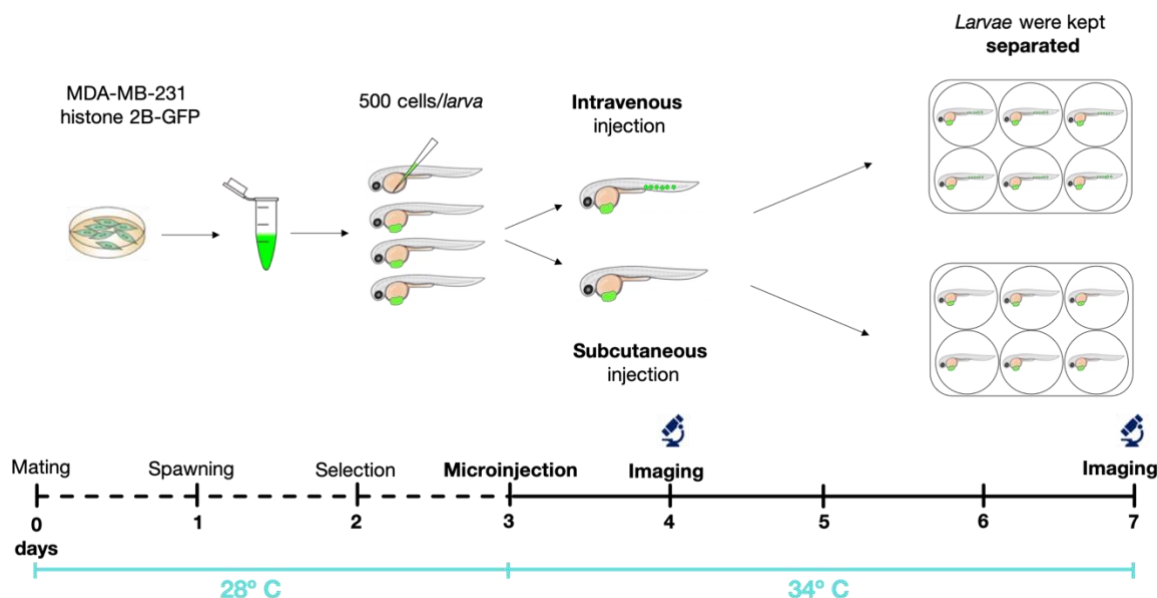


Figure 10 | Optimization of two distinct assays to evaluate metastasis formation. Experimental design and timeline.

4.2.2 Incidence of metastasis

Incidence of metastasis quantifies the number of xenografts that present at least one extravasated metastatic cell cluster (≥ 5 cells) at a secondary site and represents a measure of the overall efficiency of metastasis formation. In general, metastasis efficiency may vary depending on the capacity of cancer cells to detach from the PT, enter the circulation, survive in the bloodstream, extravasate and seed at distant sites. To successfully establish a metastasis, MDA-MB-231 cells transplanted subcutaneously have to go through all the steps of the metastatic cascade, whereas MDA-MB-231 cells injected intravenously only have to undergo the later stages. Observation of live xenografts revealed that $21.8 \pm 1.3\%$ of subcutaneously injected fish developed extravascular metastases already at 1 dpi and this percentage significantly increased till almost 70% at 4 dpi ($p < 0.0001$), confirming the highly metastatic nature of this BC cell line.

When cancer cells are directly placed in the circulation, the early metastatic steps are by-passed, thus increasing the likelihood of successful colonization. This is supported by the higher incidence of metastasis calculated for intravenously injected fish at 1 dpi ($51 \pm 1.8\%$; $p = 0.0053$). However, I did not observe a significant difference in the incidence of metastasis between the two groups at 4 dpi ($69 \pm 8.8\%$ vs. $86 \pm 3.5\%$; $p = 0.1148$) suggesting that, in the absence of continuous feeding from the PT, the short half-life of CTCs limits the efficiency of metastatization (Figure 11A).

Based on these considerations, I split the incidence-of-metastasis determination into two indexes: Early Metastatic Potential (EMP) and Late Metastatic Potential (LMP). Interestingly, I scored no significant differences among EMP and LMP for MDA-MB-231 cells at both 1 dpi ($42.8 \pm 1.5\%$ vs. $51 \pm 1.8\%$; $p = 0.8026$) and 4 dpi ($81 \pm 12.2\%$ vs. $86 \pm 3.5\%$; $p = 0.9452$), suggesting that intravasation involves all cells of the PT with a potential to survive in the bloodstream (Figure 11B).

Overall, these parameters allows to evaluate the metastatic potential of a tumor by comparing the efficiency of cells in metastasizing when placed in the circulation or not, based on their capacity to support the entire metastatic cascade.

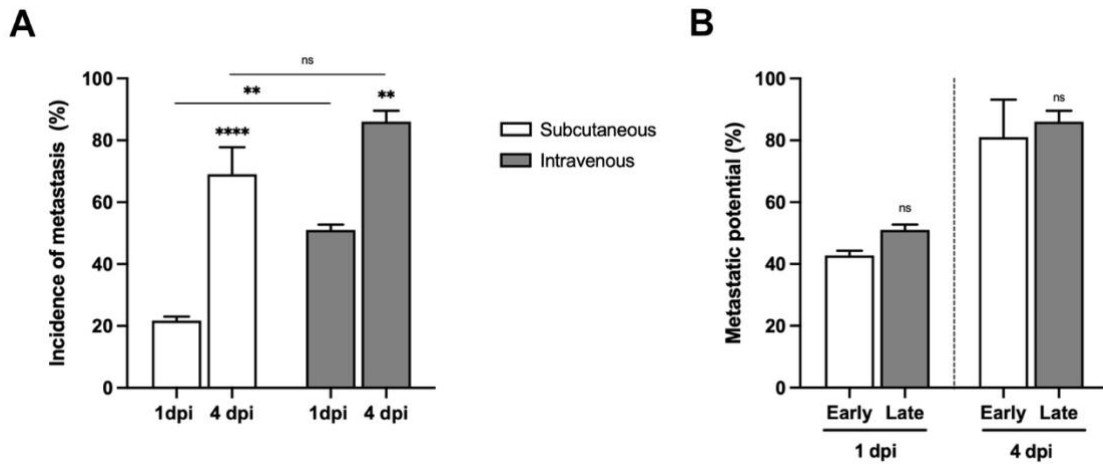


Figure 11 | Incidence of metastasis formation in zebrafish xenografts for MDA-MB-231 human BC cells. Quantification of the incidence of metastasis for MDA-MB-231 cells at 1 dpi and 4 dpi, with two modalities of injection, subcutaneous and intravenous. Results are expressed as $AVG \pm SEM$ of at least three independent experiments. Numbers of xenografts analyzed are: subcutaneous injection 1 dpi=140, 4 dpi=73; intravenous injection 1 dpi=359, 4dpi=268 (A). Measurement of Early (EMP) and Late (LMP) Metastatic Potential for MDA-MB-231 cells at 1 dpi and 4 dpi. Results are expressed as $AVG \pm SEM$ of at least three independent experiments (B). Statistical analysis: one-way ANOVA followed by Tuckey's *post-hoc* test. ** $p < 0.001$, **** $p < 0.0001$, ns= not significant.

4.2.3 Numbers of metastases

I then evaluated successful metastatic seeding at distant sites quantifying the average number of extravasated metastatic growths in MDA-MB-231 zebrafish xenografts, injected either subcutaneously or intravenously. Exploiting these two distinct modalities of injection, it is possible to measure at which extent transplanted cancer cells seed in a secondary organ depending on their capacity to undergo the entire metastatic cascade or only the later phases. To capture the process of metastatic seeding I counted not only the macroscopic lesions (>10 cells), but also micro-metastatic clusters composed by at least 5 extravasated cancer cells, that constitute potential foci of metastatic outgrowth. The use of reporter fish with fluorescent vasculature *Tg(kdrl:DsRed)* enabled to unequivocally identify extravasated cells.

Stereomicroscope observation of anesthetized live xenografts showed that the average number of metastases scored in subcutaneously transplanted animals is significantly lower with respect to the intravenously transplanted fish, at both 1 dpi (0.34 ± 0.04 vs. 1.12 ± 0.12 ; $p = 0.0085$) and 4 dpi (1.23 ± 0.15 vs. 2.68 ± 0.22 ; $p < 0.0001$). Interestingly, metastases count increased over time nearly three times as much in both conditions, passing from 0.36 ± 0.05 to 1.23 ± 0.15 for PVS injection ($p = 0.0033$) and from 1.12 ± 0.12 to 2.68 ± 0.22 ($p < 0.0001$) for DoC injection (Figure 12A).

Since animals were kept separated from one another along all the experimental time-window and independently imaged, I calculated metastasis increment over time as the difference in the total number of metastases per each xenograft between 4 and 1 dpi. The analysis revealed that, as shown in the box plot (Figure 12B), once extravasated, the increment metastasis number is similar in both subcutaneously and intravenously injected xenografts ($p=0.5573$).

These results confirm that MDA-MB-231 cells are able to successfully complete all the metastatic steps in four days. In addition, the comparable metastasis increment measured for subcutaneously and intravenously transplanted xenografts suggests comparable dynamics of metastatic colonization between the two groups. However, the much-higher numbers of metastatic lesions observed when cells are directly placed in the circulation demonstrates that the extent of metastatic seeding is dependent on the injection site.

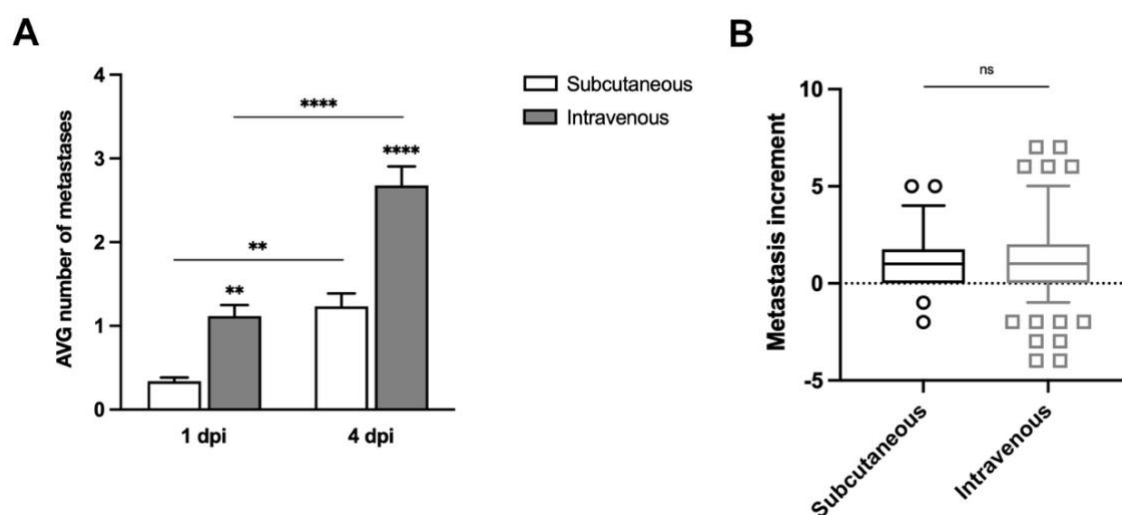


Figure 12 | Average number of metastasis detected in zebrafish xenografts transplanted with MDA-MB-231 human BC cells. Quantification of the AVG number of metastases for MDA-MB-231 cells at 1 dpi and 4 dpi, with two modalities of injection: subcutaneous and intravenous. Xenografts that did not develop any metastasis were included in the count. Results are expressed as $AVG \pm SEM$ of at least three independent experiments. Numbers of xenografts analyzed are: subcutaneous injection 1 dpi=182, 4 dpi=91; intravenous injection 1 dpi=454, 4dpi=317. Statistical analysis: one-way ANOVA followed by Tuckey's *post-hoc* test (A). Metastasis increment is measured as Δ metastases between 4 dpi and 1 dpi. Results are expressed as median \pm 95%CI of at least three independent experiments. Numbers of xenografts analyzed are: subcutaneous injection=84; intravenous injection=206. Statistical analysis: Mann-Whitney test. ** $p < 0.001$, **** $p < 0.0001$, ns=not significant.

4.2.4 Metastasis size

Successful metastatic colonization is achieved when extravasated micro-metastatic clusters survive the microenvironment of the secondary site, respond to survival and

proliferative stimuli and expand to form macro-metastatic lesions. With the purpose of following these phases, I analyzed the distribution of metastases according to their size. The small dimensions and optical transparency of zebrafish *larvae*, combined with the usage of the nuclear fluorescent reporter H2B-GFP, enabled to reach extraordinary cellular resolution for live imaging. Thus, metastasis size was simply assessed counting numbers of the GFP⁺ nuclei composing each extravasated metastatic lesion in anesthetized living xenografts at 1 and 4 dpi. On the basis of cellularity, I categorized metastases in three separate groups: *i*) micro-metastases, composed by a number of cells between 5 and 10; *ii*) mid-size metastases, composed by a number of cells between 10 and 20; *iii*) overt metastases, composed by >20 cells. Each category depicts a distinct step of metastasis formation, namely seeding for micro-metastases, active colonization for mid-size metastases and outgrowth for overt metastases.

Results showed no significant differences in how metastases are distributed according to their size between subcutaneously and intravenously transplanted xenografts at both 1 and 4 dpi, confirming that the dynamics of metastatic colonization do not depend on the injection site. Metastases homogeneously distributed within the single groups, with each size category accounting for approximately one third of the total number of metastases at the end of the assay (Figure 13). These findings suggest that, although a part of micro-metastases may not survive the foreign microenvironment, newly formed metastatic foci continue to appear over time as a consequence of active metastatic cell seeding, while others expand in size.

Despite the differences are statistically not-significant, cells injected in the PVS mostly gave origin to micro- ($44.2 \pm 0.08\%$ at 1 dpi; $43.2 \pm 0.05\%$ at 4 dpi) and mid-size metastatic lesions ($40.3 \pm 0.05\%$ at 1 dpi; $34.2 \pm 0.02\%$ at 4 dpi), whereas larger masses represented only $15.5 \pm 0.07\%$ of total metastases at the first time point and $22.6 \pm 0.05\%$ of total metastases at the end of the assay. According to these findings, the onset of overt metastases that have efficiently undergone colonization and outgrowth is slightly delayed upon subcutaneous injection of MDA-MB-231 cells, a likely consequence of their necessity to go through the entire metastatic cascade during the 4-day observation.

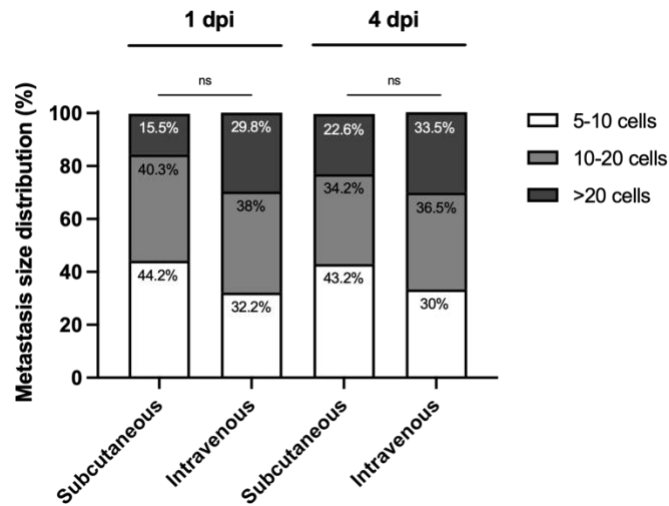


Figure 13 | Distribution of MDA-MB-231 metastases according to their size. Comparison of MDA-MB-231 metastasis size distributions between subcutaneous and intravenous injected xenografts at the same time point. Results are expressed as AVG of at least three independent experiments. Statistical analysis= Chi-square test. Results are expressed as AVG of at least three independent experiments. Numbers of metastatic masses analyzed are: subcutaneous injection 1 dpi=66, 4 dpi=117; intravenous injection 1 dpi=381, 4dpi=315. ns= not significant.

4.2.5 Metastatic burden

The metastatic-burden index assigns a score to each xenograft based on both numerosity and size of metastases, thereby expressing the overall grade of metastatic progression for each animal. Each size category is defined by a score that differently contributes to the definition of the metastatic burden: 0.5 for micro-metastasis; 0.75 for mid-size metastasis; 1.5 for overt metastasis. Size scores were arbitrary chosen on the basis of the relevance that each category may have in a hypothetical clinical context, with overt metastasis having the heaviest impact on clinical outcome. Therefore, metastatic burden quantitatively manifests the severity of metastasis colonization, resembling a clinical parameter. Metastatic burden was computed according to the equation described in paragraph 3.3.4 of *Materials and Methods*.

This index revealed that subcutaneously transplanted MDA-MB-231 cells have a significantly reduced metastatic burden as compared to the same cells directly placed in the circulation, at both 1 dpi (1.02 ± 0.006 vs. 1.42 ± 0.05 ; $p < 0.0001$) and 4 dpi (1.23 ± 0.04 vs. 2.26 ± 0.13 ; $p < 0.0001$). Metastatic burden of fish transplanted with both modalities of injection increased over time, demonstrating a progressive worsening of the “clinical” conditions of zebrafish recipients with regard to their metastatic disease (Figure 14A).

I then calculated how the metastatic-burden index of each animal varies between 1 and 4 dpi, as fold change (Figure 14B). Although the value was slightly higher for the

intravenously injected cells, I observed a comparable level of variation in both conditions (1.17 ± 0.04 vs. 1.59 ± 0.09 ; $p=0.0917$).

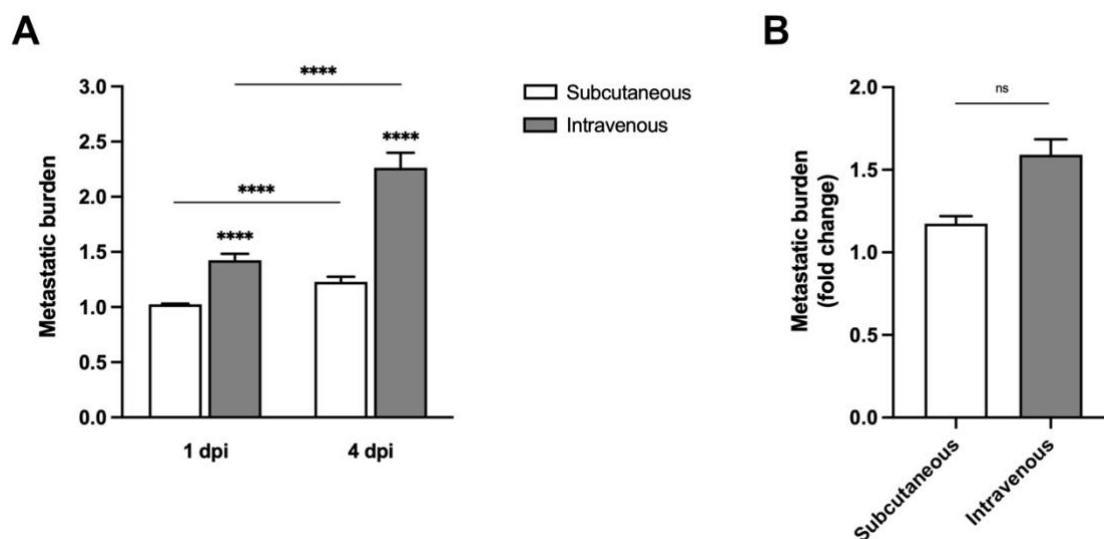


Figure 14 | Human BC MDA-MB-231 metastatic burden in zebrafish xenografts. Quantification of the metastatic burden for MDA-MB-231 cells at 1 dpi and 4 dpi, transplanted with two modalities of injection, subcutaneous and intravenous. Results are expressed as $AVG\pm SEM$ of at least three independent experiments. Statistical analysis: Kruskal-Wallis test. **(A)**. Measurement of metastatic burden fold change between 1 dpi and 4 dpi, for each zebrafish xenograft injected either subcutaneously or intravenously. Results are expressed as $AVG\pm SEM$ of at least three independent experiments. Statistical analysis: Mann-Whitney test **(B)**. Numbers of xenografts analyzed are: subcutaneous injection 1 dpi=183, 4 dpi=85; intravenous injection 1 dpi=238, 4dpi=146 .**** $p<0.0001$, ns= not significant.

4.2.6 Frequency of metastasis initiating cells

According to literature data and clinical evidence, the rate of metastasis initiation correlates with the size of the PT [Klein *et al.*, 2009]. As cancer advances, in fact, cells located at the surface of the PT and close to blood vessels spread to other parts of the body, where they extravasate and form metastatic lesions.

Assuming that all cells composing the PT are viable and able to metastasize at the same rate and assuming that metastatic lesions originate from a single extravasated cell, I quantified the frequency of metastasis initiating cells (MIC) normalizing the number of metastases at 4 dpi over the total number of cells that constitute the PT mass in subcutaneously transplanted xenografts. From this analysis I observed that $0.45\pm 0.1\%$ of MDA-MB-231 cells are able to initiate metastatic growth starting from the PT.

Applying the same calculation to intravenously transplanted xenografts, the percentage of MIC, which amounts to $1.15\pm 0.26\%$, reflects the extravasation/seeding probability of MDA-MB-231 cancer cells in the zebrafish host (Figure 15). The frequencies

calculated for the two modalities of injection differed from one another ($p=0.0446$), demonstrating that only a smaller subset of cells within the PT has the capacity to undergo the entire metastatic cascade, as compared to cells that skipped the counter selection of the intravasation step.

Although built on basic assumptions, this index gives a preliminary hint of how many cells in a specific PT are endowed with pro-metastatic properties.

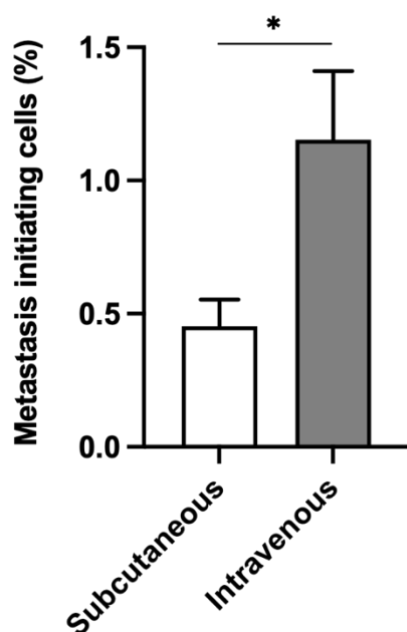


Figure 15 | Frequency of metastasis initiating cells in zebrafish xenografts for human BC MDA-MB-231 cell line. Percentage of MIC was measured normalizing the AVG number of metastases at 4 dpi over the total number of cells composing the PT, for both subcutaneously and intravenously injected xenografts. PT cellularity was quantified on confocal images of fixed 4 dpi xenografts, using Arivis Vision 4D 3.5.0 software. Results are expressed as $AVG \pm SEM$ of at least three independent experiment. Numbers of xenografts analyzed are the following: subcutaneous, $n=26$; intravenous, $n=26$. Statistical analysis: t test. $*p < 0.05$.

4.2.7 Metastasis proliferative index

As already described in previous paragraphs, the proliferative index of metastases can be easily quantified in zebrafish xenografts via *ex vivo* imaging applications. At the end of the assay, I sacrificed 4 dpi MDA-MB-231 xenografts regardless the injection site and fixed them in PFA to performed whole-mount immunofluorescence analyses of Ki67 expression. I evaluated proliferative potential according to metastasis size, aiming to investigate whether cells in differently-sized metastases are actively proliferating or exist in a dormant state.

Analyses showed that proliferative indexes were comparable in the mid-size and overt metastases ($\sim 27\%$ Ki67-positivity; $p=0.9122$), while significantly lower in the micro-metastases ($\sim 16\%$ of Ki67-positivity; $p=0.0413$). These data support the hypothesis that cells of micro-metastases are initially quiescent, until the resolution of stress responses or the occurrence of specific environmental signals trigger their expansion.

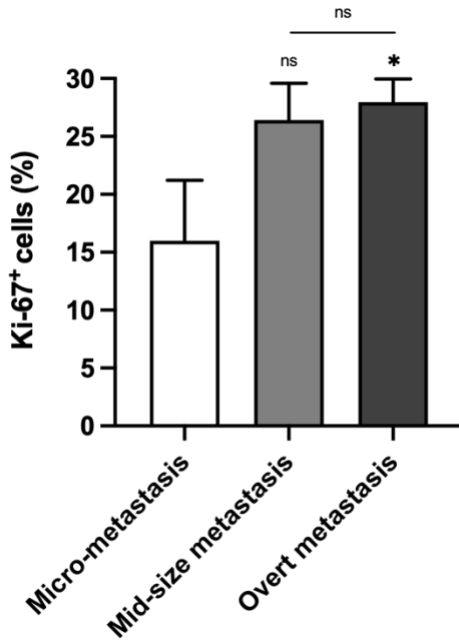


Figure 16 | Frequency of proliferating MDA-MB-231 cells at the metastatic site in zebrafish xenografts. Percentage Ki67⁺ cells was measured on confocal images of fixed 4 dpi xenografts, using Arivis Vision 4D 3.5.0 software. Metastases were discriminated basing on their size. Results are expressed as AVG±SEM of at least three independent experiment. Numbers of analyzed xenografts are the following: micro-metastases, n=9; mid-size metastases, n=18; overt metastases n=33. Statistical analysis: one-way ANOVA followed by Tuckey's *post-hoc*. test. **p*<0.05.

4.2.8 Metastasis outgrowth

Since I observed active proliferation at the metastatic site in zebrafish *larvae*, I analyzed whether metastases cellularity increase significantly over time (metastasis outgrowth), by measuring the increment in metastasis cell numbers between 1 and 4 dpi. Also in this case the analysis was performed *ex vivo*, sacrificing a pool of animals for whole-mount immunofluorescence.

Notably, larger metastases (>20 cells/metastasis) expanded in size between 1 and 4 dpi, probably as a consequence of cell division (Figure 17), passing from an AVG of 27 cells at 1 dpi to 50 cells at 4 dpi (*p*<0.0001).

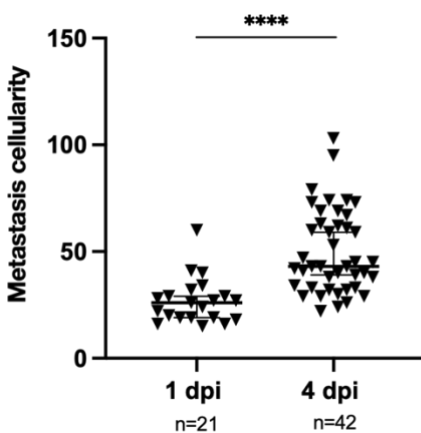


Figure 17 | Human BC MDA-MB-231 metastatic outgrowth in zebrafish xenografts. Metastasis cellularity was measured on confocal images of fixed MDA-MB-231 xenografts at 1 dpi and 4 dpi, using Arivis Vision 4D 3.5.0 software. Results are expressed as AVG±SEM. Each symbol in the dot plot represents a xenograft. Numbers of xenografts analyzed are: 1 dpi n=21; 4 dpi n=43. Statistical analysis: Mann Whitney test. *****p*<0.0001.

4.2.9 Summary

As illustrated in the previous paragraphs, the zebrafish larval xenograft assay enables calculation of a series of semi-quantitative scores for several analytical parameters, aiming to describe metastasis progression of human breast tumors. A comprehensive summary of all the scores for MDA-MB-231, and their biological significance, is reported in Table 1. Early and late phases of the metastatic cascade are discriminated exploiting two distinct protocols of cell injection: subcutaneous and intravenous, reported in the table as S.I. and I.I. respectively.

Simultaneously, as described in paragraphs 1.2 and 1.3 of chapter 4, my zebrafish xenograft-platform also allows to measure PT engraftment (as the percentage of xenografts that develop a tumor mass at the size of injection), PT size (expressed both as volume and cellularity) and proliferative index of PT cells (expressed as the frequency of Ki67⁺ cells).

Table 1 | Summary table of quantitative parameters describing human BC metastatic progression in zebrafish xenografts

| Quantitative parameters of metastasis progression | | Biological informations | 1 dpi | | 4 dpi | | |
|---|-----------------------|---|-------------------|-------------------|-------------------|----------------------|------------------------------|
| | S.I. vs I.I. | | S.I. | I.I. | S.I. | I.I. | p value |
| Incidence of metastasis (%) | S.I. vs I.I. | Percentage of xenografts that develop at least one distant metastasis | 21.8±1.3 | 51±1.8 | 69±8.7 | 86±3.5 | 0.1148 |
| Metastatic potential (%) | Early vs Late | Rate of distant metastasis formation based on the capacity of the cells to entirely of partially undergo the metastatic cascade | Early 42.8±1.6 | Late 51±1.8 | Early 81±12.2 | Late 86±3.5 | 0.9452 |
| Number of metastasis | S.I. vs I.I. | Average number of extravasated metastases at distant sites | S.I. 0.34±0.04 | I.I. 1.12±0.13 | S.I. 1.23±0.16 | I.I. 2.68±0.22 | <0.0001 |
| Metastasis increment | 1 dpi vs 4 dpi | Metastasis number variation over time | | | S.I. 1.02±0.15 | I.I. 1.19±0.14 | 0.5573 |
| Frequency of metastasis initiating cells (%) | S.I. vs I.I. 4 dpi | Percentage of cells able to initiate metastasis formation | | | S.I. 0.45±0.1 | I.I. 1.15±0.26 | 0.0446 |
| Metastasis size distribution (%) | S.I. vs I.I. | Distant metastases distribution in micro-, mid-size and overt metastases | S.I. 45-40-15 | I.I. 32-38-30 | S.I. 43-34-23 | I.I. 30-37-33 | 0.0523 |
| Metastatic burden | S.I. vs I.I. | Severity of metastasis progression | S.I. 1.02±0.01 | I.I. 1.42±0.06 | S.I. 1.23±0.05 | I.I. 2.26±0.14 | <0.0001 |
| Metastasis proliferative index | 4 dpi | Percentage of active proliferating cells at the metastatic site | | | Micro 15.9±5.2 | Mid-size 26.4±3.2 | Overt 27.9±2.0 |
| Metastasis outgrowth | 1 dpi vs 4 dpi | Size increment of overt metastasis | | 26.7±2.3 | | 49.8±3.0 | p value <0.0001 |

4.3 Zebrafish xenografts as *in vivo* platform to quantitatively test the pro-metastatic role of candidate genes in BC: a focus on ANGPTL4

The zebrafish xenograft metastasis platform described in the previous paragraphs enables semi-quantitative analyses of the metastatic cascade of human BC. The platform is robust, significantly faster than its murine counterpart (4 days vs. several months) and relatively low-cost, thereby providing the possibility to easily scale up experiments to a large number of animals. Thus, I tested the zebrafish larval assay as high-throughput approach to unravel the function of candidate genes in metastasis progression.

Our laboratory has recently set up a robust *in vivo* lineage tracing approach for the identification of genes involved in the establishment of the pro-metastatic transcriptional phenotype of growing breast PTs, using MDA-MB-231 cells as model system. BC cells were *in vitro* engineered with a library of expressed barcodes, orthotopically transplanted in immune-deficient mice and monitored during metastatization by single-cell RNA sequencing, to follow their clonal evolution [Adamson *et al.*, 2016; Dixit *et al.*, 2016]. By this approach, we were able to simultaneously reconstruct both the clonal architecture and dynamics of PTs and metastases and characterize their transcriptional profiles with single-cell resolution. Analysis of clonal dynamics showed that MDA-MB-231 cells generate highly monoclonal metastases from rare pro-metastatic clones in the growing PT. scRNAseq revealed that the pro-metastatic clones mainly activate pathways involved in migration, ECM deposition and activation of stress responses (*i.e.* hypoxia, UPR and type-I IFN response). Strikingly, genes up-regulated in the pro-metastatic clones predict worse prognosis in BC patients. The top-ranked differentially expressed genes include ANGPTL4, KCNQ1OT1, ITGB4, LY6E, IFI6 and FST (manuscript in preparation). To validate these genes and to investigate their function(s) in the metastatic cascade, I examined their behavior *in vivo* by sh-mediated gene knock-down (KD) and XT in the zebrafish model.

I first analyzed in zebrafish angiopoietin-like 4 (ANGPTL4), the only gene in the list already known to play a role in BC metastasis in mice. ANGPTL4 is a cytokine specifically expressed by mammary tumor cells upon activation by TGF β . The pro-metastatic role of ANGPTL4 is exerted at later phases of the metastatic cascade, specifically in the extravasation step, since its stimulates the dissociation of endothelial cell-to-cell junctions in lung capillaries, enabling extravasation of ANGPTL4-secreting BC cells [Padua *et al.*, 2008].

MDA-MB-231-GFP⁺ cells were engineered to express either two independent ANGPTL4-specific shRNAs or a scrambled shRNA construct as a control, and transplanted either subcutaneously or intravenously in zebrafish *larvae* (~500 cells/*larva*; ~100 *larvae*/condition). Fish were monitored for PT and metastasis progression at 1 and 4 dpi, keeping the animals separated from one another along all the experimental time-window. Results were expressed according to the quantitative analytical tools presented in Table 1 of paragraph 4.2.9.

4.3.1 ANGPTL4 is not involved in PT implantation and growth

To investigate whether ANGPTL4 plays a role in cancer cell growth, aside from its involvement in metastatization, I first assessed the impact of ANGPTL4 silencing on the capacity of MDA-MB-231 BC cells to engraft and develop a PT mass.

MDA-MB-231 control cells displayed a high implantation potential, with ~93% xenografts harboring a consistent PT mass at the site of injection at 4 dpi (Figure 18A', B), with a volume comparable to what described for MDA-MB-231 cells in paragraph 4.1.2. ANGPTL4 KD cells grafted at a similarly high rate (Figure 18A'', A''', B; sh#1 $p=0.2187$; sh#2 $p=0.6672$) and gave rise to PTs with comparable size (Figure 18C; sh#1 $p=0.9997$; sh#2 $p=0.5610$) and cellularity (Figure 18D; sh#1 $p=0.9995$; sh#2 $p>0.9999$). Notably, xenotransplantation experiments in immunocompromised mice performed in our laboratory using the same cells demonstrated that *in vivo* PT growth is not impaired by the lack of ANGPTL4 also in the mammalian host (Figure 18E, data courtesy of Niccolò Roda). Consistently, I observed similar frequencies of Ki67⁺ cells (~25%) at 4 dpi in ANGPTL4 KD and control cells (Figure 18F; sh#1 $p=0.9997$, sh#2 $p=0.5610$).

Therefore, ANGPTL4 does not confer any advantage to BC cells in terms of animal engraftment and PT *in vivo* growth.

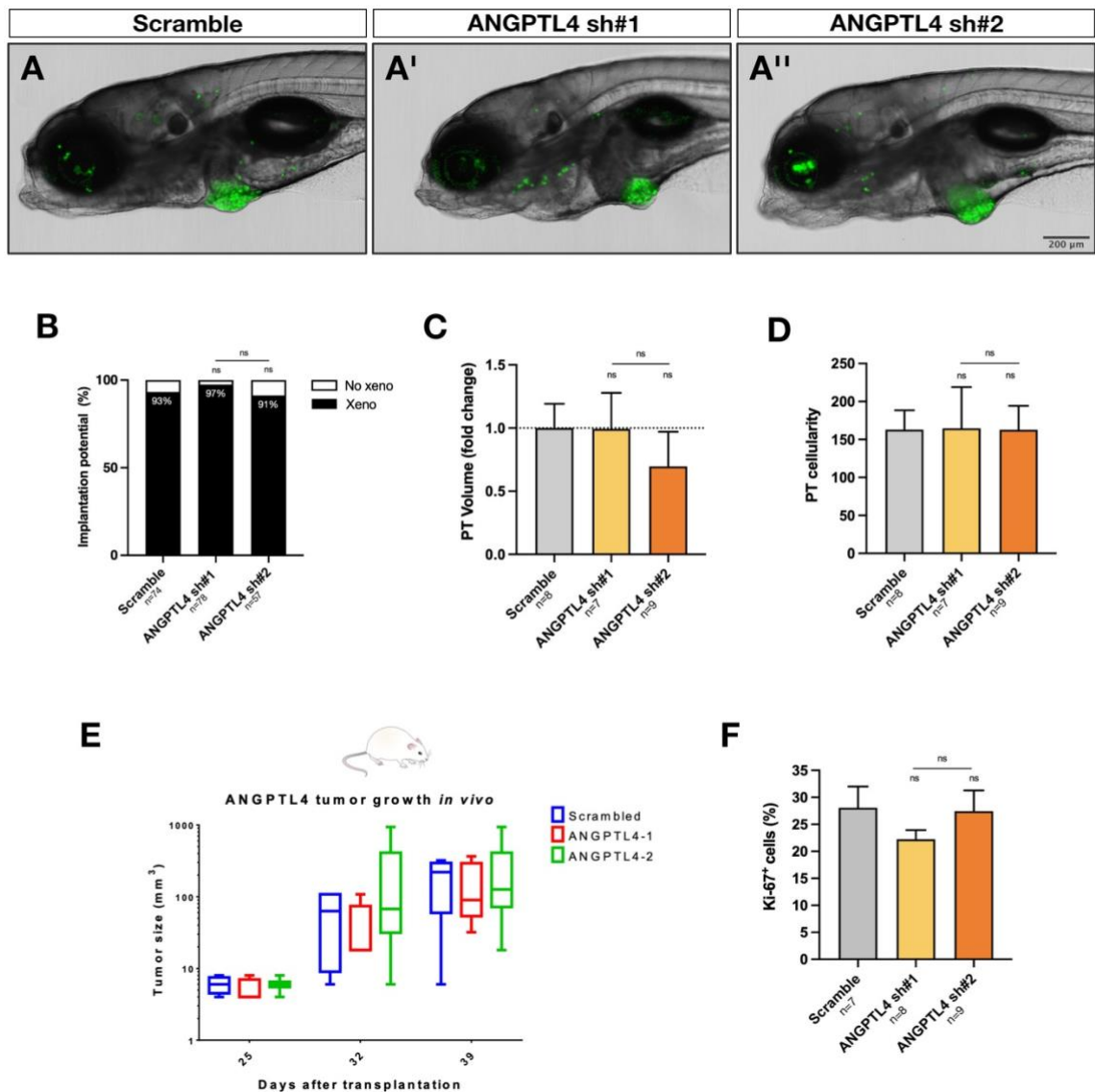


Figure 18 | Analysis of PT engraftment and growth in zebrafish xenografts upon ANGPTL4 silencing. Z-stack confocal images of live 4 dpi xenografts transplanted with scramble (A'), ANGPTL4_sh#1 (A'') and ANGPTL4_sh#2 (A''') cells, representing PTs grafted at the site of injection. Green: human BC cell nuclei. Scale bar= 200 μ m. Implantation potential was measured at 4 dpi. Statistical analysis: z score test (B). Quantification of the PT volume was performed *ex vivo* at 4 dpi using a Fiji/ImageJ customized pipeline (C). PT cellularity (D) and proliferative index (F) was measured *ex vivo* at 4 dpi using Arivis Vision 4D 3.5.0 software. PT growth in the mouse model. Data on mouse xenografts were a courtesy of Niccolò Roda (E). Number of analyzed xenografts for all zebrafish experiments are reported in the graphs. Statistical analysis: one way ANOVA followed by Tuckey's *post-hoc* test. ns= not significant.

4.3.2 ANGPTL4 is essential in the step of extravasation of metastatic cells

I then investigated incidence of metastasis following subcutaneous or intravenous injection of ANGPTL4-silenced cells. This index measures efficiency of extravasation, by comparing metastatic potential of cells undergoing the entire or only the last phases of the metastatic cascade.

Despite a little decrease in the incidence of metastases at 1 dpi (sh#1, $p=0.00596$; Figure 19A), I observed no differences between control and ANGPTL4 KD cells in the number of xenografts that develop metastases at 4 dpi for subcutaneous injection (41% average incidence of metastasis in control and shRNA-specific cohorts; Figure 19B). On the contrary, the percentage of xenografts with metastases dramatically dropped in *larvae* injected-intravenously with control *vs.* ANGPTL4-silenced cells at both 1 dpi (Figure 19C) and 4 dpi (Figure 19D), with 93% *vs.* 35% (sh#1, $p<0.0001$) or 58% (sh#2, $p=0.00034$) xenografts presenting at least one metastasis at the end of the assay. Since the specific role of ANGPTL4 in extravasation has been previously demonstrated in mice [Padua *et al.*, 2008], these results validate the capacity of my zebrafish xenograft metastasis-assay to discriminate early and late phases of BC metastatic cascade.

Evaluation of Early (EMP) and Late (LMP) Metastatic Potential indexes at 4 dpi confirmed the previous findings. Upon silencing of ANGPTL4, average LMP between the two shRNAs was equal to 46%, whereas EMP was twice as high, amounting to 90%.

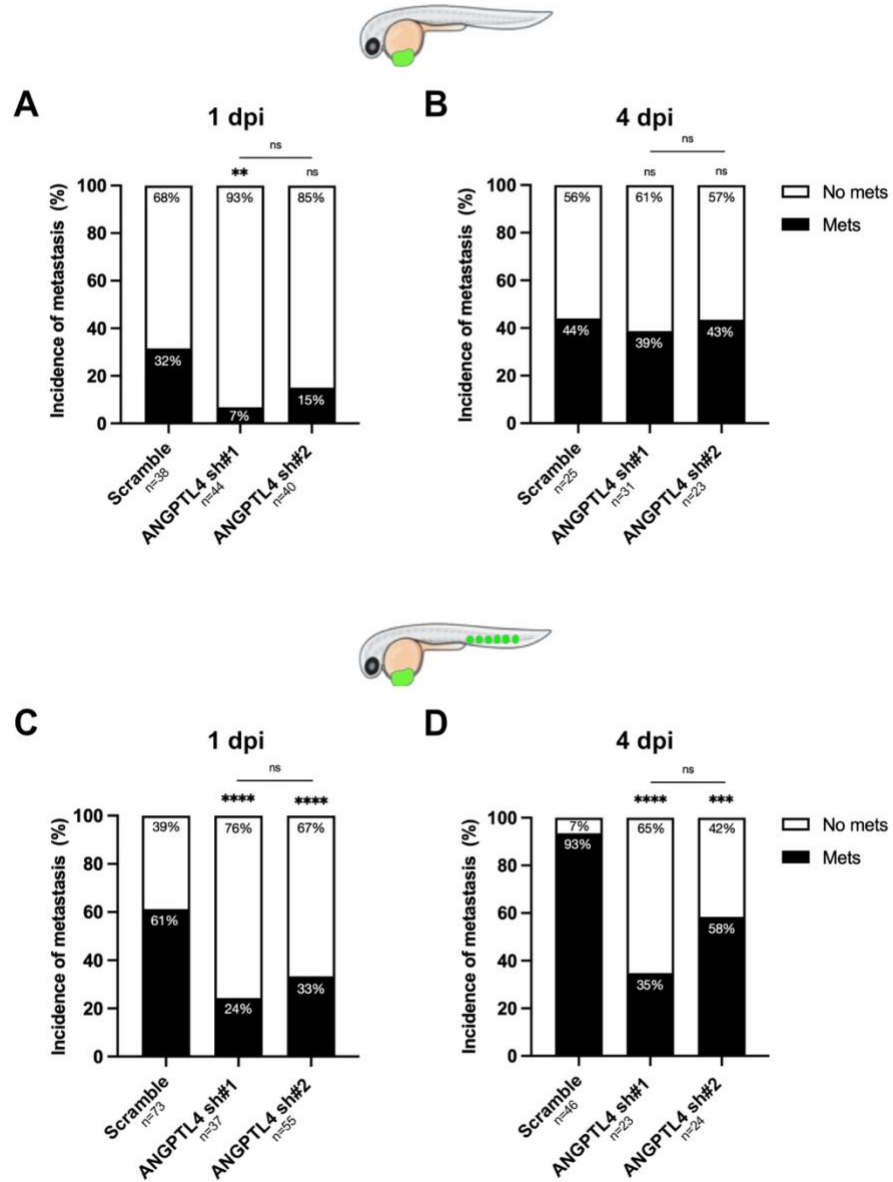


Figure 19 | Incidence of metastasis formation in zebrafish xenografts for MDA-MB-231 cells upon ANGPTL4 silencing. Quantification of the incidence of metastasis for subcutaneous injection at 1 dpi (**A**) and 4 dpi (**B**) and for intravenous injection at 1 dpi (**C**) and 4 dpi (**D**). Number of analyzed xenografts are reported in the graphs. Statistical analysis: *z* score test. ** $p < 0.01$, *** $p < 0.001$, **** $p < 0.0001$, ns= not significant.

4.3.2 ANGPTL4 silencing reduces the number of extravasated metastases but does not impact on their size

Once demonstrated that the lack of ANGPTL4 reduces the efficiency of metastasis formation when cells are placed in the circulation, I evaluated the extent of metastatic seeding, quantifying numbers and size of metastases at 1 and 4 dpi.

Following subcutaneous injection, despite a slight decrement at 1 dpi observed only with the sh#1 ($p=0.0060$), the AVG number of extravasated metastatic growths in zebrafish xenografts was not affected by ANGPTL4 silencing at 4 dpi ($p>0.9999$; Figure 20A). In opposition, intravenous injection of ANGPTL4-interfered cells, showed significantly fewer metastases, as compared to control cells at both 1 dpi (sh#1, $p=0.0006$; sh#2, $p=0.0065$) and 4 dpi (sh#1, $p<0.0001$; sh#2, $p=0.0064$; Figure 20B). Being animals separated from one another, the assay allowed to count metastases in the same fish at both 1 and 4 dpi, aiming to monitor metastasis evolution longitudinally. This analysis revealed a median increase of 2 metastases/fish between 1 and 4 dpi in scramble-injected xenografts, whereas numbers of metastases in ANGPTL4 KD-injected fish did not undergo significant variations (sh#1, $p=0.0002$; sh#2, $p=0.0172$; Figure 20C). The metastatic potential of ANGPTL4-interfered cells was tested in parallel also in immunocompromised mice, obtaining similar results. In mice, metastatic outbreak in secondary organs was assessed *post-mortem*, checking the presence of metastatic nodules in explanted lungs 21 days after surgical resection of the PT (Figure 20E; courtesy of Niccolò Roda).

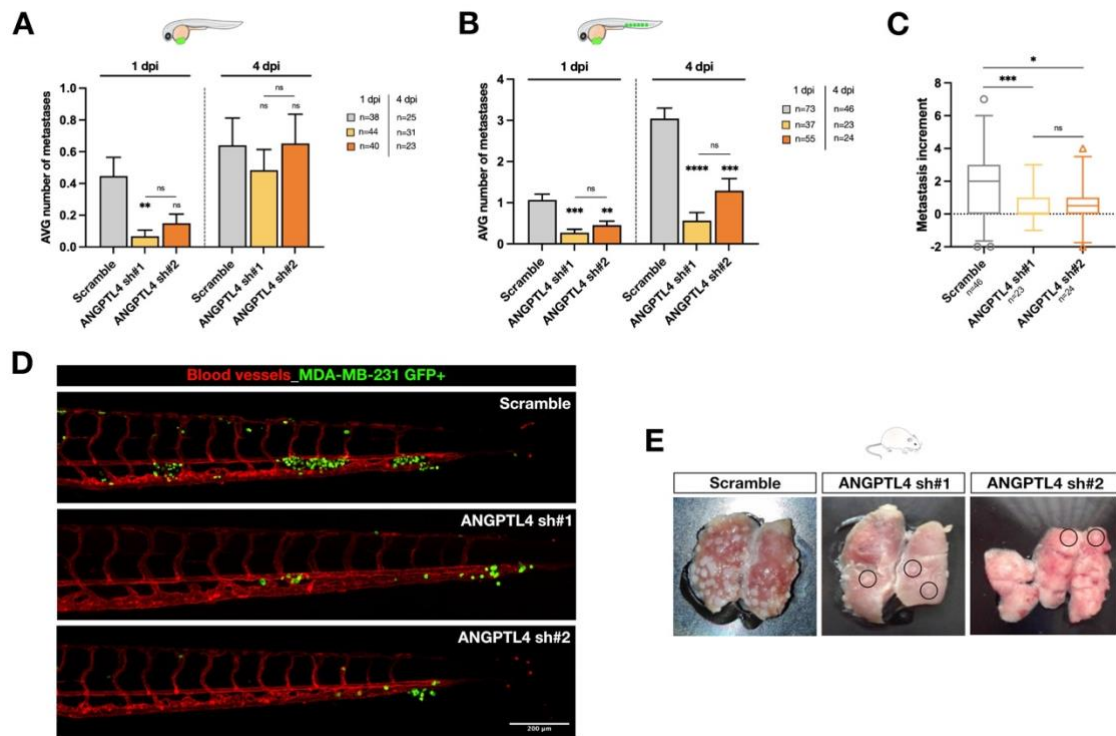


Figure 20 | Number of MDA-MB-231 metastases in zebrafish xenografts upon ANGPTL4 silencing. Quantification of the AVG number of metastases at 1 dpi and 4 dpi for subcutaneous injection (**A**) and for intravenous injection (**B**). Results are expressed as AVG±SEM. Metastasis increment in intravenously transplanted fish is measured as Δ metastases between 4 dpi and 1 dpi. Results are expressed as median±95% CI (**C**). Number of analyzed xenografts are reported in the graphs. Statistical analysis: Kruskal-Wallis test. * $p < 0.05$, ** $p < 0.01$, *** $p < 0.001$, **** $p < 0.0001$, ns= not significant. Representative z-stack confocal images of the CHT of live *Tg(kdrl:DsRed)* fish at 4 dpi, transplanted either with scramble or ANGPTL4 KD MDA-MB-231 cells. Green: human BC cell nuclei; red: blood vessels. Scale bar= 200 μ m (**D**). Representative images of surgically resected lungs. Circles highlight micro-metastases. Data on mouse xenografts were a courtesy of Niccolò Roda (**E**).

Finally, I computed the frequency of MIC, normalizing numbers of metastases over the total number of cells composing the PT at 4 dpi (Figure 21). I observed that subcutaneously transplanted ANGPTL4-interfered cells initiate the metastatic cascade – starting from local invasion at PT level – with the same rate as control cells ($0.45 \pm 0.06\%$), for both the shRNAs (sh#1 $0.57 \pm 0.18\%$, $p = 0.8168$; sh#2 $0.54 \pm 0.12\%$, $p = 0.9936$). On the contrary, when cells were directly placed in the circulation, ANGPTL4 silencing strongly impaired the extravasation frequency (sh#1 $0.66 \pm 0.21\%$, $p = 0.0013$; sh#2 $1.08 \pm 0.23\%$, $p = 0.0120$), with respect to control cells ($2.15 \pm 0.28\%$), thereby confirming the role of ANGPTL4 in the late stage of BC metastatic cascade.

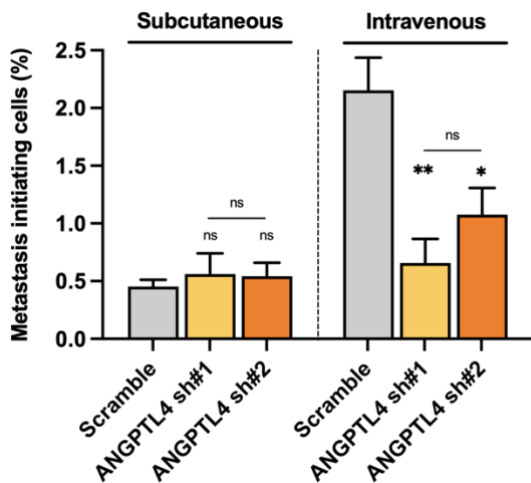


Figure 21 | Frequency of metastasis initiating cells for MDA-MB-231 cells upon ANGPTL4 silencing. Percentage of MIC was measured 4 dpi for both subcutaneously (**left**) and intravenously (**right**) injected xenografts. Results are expressed as $AVG \pm SEM$. Number of xenografts analyzed are the following: scramble, $n=8$; ANGPTL4 sh#1 $n=7$; ANGPTL4 sh#2, $n=9$. Statistical analysis: one-way ANOVA followed by Tuckey's *post-hoc* test. ** $p < 0.01$, * $p < 0.05$, ns= not significant.

The size distribution of metastases in subcutaneously injected 4 dpi xenografts was significantly skewed towards smaller masses and no overt metastases were detected (sh#1, $p=0.0048$; sh#2, $p=0.0023$; Figure 22B) indicating that, despite the incidence and numbers of metastases remain unchanged in this condition, ANGPTL4 KD pro-metastatic cells mostly seed as micro-metastases. On the contrary, upon intravenous injection, residual ANGPTL4 KD metastases distributed equally among micro-, mid-size and overt metastases, showing no differences with respect to scrambled cells at both 1 dpi (sh#1, $p=0.2541$; sh#2, $p=0.4054$; Figure 22C) and 4 dpi (sh#1, $p=0.8711$; sh#2, $p=0.3540$; Figure 22D) suggesting that, once cells have extravasated and seeded in the foreign environment, ANGPTL4 does not exert any effect on BC cells colonization dynamics.

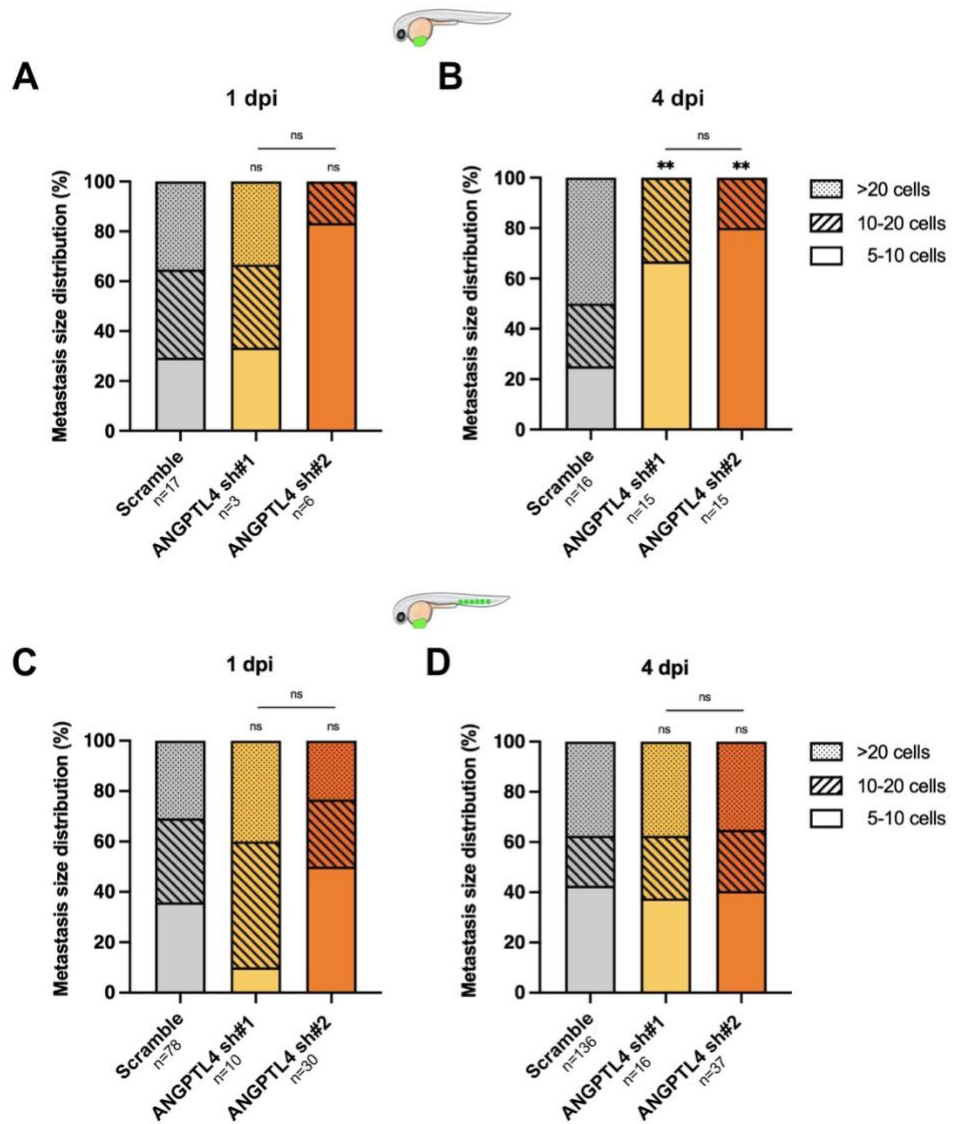


Figure 22 | Size distribution of MDA-MB-231 metastases in zebrafish xenografts upon ANGPTL4 silencing. Comparison between metastasis size distribution between fish transplanted subcutaneously at 1 dpi and 4 dpi (A, B) and intravenously at 1 dpi and 4 dpi (C, D) either with scrambled and ANGPTL4 KD cells. Number of analyzed metastases are reported in the graphs. Statistical analysis: Chi-square test. $**p < 0.01$; ns= not significant.

4.3.3 ANGPTL4 is a determinant of metastatic burden

The metastatic-burden index expresses the severity of metastatic progression, considering both numerosity and size of metastases in each xenograft. Examination of subcutaneously and intravenously injected fish at 1 and 4 dpi revealed that metastatic burden is significantly lower for ANGPTL4 KD cells injected in the circulation, as compared to control (Figure 23B) or PVS-injected cells (Figure 23A). Moreover, contrary to scrambled MDA-MB-231 cells – whose metastatic burden increases over time, mirroring the worsening of the conditions of the animals – I did not observe any variations in the conditions of xenografts lacking ANGPTL4 (Figure 23C).

Since zebrafish xenografts benefit from the lack of ANGPTL4 in terms of their grade of metastatic disease, mainly impairing the capacity of cells to extravasate when placed in the circulation, ANGPTL4 represents a determinant of BC metastatic progression, acting late in the multistep cascade.

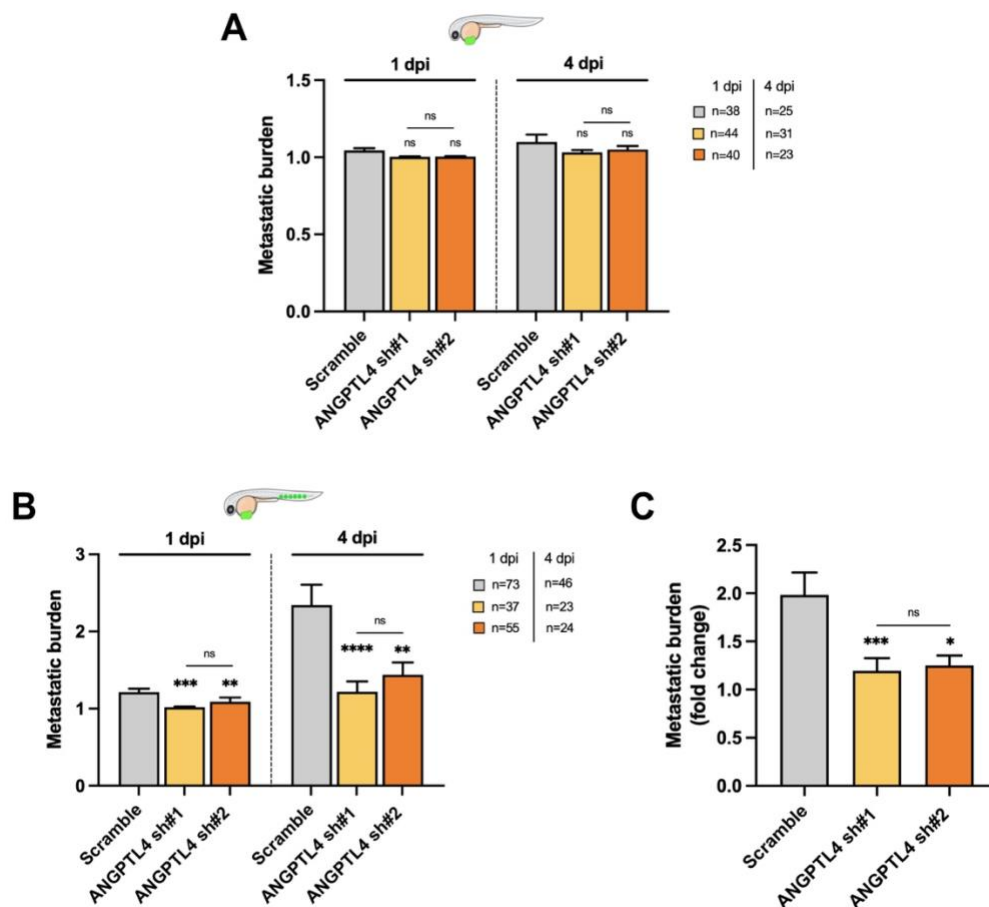


Figure 23 | Metastatic burden of MDA-MB-231 BC cells in zebrafish xenografts upon ANGPTL4 signaling. Quantification of the metastatic burden in xenografts transplanted with scramble and ANGPTL4 cells at 1 dpi and 4 dpi either subcutaneously (A) and intravenously (B). Measurement of metastatic burden fold change between 1 dpi and 4 dpi for intravenous injection (C). Results are expressed as $AVG \pm SEM$. Statistical analysis: Kruskal-Wallis test. Numbers of analyzed xenografts are reported in the graphs. * $p < 0.05$, ** $p > 0.01$, *** $p < 0.001$, **** $p < 0.0001$, ns= not significant.

4.3.4 ANGPTL4 does not impact on metastasis cell proliferation and outgrowth

Finally, I sacrificed animals and I evaluated metastasis cell proliferation according to size category, checking expression of the Ki67 marker. Interestingly, I observed that the proliferative index of micro-, mid-size and overt metastases at 4 dpi was not effected by ANGPTL4 silencing (Figure 24A), indicating that extravasated cells grew similarly to

control at the metastatic site. Overall, the proliferative index of ANGPTL4 KD cells was equal to $22.5 \pm 7.4\%$ in micro-metastases ($p=0.8799$), $42.3 \pm 7.2\%$ in mid-size metastases ($p=0.1950$) and $20.4 \pm 4.2\%$ in overt metastases ($p=0.1714$).

Consistently, control and ANGPTL4-interfered overt metastases presented similar sizes, being composed by 46 cells/metastasis and 40 cells/metastasis respectively ($p=0.4651$; Figure 24B). Therefore, once cells have seeded, ANGPTL4 does not contribute to metastatic cell expansion in the foreign organ. For both analyses, the two shRNAs were merged in order to achieve a good sample size.

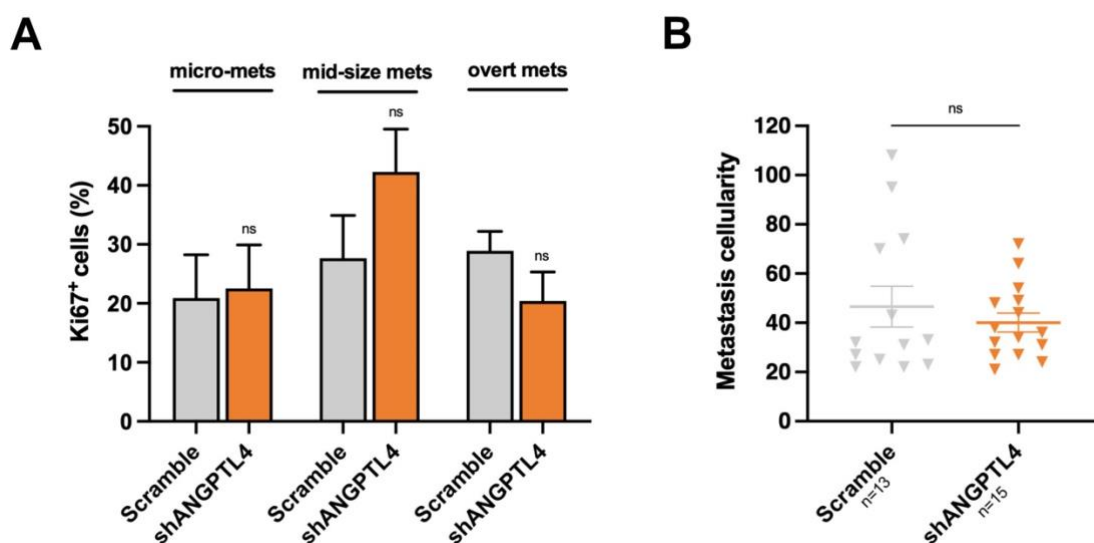


Figure 24 | Metastasis proliferation and outgrowth of MDA-MB-231 metastases in zebrafish xenografts upon ANGPTL4 silencing. Analysis of metastatic cell proliferation in micro-, mid-size and overt metastases between scramble and ANGPTL4 KD-injected fish. Results are expressed as $AVG \pm SEM$. Numbers of analyzed xenografts are the following: micro-metastases scramble $n=7$, shANGPTL4 $n=9$; mid-size metastases, scramble $n=6$, shANGPTL4 $n=9$; overt metastases, scramble $n=13$, shANGPTL4 $n=15$. Statistical analysis: one-way ANOVA followed by Tuckey's *post-hoc* test. **(A)**. Comparison of 4 dpi overt metastases size in fish transplanted either with scramble or ANGPTL4 KD cells. Results are expressed as $AVG \pm SEM$. Each symbol in the dot plot represents a single xenograft. Numbers of analyzed xenografts are reported in the graph. Statistical analysis: *t* test **(B)**. Metastasis cellularity and percentage of Ki67⁺ cells was measured on confocal images of fixed 4 dpi xenografts, using Arivis Vision 4D 3.5.0 software. ShRNAs were merged to reach a good sample size. ns= not significant.

4.3.5 Summary

Since its contribution in BC metastatization was already reported, ANGPTL4 was used to validate my assay. Indeed, evidence reported in the previous paragraphs confirmed zebrafish larval xenografts as a reliable platform to accurately and rapidly identify stage-specific vulnerabilities of the metastatic process. Besides confirming the role of ANGPTL4 in the steps of extravasation and seeding of BC cells, zebrafish xenografts quantitatively defined the impact of ANGPTL4 on BC metastatic progression. Table 2 illustrates a comprehensive summary of all measurable parameters describing metastatic cascade and PT growth of control and ANGPTL4-interfered MDA-MB-231 cells in zebrafish *larvae*. Results of the two shRNAs used in the experiments were merged. Controls are represented by cells transduced with the scrambled construct. Significant *p* values are highlighted in bold red.

Table 2 | Validation of ANGPTL4: summary of quantitative analyses.

| Metastatic phase explored | Quantitative parameters of metastatic progression | | ANGPTL4_merged | Control | <i>p</i> value |
|---|--|-------------|---------------------|---------------------|-----------------------------|
| Metastatic efficiency according to either intravasation or extravasation capacity | Incidence of metastasis_1d (%) | S.I. | 11 | 32 | 0.0029 |
| | | I.I. | 29 | 61 | <0.0001 |
| | Incidence of metastasis_4d (%) | S.I. | 41 | 44 | 0.81034 |
| | | I.I. | 46 | 93 | <0.0001 |
| Extent of metastatic seeding | Number of metastasis_1d | S.I. | 0.11 | 0.45 | 0.0591 |
| | | I.I. | 0.38 | 1.07 | 0.0025 |
| | Number of metastasis_4d | S.I. | 0.55 | 0.64 | >0.9999 |
| | | I.I. | 0.94 | 3.04 | <0.0001 |
| Pro-metastatic cells with either intravasating or extravasating properties | Frequency of metastasis initiating cells (%) | S.I. | 0.55 | 0.45 | 0.9760 |
| | | I.I. | 0.89 | 2.15 | <0.0001 |
| Metastatic colonization | Metastasis size distribution_1d (%) (5-10;10-20;20+) | S.I. | 67-22-11 | 30-35-35 | 0.4579 |
| | | I.I. | 41-33-26 | 36-33-31 | 0.9761 |
| | Metastasis size distribution_4d (%) (5-10;10-20;20+) | S.I. | 73-27-0 | 25-25-50 | 0.0036 |
| | | I.I. | 40-25-35 | 42-20-38 | 0.7189 |
| Severity of metastatic progression | Metastatic burden_1d | S.I. | 1.00 | 1.04 | 0.0374 |
| | | I.I. | 1.06 | 1.21 | 0.003 |
| | Metastatic burden_4d | S.I. | 1.04 | 1.1 | >0.9999 |
| | | I.I. | 1.32 | 2.34 | <0.0001 |
| Proliferation of metastatic cells | Metastasis proliferative index_4d (%) | 5-10 cells | 22.53 | 20.91 | 0.8799 |
| | | 10-20 cells | 42.27 | 27.66 | 0.1950 |
| | | 20+ cells | 20.39 | 28.88 | 0.1714 |
| Outgrowth | Metastasis outgrowth_4d (n° cells) | | 40 | 46 | 0.4651 |
| PT phenotype explored | Quantitative parameters of PT progression | | ANGPTL4_merged | Control | <i>p</i> value vs sh merged |
| CSC-like content, innate immune-evasion | Implantation potential_4d (%) | | 94 | 93 | 0.6383 |
| Growth | PT size_4d (n° cells) | | 164 | 163 | 0.9878 |
| | PT volume_4d (µm ³) | | 7.5x10 ⁵ | 9.0x10 ⁵ | 0.5103 |
| | PT proliferative index_4d (%) | | 24.98 | 28.08 | 0.4767 |

4.4 *In vivo* validation of putative gene-dependencies of BC metastatic progression

The aim of the following experiments is the *in vivo* validation, using the zebrafish model, of 5 additional candidate genes, whose general role and stage-specific functions in the BC metastatic cascade had never been characterized before. These targets were part of the BC pro-metastatic transcriptional signature identified by exploiting the clonal tracking approach briefly described in paragraph 4.3 and include: KCNQ1OT1, ITGB4, LY6E, IFI6 and FST. They were prioritized based on folds of up-regulation in the pro-metastatic clones and their ability to function as a prognostic factor in BC patients. As for ANGPTL4, MDA-MB-231-GFP⁺ cells were infected with lentiviruses expressing two distinct shRNAs for each of the candidate genes, or scrambled shRNA as a control, and injected in *Tg(kdrl:DsRed)* zebrafish *larvae* either subcutaneously or intravenously. PT growth and metastatic spreading were monitored by *in vivo* and *ex vivo* imaging at 1 and 4 dpi.

4.4.1 KCNQ1OT1

KCNQ1 Opposite Strand/Antisense Transcript 1 (KCNQ1OT1) is antisense to the KCNQ1 gene and is an unspliced long non-coding RNA, preferentially expressed from the paternal allele. KCNQ1OT1 interacts with chromatin, regulating transcription of multiple genes via epigenetic modifications [Mitsuya *et al.*, 1999; Pandey *et al.*, 2008]. Its abnormal expression is associated with the onset of growth disorders, such as Beckwith-Wiedemann syndrome [Lee *et al.*, 1999]. Preliminary data implicate KCNQ1OT1 in colorectal and melanoma carcinogenesis [Zhang *et al.*, 2019; Guo *et al.*, 2018], as well as chemoresistance in lung adenocarcinoma [Ren *et al.*, 2017b].

KCNQ1OT1-interfered cells successfully implanted in zebrafish *larvae*, originating a PT mass at the site of injection in ~91% of the cases, showing no differences respect to scrambled cells (91% *vs.* 93%; $p=0.7188$; Figure 25A-A'). Nevertheless, PT size at 4 dpi – expressed as the total number of cells that constitute the mass – was reduced by ~2.5 folds with respect to control (125±21 cells *vs.* 302±49 cells; $p=0.0022$; Figure 25B), consistent with the strong impairment in proliferation (Ki67 index) observed for KCNQ1OT1 KD tumors (12.5±1.6% *vs.* 5.9±1.4%; $p=0.0092$; Figure 25C).

Same results were obtained upon xenotransplantation in immunocompromised mice, which showed that KCNQ1OT1 is involved in the formation of a noticeable PT mass *in vivo* (Figure 25D, data courtesy of Niccolò Roda)

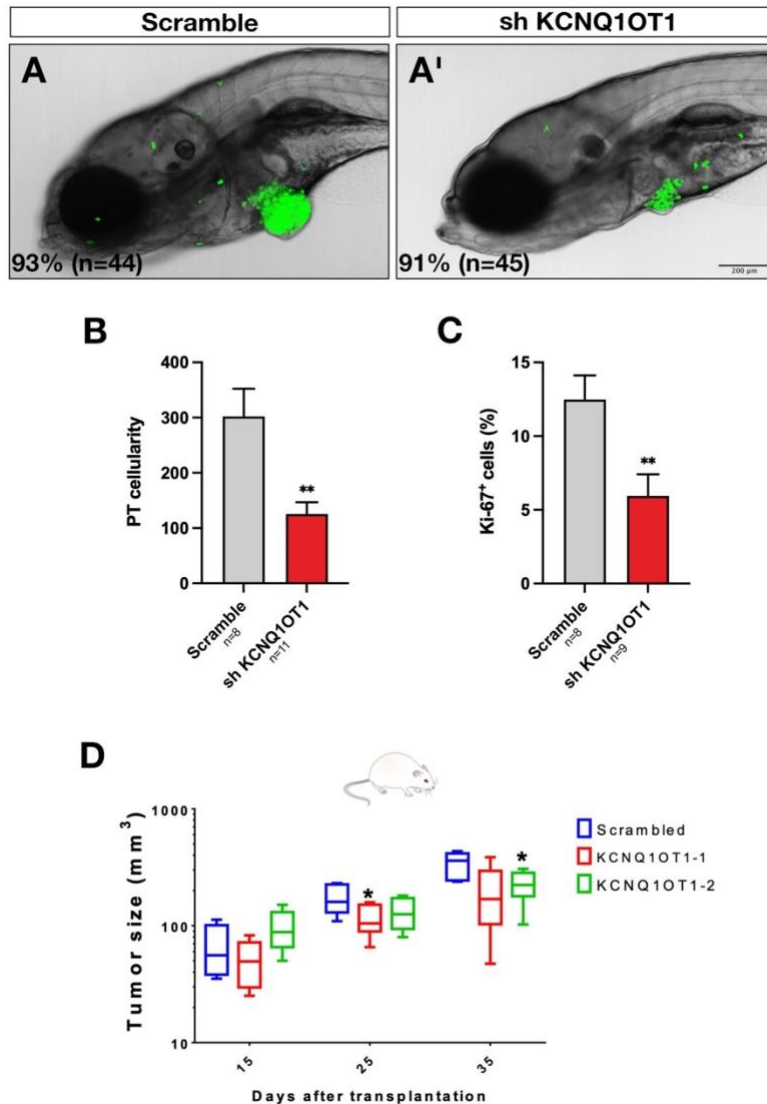


Figure 25 | Analysis of PT growth in zebrafish xenografts upon KCNQ10T1 silencing. Z-stack confocal images of live 4 dpi xenografts transplanted with scramble (A) and sh KCNQ10T1 (A') MDA-MB-231 cells, representing PTs grafted at the site of injection. Green: human BC cell nuclei. Scale bar= 200 μ m. Implantation potential was measured at 4 dpi and reported in the lower left corner. Quantification of the PT cellularity (B) and proliferative index (C) was performed *ex vivo* at 4 dpi using a Arivis Vision 4D 3.5.0 software. Number of analyzed xenografts are reported in the graphs. ShRNAs were merged. Statistical analysis: *t* test. ** $p < 0.01$. PT growth in the mouse model. Data on mouse xenografts were a courtesy of Niccolò Roda (D).

Numbers of xenografts that develop metastases at 4 dpi was reduced by half upon KCNQ10T1 silencing when cells are directly placed in the circulation (36% vs. 68%; $p=0.0067$), whereas it did not change when cells are injected subcutaneously (24% vs. 38%; $p=0.4473$; Figure 26A). Thus, similarly to what I had already noticed for ANGPTL4 (paragraph 4.3.2), the lack of KCNQ10T1 does not affect MDA-MB-231 EMP (67% vs. 56%), but reduces LMP.

Likewise, both the AVG number of extravasated metastatic growths ($p=0.0034$; Figure 26B,C) and metastatic-burden index at 4 dpi ($p=0.0073$; Figure 26E) were lower in

xenografts transplanted intravenously with KCNQ1OT1 KD cells with respect to control. On the contrary, metastasis size distribution was not affected by KCNQ1OT1 silencing for both modalities of injection (S.I., $p=0.0787$; I.I., $p=0.1146$; Figure 26D). Metastatic behavior of KCNQ1OT1 cells was also validated in mice, recapitulating the same observations obtained in zebrafish xenografts (data not shown).

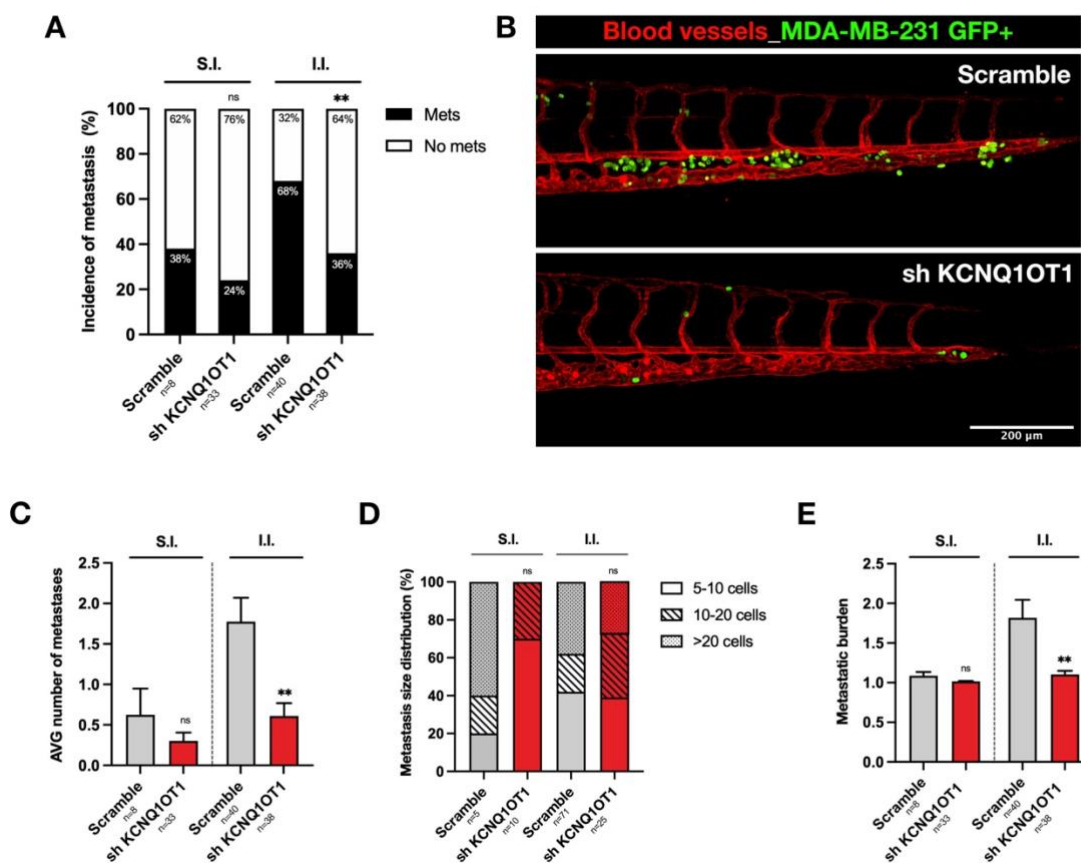


Figure 26 | In vivo validation of metastatic behavior of MDA-MB-231 cells upon KCNQ1OT1 silencing in zebrafish xenografts. Quantification of incidence of metastasis formation in 4 dpi for xenografts transplanted with subcutaneous (S.I.) and intravenous (I.I.) injection either with scrambled or KCNQ1OT1 KD MDA-MB-231 cells (A). Representative z-stack confocal images of the CHT of live *Tg(kdrl:DsRed)* fish at 4 dpi, transplanted either with scrambled or KCNQ1OT1 KD. Green: human BC cell nuclei; red: blood vessels. Scale bar= 200 μ m (B) Quantification of the AVG number of metastases at 4 dpi for S.I. and I.I. Results are expressed ad AVG \pm SEM. Number of analyzed xenografts are reported in the graph. Statistical analysis: Kruskal-Wallis test (C). Comparison between metastasis size distribution at 4 dpi for S.I. and I.I. Number of analyzed metastases are reported in the graphs. Statistical analysis: Chi-square test (D). Quantification of the metastatic burden at 4 dpi for S.I. and I.I. Results are expressed ad AVG \pm SEM. Number of analyzed xenografts are reported in the graph. Statistical analysis: Kruskal-Wallis test (E). ShRNAs were merged. ** $p<0.01$, ns= not significant.

In summary, these experiments demonstrate a strong reduction of the metastatic potential of BC cells lacking the expression of KCNQ1OT1, most likely due to an impairment of the their ability to extravasate, whereas intravasation and colonization of

distant sites were not affected. Moreover, KCNQ1OT1 also plays a role in breast PT growth, promoting cell proliferation. Thus, KCNQ1OT1 involvement in BC metastatic progression was successfully validated *in vivo*, both in zebrafish and in mouse models.

4.4.2 ITGB4

Integrin $\beta 4$ (ITGB4) gene encodes for the $\beta 4$ subunit of the protein $\alpha 6\beta 4$ integrin. This protein is mainly found in epithelial cells and functions as a receptor for laminin in junctional adhesion complexes called hemidesmosomes. ITGB4 promotes cell-to-cell and cell-to-matrix adhesion and mediates signal transduction [Stewart and O'Connor, 2015]. Mutations in this gene are commonly associated with skin defects, namely epidermolysis bullosa [Ashton *et al.*, 2001]. ITGB4 is also known to play a pivotal role in the biology of invasive carcinomas – including lung, prostate, colon and BC – being correlated to tumor invasion and migration [Ruan *et al.*, 2020; Yang *et al.*, 2021]. However, its direct implication in BC metastasis has not been elucidated yet.

First, I observed that ITGB4 KD MDA-MB-231 cells display a good implantation rate at 4 dpi, although slightly but significantly lower with respect to control cells (76% *vs.* 94%; $p=0.0042$; Figure 27A-A'). PT size was heavily affected by the lack of ITGB4 (Figure 27B): PTs from interfered cells were composed by 97 ± 16 cells, whereas PT cellularity in control fish amounted to 258 ± 69 cells ($p=0.0053$). Interestingly, engraftment capacity and growth of ITGB4 silenced tumors did not seem to correlate with cell proliferation (Figure 27C), that was relatively low but comparable between the two groups (9.1 ± 1.5 *vs.* 5.7 ± 2.2 in control cells; $p=0.2220$).

These analyses suggested that ITGB4 is involved in PT formation, although not significantly implicated in BC cell proliferation *in vivo*. Further experiment are required to understand whether lower tumor engraftment and growth might be due to reduced cell survival or be a consequence of innate immune clearance.

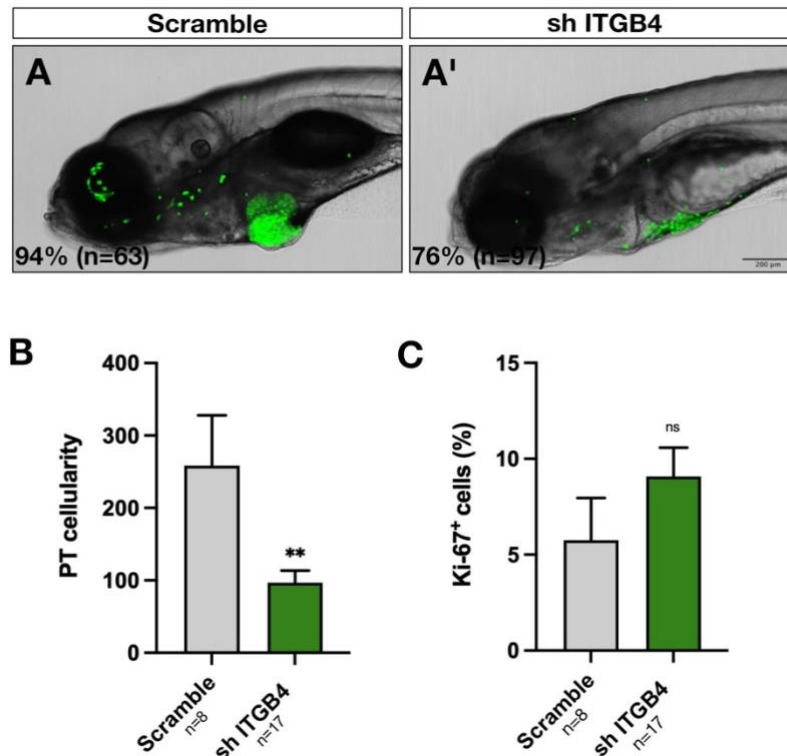


Figure 27 | Analysis of PT growth in zebrafish xenografts upon ITGB4 silencing. Z-stack confocal images of live 4 dpi xenografts transplanted with scramble (A) and sh ITGB4 (A') cells, representing PTs grafted at the site of injection. Green: human BC cell nuclei. Scale bar= 200 μ m. Implantation potential was measured at 4 dpi and reported in the lower left corner. Quantification of the PT cellularity (B) and proliferative index (C) was performed *ex vivo* at 4 dpi using a Arivis Vision 4D 3.5.0 software. Number of analyzed xenografts are reported in the graphs. Statistical analysis: *t* test. ** $p < 0.01$, ns= not significant.

I then investigated the metastatic behavior of MDA-MB-231 cells lacking ITGB4. Exploiting both subcutaneous (S.I.) and intravenous (I.I.) modalities of cell injection, I observed a relevant reduction of the number of xenografts presenting distant metastases (incidence of metastasis) in both conditions (Figure 28A). In detail, ITGB4 KD cells formed metastases in only 23% of xenografts at 4 dpi, with respect to 100% of metastasis incidence in fish subcutaneously injected with control cells ($p < 0.0001$). Most notably, ITGB4 KD cells formed metastases in ~49% of intravenously injected animals, as compared to 88% incidence with control cells ($p < 0.0001$), suggesting involvement of ITGB4 also in the later phases of BC metastasis progression. The same trend in the efficiency of metastasis formation upon I.I. was observed at 1 dpi, further confirming a possible impact of ITGB4 on extravasation (data not shown). Quantification of EMP and LMP revealed, as suggested by the previous observations, no differences in the two indexes (47% vs. 49%).

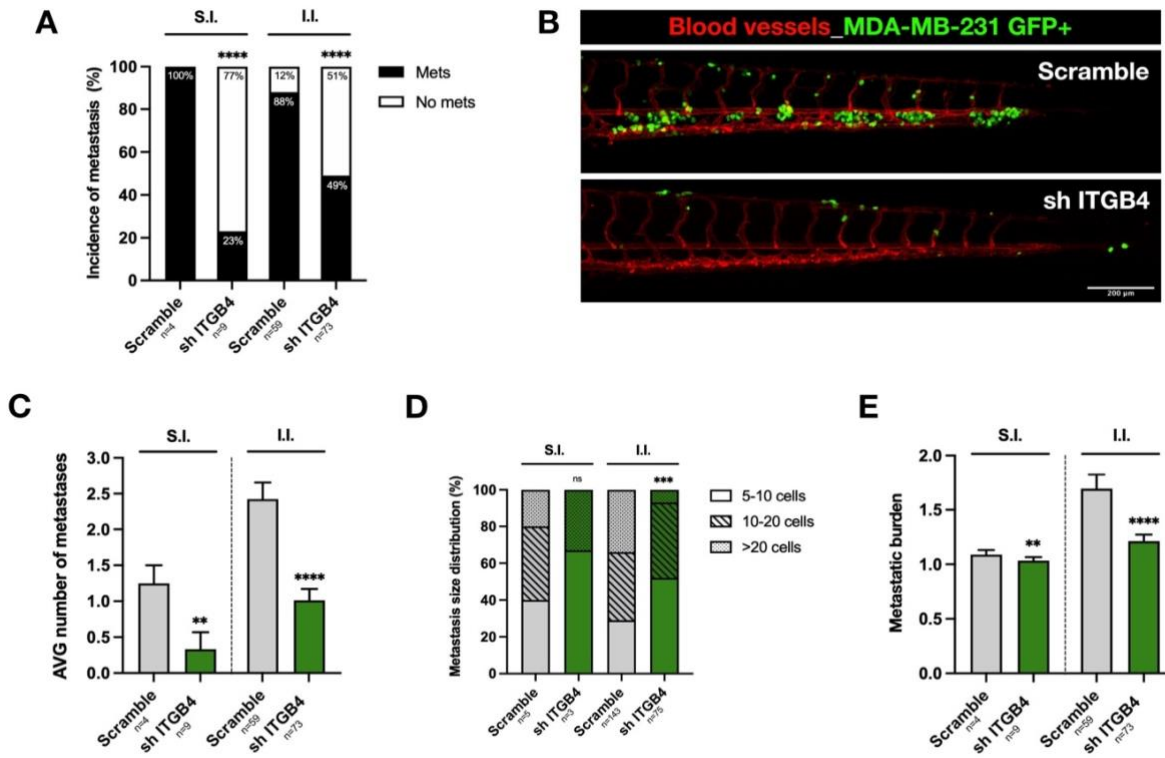


Figure 28 *In vivo* validation of metastatic behavior of MDA-MB-231 cells upon ITGB4 silencing in zebrafish xenografts. Quantification of incidence of metastasis formation in 4 dpi for xenografts transplanted with subcutaneous (S.I.) and intravenous (I.I.) injection either with scrambled or ITGB4 KD MDA-MB-231 cells (A). Representative z-stack confocal images of live *Tg(kdrl:DsRed)* fish at 4 dpi, transplanted either with scrambled or ITGB4 KD cells. Green: human BC cell nuclei; red: blood vessels. Scale bar= 200 μm (B) Quantification of the AVG number of metastases at 4 dpi for S.I and I.I. Results are expressed ad AVG±SEM. Number of analyzed xenografts are reported in the graph. Statistical analysis: Kruskal-Wallis test (C). Comparison between metastasis size distribution at 4 dpi for S.I. and I.I. Number of analyzed metastases are reported in the graphs. Statistical analysis: Chi-square test (D). Quantification of the metastatic burden at 4 dpi for S.I. and I.I. Results are expressed ad AVG±SEM. Number of analyzed xenografts are reported in the graph. Statistical analysis: Kruskal-Wallis test (E). ShRNAs were merged. ** $p < 0.01$, *** $p < 0.001$, **** $p < 0.0001$, ns= not significant.

I also detected significantly reduced numbers of extravasated tumor growths in CHT of both subcutaneously and intravenously transplanted *larvae* (S.I., $p=0.0038$; I.I., $p < 0.0001$; Figure 28B,C). Accordingly, metastatic colonization was also impaired by the silencing of ITGB4, as shown by the different size-distribution of metastases at 4 dpi between scrambled and ITGB4 KD cells upon I.I. ($p=0.0003$; Figure 28D). In detail, the lack of ITGB4 significantly skewed metastasis distribution towards small micro-metastases (5-10 cells) and impaired the onset of overt metastases (>20 cells). Consistently, also the metastatic burden, which measures the severity of metastatic progression in zebrafish *larvae*, was lower in xenografts transplanted with ITGB4-interfered cells for both modalities of injection (S.I., $p=0.0036$; I.I., $p < 0.0001$; Figure 28E).

To conclude, ITGB4 involvement in BC metastatic process was successfully validated *in vivo* in the zebrafish model. Data demonstrated that ITGB4 exerts multiple roles

during tumor progression, functioning at different levels of the metastatic cascade, including PT growth, intravasation, extravasation and colonization.

4.4.3 LY6E

Lymphocyte antigen 6 family member E (LY6E) gene encodes a glycosylated cell surface protein whose transcription is activated by interferons and plays critical roles in T cell functions and immune modulation, including response to viral infections [Mar *et al.*, 2018]. LY6E role in oncogenesis still remains poorly understood, although few studies reported that its overexpression correlates with poor BC therapeutic outcomes [AlHossiny *et al.*, 2016].

LY6E silencing moderately, yet significantly, compromised the capacity of MDA-MB-231 BC cells to form a noticeable PT mass at the injection site at 4 dpi, with 72% of shLY6E-transplanted fish harboring a tumor, as compared to 98% of scramble-transplanted animals ($p=0.0004$; Figure 29A-A'). Moreover, as shown by the representative images in panel A-A', LY6E interfered cells developed tumors with a decreased size with respect to control. These observations – although PT cellularity and proliferation have not been quantified yet in the zebrafish model – are consistent with literature data, which reported reduced formation of xenografted tumors in mice upon LY6E silencing [AlHossiny *et al.*, 2016] and suggested that LY6E is required for BC implantation and tumor growth *in vivo*.

Subsequently, the metastatic potential of LY6E interfered cells was assessed in subcutaneously and intravenously transplanted *larvae*. I observed that LY6E impacts the efficiency of metastasis formation, similarly to what already described for ITGB4 (Figure 29B). Indeed, the percentage of xenografts carrying metastases dramatically decreased from 79% to 10% upon S.I. ($p=0.0009$) whereas, when the early steps of the metastatic cascade are circumvented via I.I., incidence of metastasis was only slightly reduced (55% *vs.* 87%, $p=0.0053$). In addition, frequencies of distant metastases onset were expressed also as metastatic potential indexes, revealing 18% of EMP *vs.* 55% of LMP for LY6E KD cells. Overall these data suggest that LY6E promotes early phases of metastatization, consistently with its reported role in TGF β and Smad signaling, known mediators of EMT in solid tumors [AlHossiny *et al.*, 2016].

I also measured a significant reduction in numbers of CHT metastases (S.I. $p=0.0003$; I.I., $p=0.0053$; Figure 29C,D) and in metastatic burden (S.I., $p=0.0010$; I.I., $p=0.0021$; Figure 29F) for both conditions at 4 dpi. On the other hand, CHT colonization did not seem to be impaired, since cells lacking LY6E expression developed extravasated masses indiscriminately distributed among the three size categories, although sample size

for S.I. should be increased to achieve statistical robustness (S.I., $p=0.5796$; I.I., $p=0.1674$; Figure 29E).

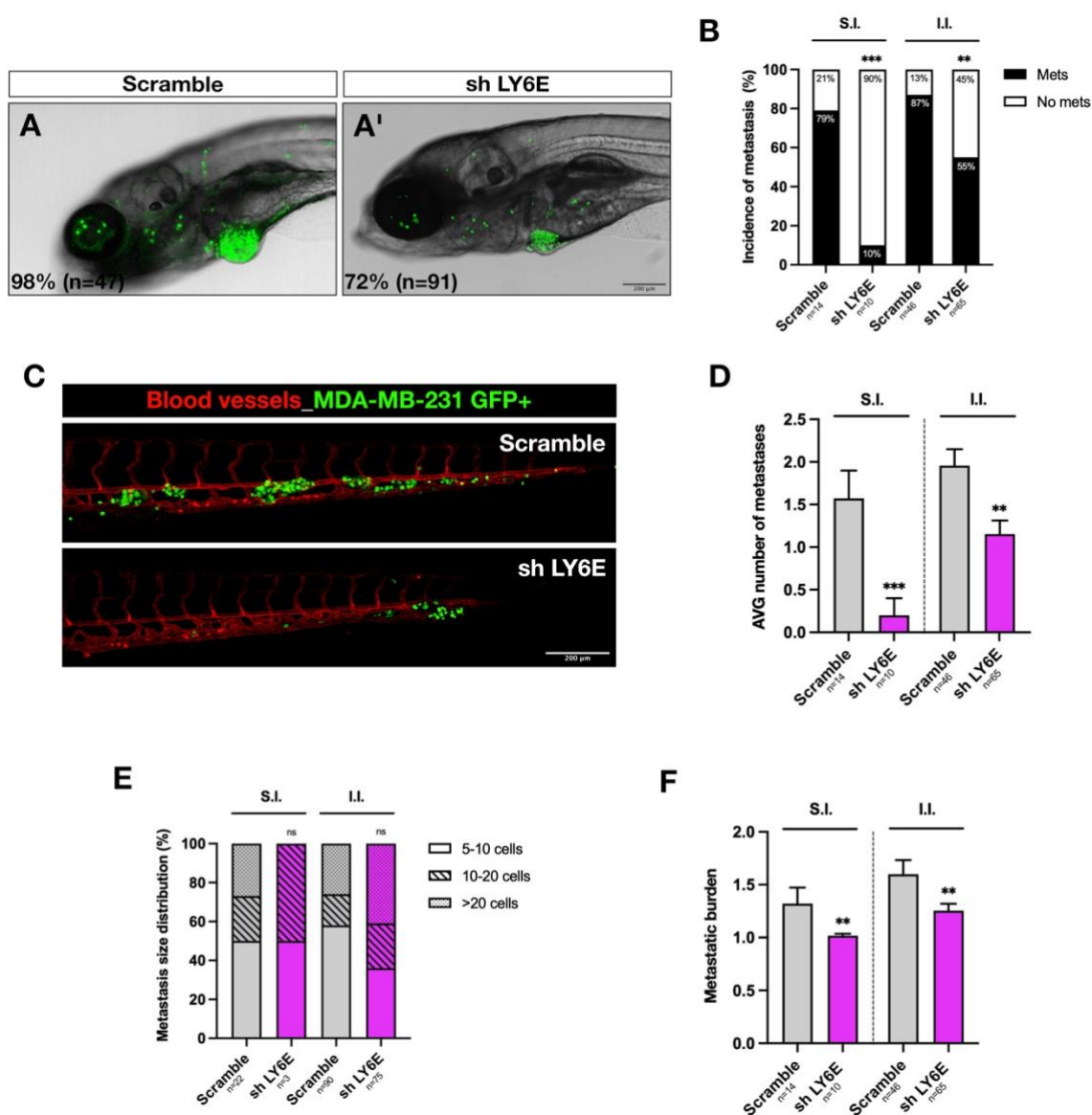


Figure 29 | *In vivo* analysis of PT growth and metastatic behavior of MDA-MB-231 cells upon LY6E silencing in zebrafish xenografts. Z-stack confocal images of live 4 dpi xenografts transplanted with scramble (A) and sh LY6E (A') MDA-MB-231 cells, representing PTs grafted at the site of injection. Green: human BC cell nuclei. Scale bar= 200 μ m. Implantation potential was measured at 4 dpi and reported in the lower left corner. Quantification of incidence of metastasis formation in 4 dpi for xenografts transplanted with subcutaneous (S.I.) and intravenous (I.I.) injection either with scrambled or LY6E KD cells (B). Representative z-stack confocal images of live *Tg(kdrl:DsRed)* fish at 4 dpi, transplanted either with scrambled or LY6E KD cells. Green: human BC cell nuclei; red: blood vessels. Scale bar= 200 μ m (C) Quantification of the AVG number of metastases at 4 dpi for S.I and I.I. Results are expressed ad AVG \pm SEM. Number of analyzed xenografts are reported in the graph. Statistical analysis: Kruskal-Wallis test (C). Comparison between metastasis size distribution at 4 dpi for S.I. and I.I. Number of analyzed metastases are reported in the graphs. Statistical analysis: Chi-square test (D). Quantification of the metastatic burden at 4 dpi for S.I. and I.I. Results are expressed ad AVG \pm SEM. Number of analyzed xenografts are reported in the graph. Statistical analysis: Kruskal-Wallis test (E). ShRNAs were merged. ** $p<0.01$, *** $p<0.001$, ns= not significant.

Overall, these analyses validate LY6E as an *in vivo* mediator of BC metastatic progression. The evidence collected in the zebrafish model, corroborated by literature data, position LY6E functions in the early steps of the metastatic cascade.

4.4.4 IFI6

Interferon alpha-inducible protein 6 (IFI6) is identified as one of the many genes induced by interferons. It encodes a mitochondrial protein involved in the negative regulation of the intrinsic apoptotic pathway. Although the molecular mechanism for the antiapoptotic effects of interferon-induced proteins in human malignancies are still unclear, IFI6 expression correlates with oncogenic progression of myeloma [Cheriyath *et al.*, 2007], gastric [Tahara *et al.*, 2005], esophageal [Liu *et al.*, 2020] and breast cancers [Cheriyath *et al.*, 2012]. Strikingly, IFI6 overexpression in BC patients is associated with reduced metastasis-free survival [Cheriyath *et al.*, 2018].

In the zebrafish xenograft model, I observed that MDA-MB-231 cell implantation at 4 dpi was comparable in IFI6 KD and scrambled cells (85% vs. 82%; $p=0.6892$; Figure 30A-A'). Interestingly, IFI6 silencing did not impact on tumor growth, since PT size was comparable in the two groups at a first visual examination. Therefore, BC cell implantation and growth in the zebrafish *larva* does not significantly depend by the pro-survival role of IFI6.

Regarding the impact of IFI6 in BC metastatic spreading, I observed a significant reduction in the incidence of metastasis at 4 dpi in the shIFI6-transplanted xenografts upon S.I. (28% vs. 59% in the control; $p=0.0208$). On the other hand, when cells were placed in the blood stream, the percentage of xenografts with CHT metastases was only weakly reduced (76% vs. 88%; $p=0.0251$; Figure 30B), suggesting the involvement of IFI6 in the early stages of the BC multistep metastatic process. Indeed, I calculated an EMP for IFI6 KD cells of 37%, as compared to 76% for LMP.

Notably, the extent of metastatic seeding at 4 dpi of MDA-MB-231 IFI6-interfered cells, measured as the AVG number of distant metastases, was strongly decreased upon I.I. ($p<0.0001$), whereas I assessed only a mild reduction for S.I. ($p=0.0495$; Figure 30C,D). Furthermore, I detected a significant shift of metastasis distribution towards larger masses following I.I. ($p=0.0025$; Figure 30E), suggesting that the onset of newly formed metastatic foci is restricted by the lack of IFI6 expression. These results indicate that, once extravasated – phases in which IFI6 is not likely to play a major role, according to collected data – IFI6 might promote metastatic cell seeding, without acting on metastasis active growth.

Accordingly, also the metastatic-burden index of IFI6 KD xenografts was significantly decreased upon I.I. ($p=0.0002$; Figure 30F).

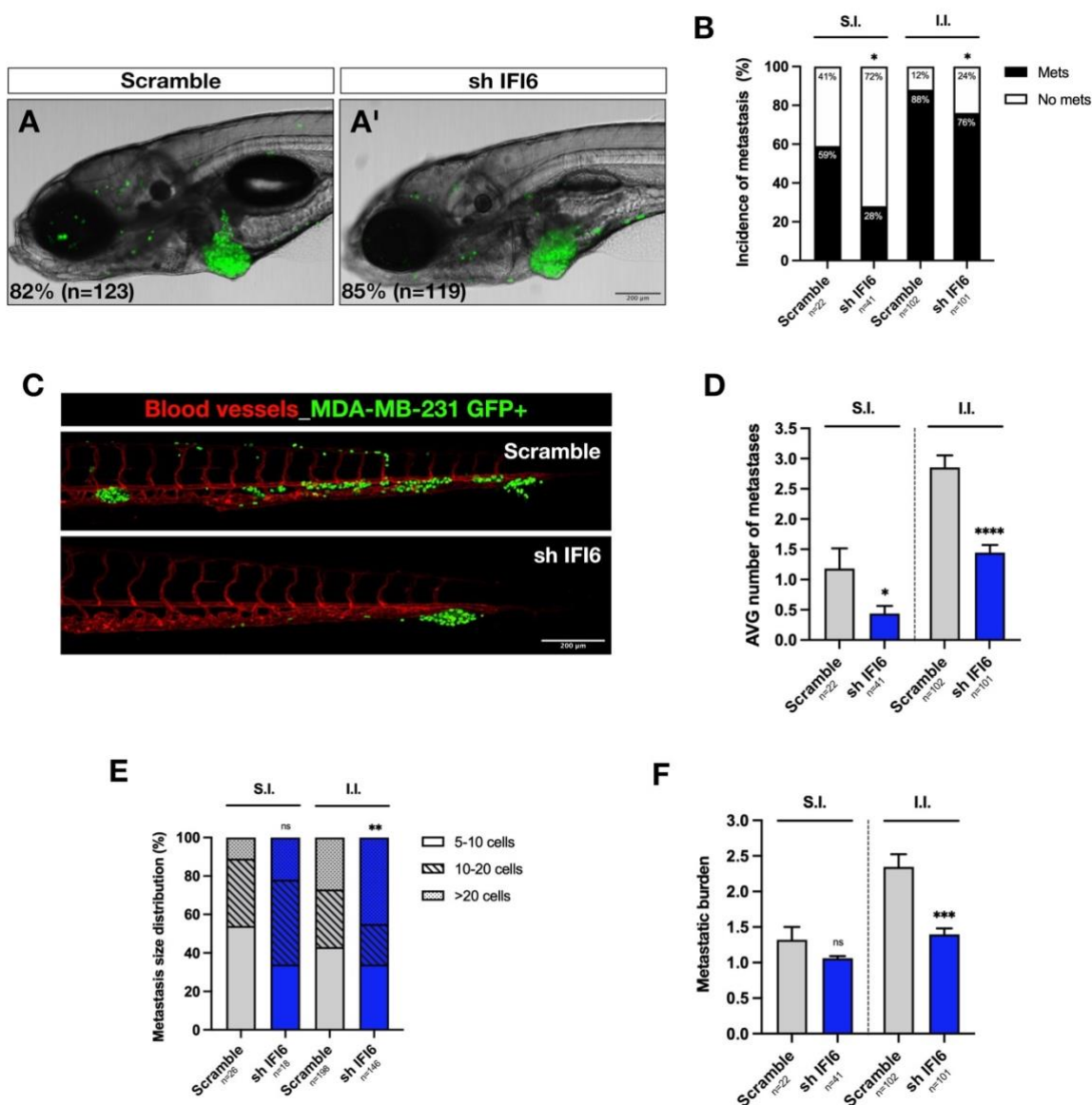


Figure 30 | *In vivo* analysis of PT growth and metastatic behavior of MDA-MB-231 cells upon IFI6 silencing in zebrafish xenografts. Z-stack confocal images of live 4 dpi xenografts transplanted with scramble (A) and sh IFI6 (A') MDA-MB-231 cells, representing PTs grafted at the site of injection. Green: human BC cell nuclei. Scale bar= 200 μ m. Implantation potential was measured at 4 dpi and reported in the lower left corner. Quantification of incidence of metastasis formation in 4 dpi for xenografts transplanted with subcutaneous (S.I.) and intravenous (I.I.) injection either with scrambled or LY6E KD cells (B). Representative z-stack confocal images of live *Tg(kdrl:DsRed)* fish at 4 dpi, transplanted either with scrambled or IFI6 KD cells. Green: human BC cell nuclei; red: blood vessels. Scale bar= 200 μ m (C) Quantification of the AVG number of metastases at 4 dpi for S.I. and I.I. Results are expressed ad $AVG \pm SEM$. Number of analyzed xenografts are reported in the graph. Statistical analysis: Kruskal-Wallis test (D). Comparison between metastasis size distribution at 4 dpi for S.I. and I.I. Number of analyzed metastases are reported in the graphs. Statistical analysis: Chi-square test (E). Quantification of the metastatic burden at 4 dpi for S.I. and I.I. Results are expressed ad $AVG \pm SEM$. Number of analyzed xenografts are reported in the graph. Statistical analysis: Kruskal-Wallis test (F). ShRNAs were merged. * $p < 0.05$, ** $p < 0.01$, *** $p < 0.001$, **** $p < 0.0001$, ns= not significant.

To conclude, IFI6 contribution to BC metastasis was validated *in vivo* in the zebrafish xenograft model. Evidence demonstrates a reduction of the metastatic potential of BC cells lacking the expression of IFI6, likely caused by impairment of their ability to intravasate and subsequently seed in the CHT of the *larva*.

4.4.5 FST

Follistatin (FST) gene encodes for a secreted extracellular regulatory protein that antagonizes, via direct binding, activin and other related members of the TGF β family, preventing access to their receptors. Since FST modulates both autocrine and paracrine cellular signals, it exerts several functions in embryogenesis, differentiation, tissue repair and immune response [Tsuchida *et al.*, 2009]. The prognostic value of FST expression has been investigated in various tumors, including BC, resulting in conflicting results on the role of this protein in cancer progression [Seachrist *et al.*, 2017; Panagiotou *et al.*, 2021].

Zebrafish *larvae* transplanted with MDA-MB-231 FST KD cells did not originate overt PTs at the injection site at 4 dpi. I observed unorganized clusters of cells of restricted dimensions (approximately 30 cells) in 73% of transplanted animals (Figure 31A-A'). Therefore, FST prevents the formation of the primary mass by impacting dramatically on BC implantation and cell survival/growth. Consistently, *in vitro* assays conducted by our laboratory revealed that FST silencing significantly restricted proliferation of MDA-MB-231 cells.

Investigation of the metastatic behavior of FST-interfered cells upon local injection is biased by the poor viability of PT cells. The tumor load that some animals presented at the injection site and in the CHT might simply reflect the originally transplanted cells progressively undergoing cell death or innate immune clearance without proliferating over the 4 days of the assay. As expected, cells lacking the expression of FST injected in the PVS (S.I.) were unable to form CHT metastases in 100% of the analyzed fish, whereas control cells metastasize in 47% of xenografts (Figure 31B). Since I detected zero metastasis in subcutaneously transplanted fish (Figure 31D), the minimum value of metastatic burden (equal to 1) was assigned to these animals, describing a metastasis-free condition (Figure 31F).

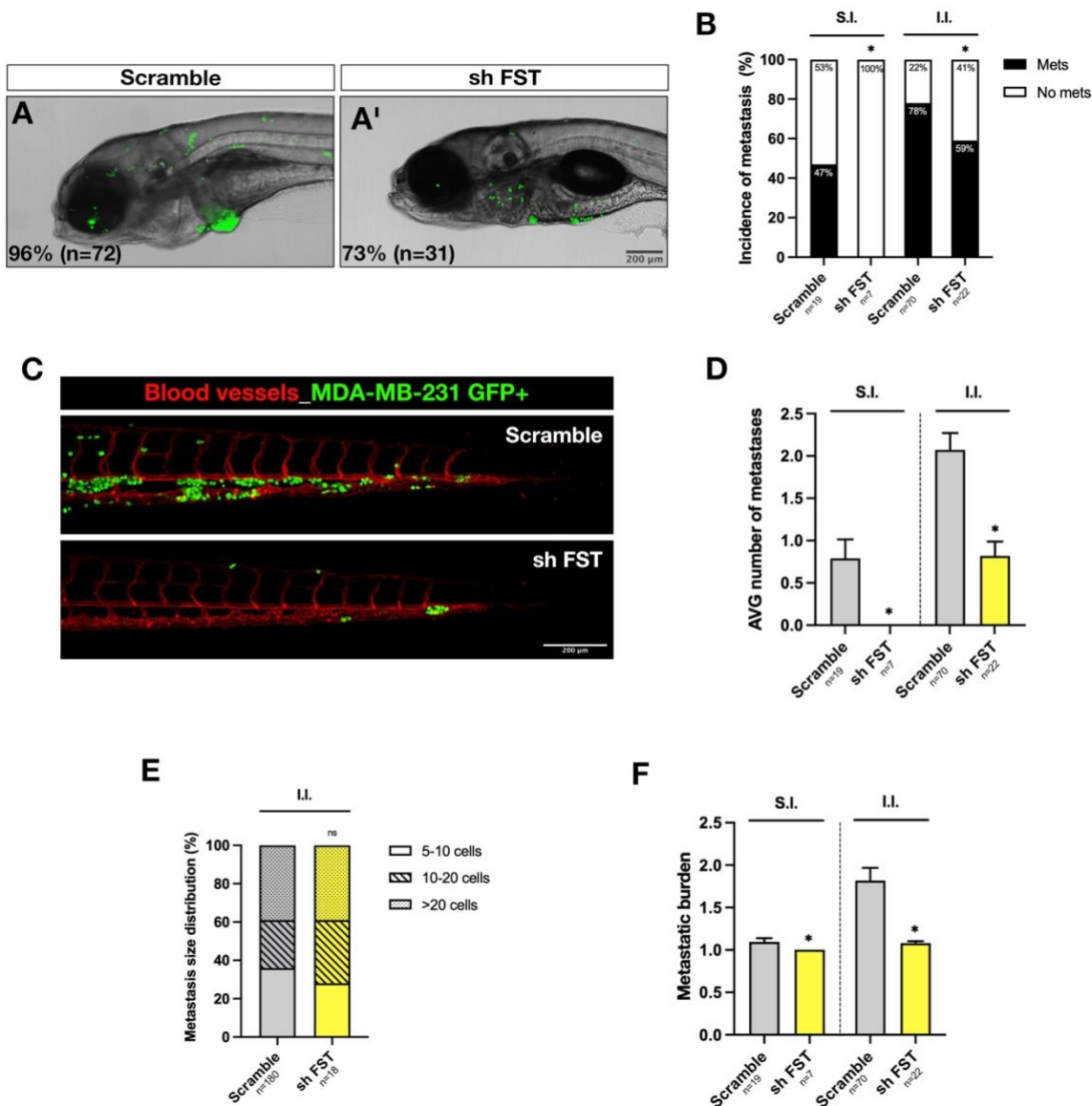


Figure 31 | *In vivo* analysis of PT growth and metastatic behavior of MDA-MB-231 cells upon FST silencing in zebrafish xenografts. Z-stack confocal images of live 4 dpi xenografts transplanted with scramble (A) and sh FST (A') MDA-MB-231 cells, representing PTs grafted at the site of injection. Green: human BC cell nuclei. Scale bar= 200 μ m. Implantation potential was measured at 4 dpi and reported in the lower left corner. Quantification of incidence of metastasis formation in 4 dpi for xenografts transplanted with subcutaneous (S.I.) and intravenous (I.I.) injection either with scrambled or FST KD cells (B). Representative z-stack confocal images of live *Tg(kdrl:DsRed)* fish at 4 dpi, transplanted either with scrambled or FST KD cells. Green: human BC cell nuclei; red: blood vessels. Scale bar= 200 μ m (C) Quantification of the AVG number of metastases at 4 dpi for S.I. and I.I. Results are expressed as $AVG \pm SEM$. Number of analyzed xenografts are reported in the graph. Statistical analysis: Kruskal-Wallis test (C). Comparison between metastasis size distribution at 4 dpi for S.I. and I.I. Number of analyzed metastases are reported in the graphs. Statistical analysis: Chi-square test (D). Quantification of the metastatic burden at 4 dpi for S.I. and I.I. Results are expressed as $AVG \pm SEM$. Number of analyzed xenografts are reported in the graph. Statistical analysis: Kruskal-Wallis test (E). ShRNAs were merged. * $p < 0.05$, ** $p < 0.01$, *** $p < 0.001$, **** $p < 0.0001$, ns= not significant.

Cells injected intravenously do not perform the entire metastatic cascade to colonize a distant site, gaining a relevant advantage respect to those cells that have to detach from the PT. In fact, I noticed that the late metastatic potential of FST-interfered cells was impaired,

as revealed by the I.I.: 59% of sh FST-transplanted xenografts presented metastatic growths (Figure 31B), suggesting that FST silencing reduces cell extravasation, though at moderate extent. Consistently, I observed slight, yet statistically significant, differences in the AVG metastasis number (Figure 31C,D) and metastatic burden (Figure F) upon I.I. However, given the toxic effect that the silencing of FST seemed to exert on MDA-MB-231 cells, I cannot formally attribute these effects to a putative metastatic role of FST.

In conclusion, the FST metastasis-candidate gene was not successfully validated *in vivo* in the zebrafish model.

4.4.6 Summary

The zebrafish larval xenograft metastatic assay that I optimized was challenged with the purpose of metastasis-target validation *in vivo*, using a set of 6 candidate metastasis genes. These genes were identified through a transcriptional lineage tracing approach in mice. I demonstrated that the silencing via sh-mediated KD of 5 out of 6 of these genes (*i.e.* ANGPTL4, KCNQ1OT1, ITGB4, LY6E, IFI6) significantly reduced the metastatic potential of MDA-MB-231 cells *in vivo*. ANGPTL4 and KCNQ1OT1 were in parallel validated also in the murine model, obtaining consistent results with regard to PT growth and metastasis. In addition, I investigated the specific roles of each of these genes in the metastatic cascade. Table 3 reports a summary of the observed phenotypes and hypothesize a putative role for each gene in the multistep metastatic cascade based on the data collected so far.

Table 3 | Summary table of *in vivo* pro-metastatic genes validation in the zebrafish model.

| Gene | Metastasis incidence | Metastasis number | Metastasis size distribution | Metastatic burden | PT reduction | Possible effect |
|----------|-------------------------------|--------------------------|-----------------------------------|--------------------------|--------------|---|
| ANGPTL4 | S.I.: Non reduced | S.I.: Non reduced | S.I.: Homogeneous | S.I.: Non reduced | X | • Extravasation |
| | I.I.: Reduced | I.I.: Reduced | I.I.: Homogeneous | I.I.: Reduced | | |
| KCNQ1OT1 | S.I.: Non reduced | S.I.: Non reduced | S.I.: Homogeneous | S.I.: Non reduced | ✓ | • Extravasation • PT growth |
| | I.I.: Reduced | I.I.: Reduced | I.I.: Homogeneous | I.I.: Reduced | | |
| ITGB4 | S.I.: Reduced | S.I.: Reduced | S.I.: Homogeneous | S.I.: Reduced | ✓ | • Intravasation • Extravasation • Colonization • PT growth |
| | I.I.: Reduced | I.I.: Reduced | I.I.: Increased micro-mets | I.I.: Reduced | | |
| LY6E | S.I.: Reduced | S.I.: Reduced | S.I.: Homogeneous | S.I.: Reduced | ✓ | • Intravasation • PT growth |
| | I.I.: Slightly reduced | I.I.: Reduced | I.I.: Homogeneous | I.I.: Reduced | | |
| IFI6 | S.I.: Reduced | S.I.: Reduced | S.I.: Homogeneous | S.I.: Non reduced | X | • Intravasation • Colonization |
| | I.I.: Slightly Reduced | I.I.: Reduced | I.I.: Increased overt mets | I.I.: Reduced | | |

In detail, I showed that all the investigated genes, with the exception of ANGPTL4 and IFI6, impacted on PT growth. ANGPTL4 and KCNQ1OT1 were positioned in the step of extravasation, while LY6E and IFI6 in the intravasation phase, with the latter having a role also in colonization. On the contrary, multiple functions were assigned to ITGB4.

4.5 Zebrafish xenografts as a pre-clinical platform for drug sensitivity studies

4.5.1 Zebrafish *larvae* display drug sensitivity in a 3 day-long assay

To validate the potential of the described zebrafish assay as a fast and reliable screening-platform for BC drugs, I tested the efficacy of the standard chemotherapy agent Cisplatin in MDA-MB-231 xenografts. I first performed a 3 day-long dose-response assay to determine the maximum tolerated dose (MTD) at which at least 80% of the animals did not show mortality or abnormal phenotypes and I identified 23 μ M as the MTD for Cisplatin (Figure 32A). At 1 dpi I selected xenografts with comparable PT masses and without any signs of suffering and I started treatment for three consecutive days. A control group was left without treatment. At 4 dpi, I examined the animals to check survival and implantation potential and I fixed them for whole-mount immunofluorescence and confocal microscopy to evaluate proliferative index, cellularity, cell death and tumor volume. The experimental design is reported in Figure 32B.

Expectedly, the 23 μ M Cisplatin MTD did not affect survival of the xenografts ($85\pm 2.3\%$, $n=120$ vs. $80.3\pm 3.2\%$, $n=118$; $p=0.3007$), as compared to the control group, and slightly, yet not significantly, reduced implantation of MDA-MB-231 cells ($90.3\pm 2.6\%$, $n=108$ vs. $73\pm 8.6\%$, $n=89$; $p=0.1266$). In 3 days of treatment, Cisplatin treatment induced a significant reduction of proliferating cells (%Ki-67: $28.9\pm 2.3\%$ vs. $12.5\pm 1.3\%$; $p<0.0001$; Fig 32C-C'') and cellularity of the PT mass (278 cells ± 31 vs. 161 cells ± 22 ; $p<0.0040$; Fig 7F). Cisplatin also caused moderate apoptosis, as shown by immunofluorescence against activated-caspase 3 ($0.8\pm 0.1\%$ vs. $1.4\pm 0.3\%$; $p<0.0372$; Fig 32D-D''). However, despite its anti-proliferative and slightly pro-apoptotic effects, Cisplatin treatment did not induced a significant reduction of the tumor volume ($p=0.2169$; Fig 32E). Volumetric analysis was performed using a customized Fiji macro on z-stacks images of primary masses stained with anti-HLA antibody.

Together, these results show the feasibility of measuring drug response in fish, in terms of proliferation, cell death and tumor volume in a relatively short time-window (3 days) and in a large cohort of transplanted animals. The zebrafish xenografts might then provide a platform to evaluate fast *in vivo* responses to treatments in pre-clinical settings.

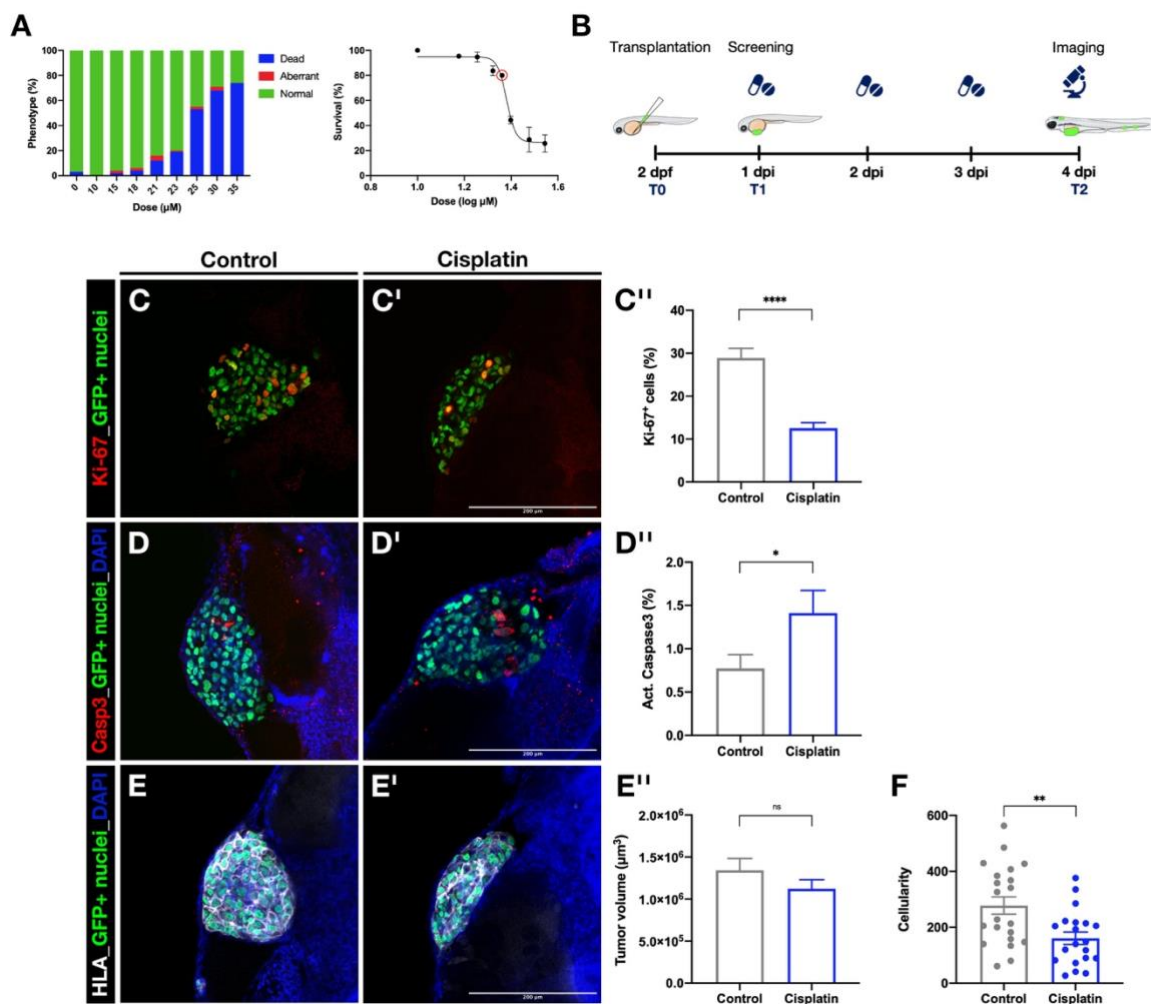


Figure 32 | Human MDA-MB-231 BC cells display chemosensitivity in just 3 days in the zebrafish host. 3 day-long dose-response assay for the definition of MTD and working concentration for CisPt. Results are expressed as the $\text{AVG} \pm \text{SEM}$ of at least three independent experiments using non-injected *larvae*; $n=90$ (A). Experimental design and timeline. Drug is replaced daily (B). Z-stacks confocal images of immunofluorescence staining at 4 dpi for Ki-67 and relative quantification using Arivis Vision 4D 3.5.0 software (C-C''); activated-caspase3 and relative quantification (D-D''); human-HLA and volumetric analysis. Volume was quantified using a Fiji/ImageJ customized pipeline (E-E''). Quantification of tumor primary mass cellularity using Arivis Vision 4D 3.5.0 software (F). All images have the same magnification and represent a single plane. Scale bar= 200 μm . Results are expressed as $\text{AVG} \pm \text{SEM}$ of at least three independent experiments. The number of xenografts analyzed are the following: %Ki-67 Ctrl $n=22$, CisPt $n=22$; % act.-caspase3 Ctrl $n=33$, CisPt $n=31$; volume Ctrl $n=39$, CisPt $n=38$; cellularity Ctrl $n=21$, CisPt $n=20$. Statistical analysis: *t* test. * $p < 0.05$, ** $p < 0.01$, **** $p < 0.0001$, ns= not significant.

4.5.2. *In vivo* treatment with autophagy-inducer drugs reverts resistance of MDA-MB-231 BC to Paclitaxel

I then evaluated the feasibility of combined treatments, testing the *in vivo* effects of a traditional chemotherapeutic drug for BC, Paclitaxel, administered with autophagy-inducing agents to MDA-MB-231 zebrafish xenografts (in collaboration with Dr. Salvatore Pece at the Department of Experimental Oncology of European Institute of Oncology).

Paclitaxel is a first-line antineoplastic drug for TNBC [Isakoff, 2010]. Emergence of taxane resistance is however a major clinical problem, which imposes the optimization of novel therapeutic approaches to sensitize TNBCs to chemotherapy. One putative strategy is stimulation of the autophagic response. Autophagy is a survival pathway that eliminates damaged organelles and cytotoxic metabolites from cells and it is activated in response to shortage of nutrients and growth signals [Kaur and Debnath, 2015]. Tumors take advantage of autophagy to survive metabolic stress, though excessive autophagy activation may lead to cell death and senescence [White, 2012]. Expression of the phosphatase PTEN by cancer cells is necessary for the activation of the autophagic response. Thus, we tested whether inhibition of the AKT-mTOR nutrient-sensing pathway in nutrient-rich conditions might revert resistance to Paclitaxel. To this end, we used two agents widely used in clinical trials [Galluzzi *et al.*, 2017]: the LY294002 PI3K-inhibitor and the Everolimus mTORC1-inhibitor on MDA-MB-231 cells, that are PTEN-proficient.

First, we confirmed that MDA-MB-231 cells are resistant to taxane treatment, conserving their tumorigenic ability *in vivo* when transplanted in zebrafish *larvae* (Figure 33A'). In fact, despite a slight decrease of tumor volume ($p=0.0232$; Figure 33B) and cellularity ($p=0.005$; Figure 33C), Paclitaxel treatment did not significantly impair PT growth. Autophagy-stimulating drugs alone efficiently reduced tumor size and cellularity (volume, $p=0.0003$; cellularity, $p<0.0001$; Figure 33A'',B,C) and synergized when used in combination with Paclitaxel (Figure 33A'''), leading to a block of tumor growth (volume, $p<0.0001$; cellularity, $p<0.0001$; Figure 33B,C). Treatment with LY294002 and Everolimus efficiently induced autophagy in PTs, as demonstrated by the immunofluorescent staining of the LC3, autophagosome marker (Figure 33D) and, in presence of chemotherapy, further increased senescence (Figure 33D) and apoptosis ($p=0.01$; Figure 33D,E), accompanied by a block of proliferation ($p=0.0012$; Figure 33D,F).

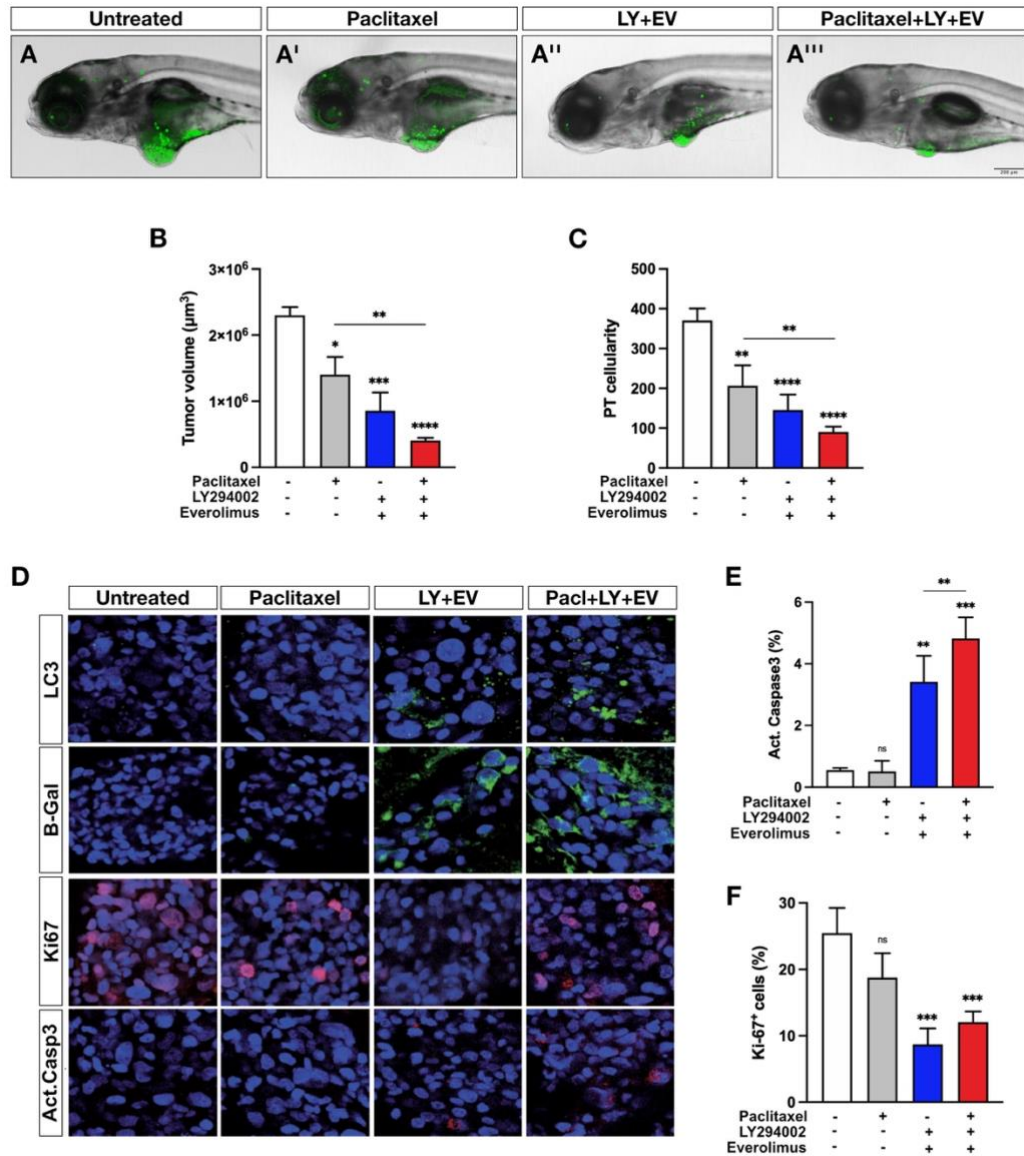


Figure 33 | Autophagy-stimulating treatments enhance TNBCs sensitivity to Paclitaxel. Z-stacks confocal images of live 4 dpi xenografts transplanted with MDA-MB-231-GFP⁺ cells (n=59) (A) and treated with Paclitaxel (n=58) (A'), LY294002+Everolimus (n=55) (A'') and the combination of the three drugs (n=47) (A'''). Scale bar= 200 μm . *Ex vivo* analysis of PT volume (B) and cellularity (C) upon treatments. Z-stacks confocal images of immunofluorescence staining of 4 dpi PTs for LC3, β Galactosidase, Ki67 and activated Caspase 3, upon treatments. All images have the same magnification and represent a single plane. Human cell nuclei are depicted in blue (D). *Ex vivo* quantification of apoptosis (E) and proliferation (F). Results are expressed as the $\text{AVG} \pm \text{SEM}$. Image analysis were performed with Fiji/ImageJ and Arivis Vision 4D 3.5.0 software. Statistical analysis: one-way ANOVA followed by Tuckey's *post-hoc* test. * $p < 0.05$; ** $p < 0.01$; *** $p < 0.001$; **** $p < 0.0001$; ns= not significant.

In conclusion, I preliminary proved the value of my zebrafish xenograft-platform to test novel pharmacological treatments *in vivo*. Specifically, these data demonstrate that Paclitaxel alone is inefficient against MDA-MB-231 BC cells in fish, and that the pharmacological activation of autophagy renders cancer cells more susceptible to standard chemotherapy, suggesting that autophagy stimulation is a valuable strategy to overcome taxane-refractoriness of TNBCs.

5. Discussion

In the last decades, many efforts have been put into the establishment of technologies and model systems to mimic individual patient cancer behavior and drug responses, as well as to dissect the process of metastasis, which remains the major determinant of cancer-related mortality [Costa *et al.*, 2020a; Khanna and Hunter, 2005]. This is especially true for breast cancer (BC), which is characterized by a high level of inter-patient heterogeneity, with therapy-resistant metastatic TNBC representing the deadliest subtype [Torre *et al.*, 2017; Siegel, Miller and Jemal, 2020]. Moreover, our growing understanding of inter- and intratumor heterogeneity suggests that metastatic potential may vary among patients and among different cells within the same tumor [Lüönd, Tiede and Christofori, 2021].

Many *in vitro* models have been developed to shed light on the cellular dynamics and molecular mechanisms involved in specific events of cancer and metastasis progression, such as cell migration and adhesion [Malandrino, Kamm and Moeendabary, 2018]. However, they failed to fully reproduce interactions with the TME, thus suffering of physiological relevance. On the other hand, *in vivo* approaches, and in particular the expansion of human cancer cells in an immune-permissive host (xenotransplantation, XT), are needed to reconstruct human cancer complexity. The gold standard for *in vivo* cancer research is mouse XT [Malaney, Nicosia and Davé, 2014], which suffers, however, of several inherent disadvantages, including: the long latency period for cancer cell engraftment and expansion; the impossibility to make observations over a significantly high number of individuals and a relatively high cost and resource-intensive maintenance. These limitations become even more stringent when mPDXs are used as personalized medicine models. Furthermore, the real-time tracking and quantification of tumor spreading and metastasis is not feasible in the mouse, due to lack of resolution of current live imaging protocols [Ellenbroek and van Rheenen, 2014]. Imaging of micro-metastases in the thick mouse tissues usually requires animal sacrifice and *ex vivo* analyses, thus preventing investigation of seeding and colonization. On the contrary, zebrafish at a larval stage, possesses many favorable traits that make it an extraordinary transplant recipient, allowing to overcome most of the limitations of the murine model. Particularly, zebrafish xenografts proved to have enough sensitivity to discriminate *in vivo* functional cancer heterogeneity in terms of engraftment, proliferation, response to therapy and metastatic potential [Fior *et al.*, 2017]. A broad introduction to the zebrafish xenograft model and an extensive description of all its advantages is reported in paragraph 3.3 of chapter 2.

Albeit many advances have been made since the first pioneering studies on zebrafish xenografts, to date no full consensus has been reached in literature about cell labeling, site of injection, incubation temperature and duration of the assay. Reported zebrafish XT protocols are frequently not standardized and adapted to specific experimental questions or cancer types. This lack of harmonized protocols and common analytic tools among zebrafish laboratories might affect reproducibility, representing a limitation to the use of zebrafish xenograft as a cancer *in vivo* pre-clinical platform and, in particular, as a patient “avatar” model [Costa *et al.*, 2020a]. Rapid, efficient and non-invasive imaging methods to visualize the metastatic process of human tumors in zebrafish have already been reported by others [Follain *et al.*, 2018b; Paul *et al.*, 2019; Asokan *et al.*, 2020] but a quantitative and univocal dissection of all the steps of the metastatic cascade was still lacking.

In this thesis, I described the development of a robust 4-day-long zebrafish xenograft assay to investigate crucial hallmarks of BC, using the metastatic MDA-MB-231 line as cellular model. Although the technical dexterity required for micro-transplantation in 2 dpf fish (specifically targeting sites like PVS and DoC to respectively obtain subcutaneous and intravenous injection) can be challenging, I successfully acquired this skill and I set up *in vivo* and *ex vivo* high-resolution imaging approaches to evaluate several tumor traits, from PT growth to metastasis, as well as drug response. Furthermore, this study provides for the first time the systematic usage of zebrafish *larvae* as *in vivo* tool to validate the role of a relatively high number of novel candidate BC pro-metastatic genes and map their stage-specific functions in the metastatic cascade, in an extremely short time-window. The set of genes exploited in this study were derived from a lineage tracing experiment conducted on MDA-MB-231 cells transplanted in nude mice, that enabled to simultaneously monitor clonal evolution of BC cells during metastatization and to unravel pro-metastatic clones transcriptional profiles at single-cell level.

Zebrafish model optimization required the use of a proper negative control, thus, in parallel with MDA-MB-231 cells, I exploited the non-tumorigenic MCF10A mammary epithelial cell line. First, I scored different implantation potentials for the two different cell lines, whose injection, however, did not differentially affect *larvae* survival. Implantation potential measures the engraftment rate as the percentage of xenografts who originate a PT at the injection site over 4 days and, according to my data, unambiguously attests the tumorigenic properties of the grafted cells: MCF10A cells, in fact, do not form any detectable tumor mass and injected cells almost totally disappear from the PVS as early as 1 dpi. Moreover, death of the few disseminated MCF10A cells is clearly evident from the apoptotic appearance of their nuclei. Nevertheless, published work [Fior *et al.*, 2017] demonstrated that, though most cancer cells positively engraft in zebrafish, some do not and

are progressively eliminated from the host. Similarly, I observed that different mammary tumor subtypes display different implantation potentials: human T47D luminal A non-metastatic BC cells, for instance, engraft in only 40% of xenografts (data not shown), while MDA-MB-231 cells form tumors in >80% of the cases. This suggests that the capacity of transplanted cancer cells to implant does not merely depend on their tumorigenic potential but from others intrinsic or microenvironmental factors, raising the question about what implantation potential actually measures.

According to my findings on MDA-MB-231 cell line, the total number of cells that compose the grafted PT at 4 dpi (211 ± 15 ; $AVG \pm SEM$) is significantly lower respect to the number of cells introduced in the *larva* at 2 dpf (~500 cells), suggesting that a part of the transplanted cells either died or underwent innate immune clearance. Alternatively, it is possible that tumor implantation in the zebrafish host might be sustained by cancer cells with self-renewal capacity, the so called cancer stem cells (CSCs).

Since the amount of cells transplanted in each *larva* is particularly low and animals are followed for a short period of time, optimal cell viability is required for successful XT. In fact, to preserve viability, cell preparations with less than 80% of living cells were discarded prior to injection and the amount of time between cell harvest and XT was strictly limited to the duration of the micro-injection procedure. Being sure of the optimal quality of the sample, it is likely that cell death occurs early after transplantation since in 4 dpi PTs I detected only 0.75% of apoptosis (cells expressing activated-caspase3). Therefore, a time course investigation of basal cell death over tumor growth is required to understand when cell elimination arises. Interestingly, the silencing of the gene FST – one of the putative metastasis targets explored in this study – seems to impact on MDA-MB-231 cell viability, preventing the formation of an overt primary mass, herein affecting implantation potential.

As extensively demonstrated by limiting dilution experiments in mice, only a restricted subset of cells endowed with stem properties is able to initiate tumorigenesis when transplanted in a compatible recipient. Similarly to normal proliferative tissues, the expansion of a tumor is fueled by CSCs, whereas the tumor bulk is composed by both rapidly proliferating and post-mitotic differentiated cells, neither of these able to self-renew [Clevers *et al.*, 2011]. Therefore, cancer cell implantation in zebrafish *larvae* might be – at least partially – stem cell-dependent, recapitulating the functional heterogeneity of human tumors. Strikingly, this hypothesis is sustained by experimental evidence. Tumor engraftment in adult zebrafish, for instance, depends on self-renewing cancer cells and an accurate method to quantify their frequency by limiting dilution transplantation assay in syngeneic fish, using primary zebrafish leukemic cells, have been established [Blackburn, Liu and Langenau, 2011]. MDA-MB-231 XT experiments performed in mice by our laboratory, measured a

frequency of CSCs for this cell line around 1:30/1:50. Considering that, in my experiments, each *larva* received ~500 viable cells and assuming that only CSCs sustained tumor growth, this finding is consistent with the cellularity of PTs at 4 dpi. However, transplantation of decreasing doses of MDA-MB-231 cells in 2 dpf *larvae* and assessment of PT implantation and size is required to confirm my observations. In addition, I failed to obtain xenografts from primary BC cells derived from patients specimens (PDX), with cells unable to survive and grow in zebrafish till 4 days: being the CSC frequency of the mammary tumor primary samples used in my experiment extremely low, 500 cells per *larva* were not sufficient to initiate oncogenic growth. On the contrary – as part of a collaboration with an independent group of the Department of Experimental Oncology of the European Institute of Oncology – I had the opportunity to challenge the zebrafish model with other tumor types, transplanting primary glioblastoma cells previously expanded in culture as neurospheres, and observing 100% of engraftment (data not shown). Indeed, the neurosphere culture system enriches the glioblastoma cell preparation of tumor initiating cells with self-renewal properties, supporting the hypothesis of CSC-dependency of cell engraftment in the zebrafish host. Likewise, literature data demonstrate that cells grown in mammospheres from BC cell lines form tumor masses and migrate in zebrafish with a significantly higher frequency respect to the same cells cultured in monolayer [Eguiara *et al.*, 2011]. I also observed that the knock-down of the epigenetic regulator KMT2D, whose silencing is involved in cell reprogramming, enhances implantation potential of the poorly engrafting T47D BC cell line from 40% to 78% (data not shown). The fact remains that, being the time-window in which tumor formation is followed extremely restricted, it is possible to observe also the contribution given by the tumor bulk, as suggested by the high proliferative index of MDA-MB-231 tumors at 1 dpi.

Extrinsic factors deriving from TME might influence tumor implantation/rejection in zebrafish *larvae*. It has been demonstrated that, after going through the process of immunoediting, the implantation capacity of cancer cells in immunocompetent recipients increases, implying that tumor engraftment capacity reflects the immunogenic state of the cells [Schreiber, Old and Smyth, 2011]. Zebrafish *larvae* are not capable of adaptive immunity at this stage of development – thereby allowing foreign cells engraftment in most cases – but present a fully mature innate immune system, with competent macrophages, neutrophils and NK-like cells [Lam *et al.*, 2004; Trede *et al.*, 2004]. According to Póvoa and colleagues, the innate immunity strongly contributes to PT engraftment, either through active cancer cells elimination or, at the contrary, immune-shaping cells toward tumorigenesis [Póvoa *et al.*, 2021]. The authors state that tumors with the higher degree of

immune cell recruitment also show poor engraftment, whereas tumors that recruit fewer immune cells engraft efficiently and grow.

MDA-MB-231 tumor masses grafted in zebrafish recipients recapitulate the same morphological, proliferative and immunohistochemical profile of MDA-MB-231 mouse xenografts, both resembling the typical features described for this cell line [Chavez, Garimella and Lipkowitz, 2010; Subik *et al.*, 2010]. This evidence further validates the use of zebrafish as a complementary xenograft model to mouse: no remarkable differences between fish and mammals have been observed, supporting the possibility to translate and compare findings between the two model organisms, also in case of transplantation of patient-derived cells. I also applied *ex vivo* imaging techniques to evaluate proliferation, cellularity, volume and apoptosis of PT masses, both in unperturbed conditions and in response to chemotherapy and targeted therapies. The image analysis protocols that I set up are particularly precise and reliable, since they allow to specifically count human GFP⁺ nuclei in multi-stack confocal images and evaluate at which extent they express specific markers. On the contrary, numerous zebrafish xenograft assays still express tumor burden indirectly as a measure of fluorescence intensity [Chen *et al.*, 2020; Usai *et al.*, 2020], estimating cell number after the sacrifice of the fish by tumor dissociation [Wu *et al.*, 2017] or by quantitative PCR assay targeting human housekeeping genes [Pruvot *et al.*, 2011]. *Ex vivo* analyses revealed that ~30% of MDA-MB-231 cells express Ki67 in 4 dpi zebrafish xenograft PTs, reflecting the relatively slow proliferating nature of MDA-MB-231 tumors *in vivo* in the mouse model. Moreover, proliferative index of zebrafish PTs might be further slowed down as a consequence of the non-physiological temperature for mammalian cells (34°C) at which xenografts are kept along the experimental time-window.

In this study I described two methods to visualize and – most importantly quantify – metastatic behavior of BC cells in a short time window. Despite the large usage of lipophilic cell dyes for cell tracking, I decided to label cancer cells by engineering them with a fluorescent reporter gene, in order to have a strong long-term nuclear signal. This gave me the possibility to easily track and quantify disseminated cells (at both single-cell and cluster level) in different districts of the *larva* under the microscope. As expected, MDA-MB-231 and MCF10A cells dramatically differ in their metastatic potential, with MDA-MB-231 metastatic spreading achieved as early as 1 dpi and sustained till the end of the assay. Much lower numbers of non-malignant breast epithelial cells disseminate and survived over time in the head, trunk or tail region of the *larva* compared to BC, consistently with already published results [Ren *et al.*, 2017a, Asokan *et al.*, 2020].

The two modalities of injection that I optimized differentiate the readout: early events of the metastatic cascade, such as local invasion, intravasation and hematogenous

dissemination, are recapitulated by injecting cancer cells in the PVS (considered the primary site), whereas late metastatic events are simulated introducing cancer cells into the circulatory system. At distant sites (mainly the CHT in the caudal region) metastatic cancer cells accumulate in the capillary beds, extravasate forming peri-vascular metastases and undergo single-cell invasion of caudal muscles or of the collagen matrix-rich tail fin.

CHT is the site of larval hematopoiesis and resembles the mammalian bone marrow, a well-known site of metastatic cell homing [Shiozawa *et al.*, 2015]. The non-random pattern of MDA-MB-231 cell metastasis in the hemopoietic niche is driven by both vessel topography, who causes early passive arrest of cells in the CHT venous plexus, and autocrine and paracrine factors that specifically mediate extravasation in this site [Tulotta *et al.*, 2016; Paul *et al.*, 2019]. Similarly to tumor cells seeded in the human bone marrow microenvironment, it has been reported that cancer cells that home in the zebrafish CHT highly express genes that regulate IL-6 pathway, cell adhesion and angiogenesis [Sacco *et al.*, 2016]. Recent findings also showed that zebrafish hemopoietic niche induces CSC traits and tumor cell response to larval CHT signals, recapitulating the response to mammalian bone marrow osteoblasts and mesenchymal stem cells [Chen *et al.*, 2020a,b], indicating a functional interaction between human cancer cells and zebrafish microenvironment, leading to enhanced cell plasticity and metastatic progression.

The peculiar characteristics of zebrafish *larvae*, mainly their small dimensions, optical transparency and easy manipulation, combined with the use of a fish strain with fluorescent vasculature, allowed to dissect the entire BC metastatic cascade and to assign a quantitative score to distinct metastatic phenotypes at both 1 and 4 dpi (see Table 1, paragraph 4.2.9). Being zebrafish an extremely prolific species, the analyses can be conducted on a large cohort of fish, derived from the mating of few adult couples, easily achieving powerful statistics.

Among the optimized analytic parameters, the incidence of metastasis measures the efficiency of metastasis formation in the CHT, reflecting the capacity of cells to go through the entire cascade or only the later phases, according to the site of injection. The number of metastatic growths (extravasated clusters of more than 5 cells) and their variation over time express the extent of metastasis seeding and formation. Thanks to its unrivalled *in vivo* optical resolution, zebrafish also offers the possibility to detect single extravasated cells – also known as disseminated tumor cells (DTCs) – in the peri-vascular niche, that is considered a reservoir of dormant metastatic cells in mammals. These disseminated indolent cells are the main cause of metastatic relapse in patients and it is reported for BC that DTCs, in mouse models of metastasis, reside on microvasculature of lungs, bone marrow and brain, where endothelial-derived factors sustain quiescence [Ghajar *et al.*, 2013]. Thus, the

quantification of peri-vascular single extravasated cells in the zebrafish model would be useful in order to obtain a measure of the portion of dormant metastatic cells present at distant sites. As observed in my experimental setting and as previously reported [Drabsch *et al.*, 2013; Ren *et al.*, 2017a], metastatic MDA-MB-231 cells exhibit single-cell invasive phenotype in the tail fin. However, further time-lapse imaging experiments on living animals are required to obtain a precise dissection of extravasation and invasion dynamics in the CHT peri-vascular parenchyma. In particular, it would be of interest to understand whether micro-metastases derive from the expansion of a single extravasated cell or from multiple independently extravasated cells that associate to form a metastatic cluster. A fine understanding of these mechanisms is indispensable to obtain a precise definition of the frequency of metastasis initiating cells (MICs).

Frequency of MICs gives a preliminary hint of how many cells in a specific tumor are endowed with metastatic properties, normalizing the number of metastases over the total number of cells composing the PT. Nevertheless, it is important to notice that this index assumes PT cellularity as a constant parameter, not taking into account that PT could grow over time – releasing more and more cells from its surface – or, on the contrary, could go through apoptosis. Therefore, for a more precise calculation of MIC frequency, it is necessary to describe the dynamics of PT growth between the time of injection and 4 dpi.

Metastatic colonization is assessed quantifying quiescent or expanding cells, based on numbers of cell per metastasis and their proliferative index. Following the same fish along the entire duration of the assay, without the need to sacrifice it, enables a longitudinal examination of the metastatic process. This kind of analysis – repeated for a large number of animals in the same experiment – aims to portray the metastatic evolution of a specific tumor. MDA-MB-231 metastases grow both in number and cellularity in zebrafish xenografts between 1 and 4 dpi, indicating both the onset of new metastatic foci and outgrowth of already existing ones. However, to portray in real-time these events, I am planning to perform time-lapse microscopy of the CHT regions of *larvae* transplanted with MDA-MB-231 cells engineered with the FUCCI cell cycle and division fluorescent reporter. This experimental setting enables to assess kinetics and proliferative properties of circulating, disseminated and metastatic cells at the same time. A similar approach was already used in zebrafish xenografts in order to investigate in real-time the cellular state of rhabdomyosarcoma cells transplanted in adult animals upon anti-cancer therapies [Yan *et al.*, 2019].

Finally, I reported for the first time a quantification of the grade of metastatic progression in the zebrafish host, defining a metastatic-burden index that takes into consideration both number and size of metastases. Metastatic burden assigns a score for each

fish basing on the presence of micro-metastatic foci (5-10 cells), actively expanding metastases (10-20 cells) and overt metastatic lesions (>20 cells), depicting the “clinical” severity of metastatic disease.

Emerging evidence sustains that metastatic progression depends more on phenotypic than genotypic traits. Our laboratory has recently investigated the specific transcriptional programs that characterize pro-metastatic BC cells (*i.e.* the cells that detach from the PT and outgrow at distant sites), applying a lineage tracing strategy coupled to scRNAseq. Strikingly, we observed that pro-metastatic cells actually display peculiar transcriptional differences respect to non-metastatic ones. We found that cell migration was linked to adaptive phenotypes, namely ECM deposition and type-1 IFN response, in turn mediated by stress signals, particularly hypoxia and ER stress. Consistently, hypoxia was already shown to stimulate ECM deposition, via the upregulation of matrix components [Gilkes, Semenza and Wirtz, 2014]. Notably, both hypoxia [Lee *et al.*, 2009] and matrix deposition [Chapman *et al.*, 2014] are known inducers of tumor dissemination and metastasis in zebrafish xenograft models of BC and melanoma. ER stress was also shown to activate type-1 IFN response in different experimental disease models [Sprooten and Garg, 2020], however, its role in metastatic progression is still controversial.

In this scenario, I tested the functions of the 6 top upregulated genes in the pro-metastatic clones – namely ANGPTL4, KCNQ1OT1, ITGB4, LY6E, IFI6, FST – performing a reverse genetics approach on MDA-MB-231 cells and exploiting the rapid and quantitative zebrafish xenograft platform recently optimized, aiming to demonstrate whether each of these genes have an impact on the metastatic outcome *in vivo*. Remarkably, my findings replicated and confirmed the previously published pro-metastatic function of ANGPTL4 [Padua *et al.*, 2008] and showed a previously unknown role for 4 out of the remaining 5 genes (*i.e.* KCNQ1OT1, ITGB4, LY6E, IFI6) in fostering BC metastatic spreading. The results I obtained in zebrafish are highly consistent with what observed in parallel in mouse, ultimately strengthening the validity of zebrafish xenograft larval model for the study of genetic determinants of metastatic progression in human tumors. *In vivo* validation experiments also strongly correlate with the analysis of over-represented pathways in the pro-metastatic clones. Indeed, I successfully validated two genes (*i.e.*, ANGPTL4 and ITGB4) involved in ECM deposition and migration and other two (*i.e.*, LY6E and IFI6) implied in type-I IFN response. Furthermore, according to clinical data, patients who overexpress this set of genes display a significant worse prognosis in terms of relapse-free, metastasis-free and overall survival, suggesting that MDA-MB-231 cells characterized by the expression of these genes play a major role in the clinical progression of BC.

This study proposes the XT in zebrafish *larvae* as a system to map specific functions of candidate genes in BC metastatic cascade. Genetic determinants of metastasis can be grouped into different classes, according to the metastatic phase they are involved in [Nguyen, Bos and Massagué, 2009]. Genes that prime transformed cells to invade locally, intravasate and disperse in the circulation – mainly through the promotion of EMT, matrix degradation, motility, angiogenesis and immune evasion – are defined metastasis initiation genes. According to the findings collected in zebrafish, I hypothesize that among the investigated set of genes, LY6E and IFI6 might be included in the above mentioned category, as their loss strongly impairs metastatic potential of subcutaneously injected cancer cells, whereas a moderate reduction was observed for cells injected in the bloodstream. However, to precisely tackle this issue, the quantification of the amount of cells that leave the PT site and enter the circulation early after subcutaneous injection would be necessary.

A second category of metastatic genes – defined metastasis progression genes – are specialized in promoting extravasation and survival in the foreign parenchyma, priming infiltration in distant organs. ANGPTL4 falls into this category, as demonstrated by my findings and previously by others. KCNQ1OT1 also seems to be involved in late metastatic phases, besides showing an effect on PT growth, herein suggesting different roles in primary and distant sites.

The boundaries between metastasis initiation and progression genes are not necessarily rigid: a gene known for regulating one event might also participate in another one. This could be the case of ITGB4, since its silencing impacts on both early and late metastatic potential. As a matter of fact, many oncogenic roles for ITGB4 has been already reported, including involvement in EMT, matrix degradation and cell motility [Yang *et al.*, 2021].

Notably, in none of the cases BC metastatic phenotype was totally abrogated. For all tested genes, we scored a significant reduction of metastatic potential but animals still displayed a certain level of distant organ infiltration, thus suggesting that MDA-MB-231 metastatic progression cannot be completely abolished by targeting a single vulnerability of the metastatic cascade.

Contemporary to the study of metastatic phenotypes, I investigated *in situ* BC cell growth. The silencing of KCNQ1OT1, ITGB4 and LY6E affected PT size, with the last two also reducing MDA-MB-231 engraftment by 15-20%, thus suggesting a role for these genes also in local BC progression. On the contrary, ANGPTL4 and IFI6 only exerted a role in the metastatic cascade, without providing any discernable benefit to PT implantation and expansion. Interestingly, LY6E gene is reported to be required for tumor immune escape, limiting NK cell activation [AlHossiny *et al.*, 2016], hence suggesting that the reduced

engraftment of LY6E KD MDA-MB-231 cells in the zebrafish model might be due to the action of innate immunity players. Further experiments, involving zebrafish transgenic lines carrying fluorescent immune cells, are required to identify the exact role of host immune cells in tumor engraftment/clearance. Reduced implantation and growth of LY6E-deficient BC cells also seems to be related to CSCs function. In fact, the murine functional homolog of human LY6E is the stem cell antigen-1 gene (Sca-1), which encodes a protein recognized as both normal and cancer SC marker [Holmes and Stanford, 2007; Grange *et al.*, 2008]. Moreover, it has been demonstrated that human LY6E silencing decreases the mRNA expression of well-known stem cell genes in BC cells, such as Nanog, PSCA and CD34 [AlHossiny *et al.*, 2016]. Likewise, decreased implantation potential of ITGB4 KD cells might be linked to a reduction of CSCs. Indeed, ITGB4 has been previously described as a basal epithelial marker overexpressed in a CSC-enriched population of tumor cells with mesenchymal phenotype in TNBC and other carcinomas [Bierie *et al.*, 2017]. In addition, the reduced size of ITGB4 KD tumors does not seem to be a consequence of impaired proliferation (Ki67 index), contrary to what observed for KCNQ10T1.

Overall, my findings demonstrate that the genes upregulated in MDA-MB-231 pro-metastatic clones possess an effective role in determining the metastatic outcome *in vivo*. Zebrafish xenograft platform proved to be an invaluable tool for the quantitative dissection of metastatic adaptive phenotypes of human cancer cells, perfectly fitting into the current effort to establish rapid, robust and informative platforms to study metastatic gene functions. Hence, this study contributes to the definition of critical targets to halt life-threatening metastatic dissemination, leading to the future optimization of specific anti-metastatic treatments, which are still very scarce in the clinical practice

Therefore, another future application of my zebrafish larval xenograft platform could be the evaluation of the effects of pharmacological intervention on BC progression. With regard to this, I set up a drug testing protocol on zebrafish xenografts that enable to discriminate fast and strong responses to both standard chemotherapeutic and targeted agents, alone and in combination, in just 3 days. While my preliminary experiments focus more on the impact of anticancer drugs on BC *in situ* growth, the effect of potential anti-metastatic drugs can be assessed taking advantage of the analytic tools optimized to describe the metastatic cascade.

Several future goals can follow to this study. For instance, we plan to optimize the zebrafish xenograft platform to isolate grafted human cancer cells from PTs, circulation and metastases for single-cell transcriptomic approaches. In this respect, I have already generated few preliminary data that demonstrate the feasibility to retrieve viable cancer cells from xenografts, performing FACS-sorting isolation of human MDA-MB-231-GFP⁺ cells

from cellular suspensions of micro-dissected larval cephalic and caudal portions. Exploiting this strategy, we aim to explore the different cancer cell phenotypic states associated with peculiar stages of BC progression.

6. References

1. Ablain J, Xu M, [...] and Yeh I. 2018. Human tumor genomics and zebrafish modeling identify *SPRED1* loss as a driver of mucosal melanoma. *Science* 362(6418):1055-1060.
2. Adamson B, Norman TM, [...] and Weissman JS. 2016. A multiplexed single-cell CRISPR screening platform enables systematic dissection of the unfolded protein response. *Cell* 167(7):1867-1882.
3. Aftimos P, Oliveira M, [...] and Piccart MJ. 2021. Genomic and transcriptomic analyses of breast cancer primaries and matched metastases in AURORA, the Breast International Group (BIG) molecular screening initiative. *Cancer Discov* 1647.2020.
4. AlHossiny M, Luo L, [...] and Upadhyay G. 2016. Ly6E/K signaling to TGF β promotes breast cancer progression, immune escape, and drug resistance. *Cancer Res* 76(11):3376-86.
5. Ashton GH, Sorelli P, [...] and McGrath JA. 2001. Alpha 6 beta 4 integrin abnormalities in junctional epidermolysis bullosa with pyloric atresia. *Br J Dermatol* 144(2):408-14.
6. Asokan N, Daetwyler S, [...] and Bornhäuser M. 2020. Long-term in vivo imaging reveals tumor-specific dissemination and captures host tumor interaction in zebrafish xenografts. *Sci Rep* 10(1):13254.
7. Banasavadi-Siddegowda YK, Welker AM, [...] and Kaur B. 2018. PRMT5 as a druggable target for glioblastoma therapy. *Neuro Oncol* 20(6):753-763.
8. Berghmans S, Murphey RD, [...] and Look AT. 2005. *tp53* mutant zebrafish develop malignant peripheral nerve sheath tumors. *Proc Natl Acad Sci U S A* 11;102(2):407-12.
9. Berns K, Sonnenblick A, [...] and Bernards R. 2016. Loss of ARID1A activates ANXA1, which serves as a predictive biomarker for trastuzumab resistance. *Clin Cancer Res* 22(21):5238-5248.
10. Bertotti A, Migliardi G, [...] and Trusolino L. 2011. A molecularly annotated platform of patient-derived xenografts ("xenopatients") identifies HER2 as an effective therapeutic target in cetuximab-resistant colorectal cancer. *Cancer Discov* 1(6):508-23.
11. Bibby MC. 2004. Orthotopic models of cancer for preclinical drug evaluation: advantages and disadvantages. *Eur J Cancer* 40(6):852-7.
12. Bierie B, Pierce SE, [...] and Weinberg RA. 2017. Integrin- β 4 identifies cancer stem cell-enriched populations of partially mesenchymal carcinoma cells. *Proc Natl Acad Sci U S A* 114(12):E2337-E2346.
13. Blackburn JS, Liu S and Langenau DM. 2011. Quantifying the frequency of tumor-propagating cells using limiting dilution cell transplantation in syngeneic zebrafish. *J Vis Exp* (53):e2790.
14. Britto DD, Wyroba B, [...] and Astin JW. 2018. Macrophages enhance Vegfa-driven angiogenesis in an embryonic zebrafish tumour xenograft model. *Dis Model Mech* 11(12):dmm035998.
15. Brown HK, Schiavone K, [...] and Chico TJA. 2017. Zebrafish xenograft models of cancer and metastasis for drug discovery. *Expert Opinion on Drug Discovery* 12:4, 379-389.
16. Cam M, Charan M, [...] and Cam H. 2020 Δ Np73/ETS2 complex drives glioblastoma pathogenesis — targeting downstream mediators by rebastinib prolongs survival in preclinical models of glioblastoma. *Neuro-Oncology* Volume 22, Issue 3, Pages 345–356.

17. Canella A, Welker AM, [...] and Pudukkoti VK. 2017. Efficacy of onalespib, a long-acting second-generation HSP90 inhibitor, as a single agent and in combination with temozolomide against malignant gliomas. *Clin Cancer Res* 23(20):6215-6226.
18. Ceol CJ, Houvras Y, [...] and Zon LI. 2011. The histone methyltransferase SETDB1 is recurrently amplified in melanoma and accelerates its onset. *Nature* 471(7339):513-7..
19. Chaffer CL and Weinberg RA. 2011. A perspective on cancer cell metastasis. *Science* 25;331(6024):1559-64.
20. Chambers AF, Groom AC and MacDonald IC. 2002. Dissemination and growth of cancer cells in metastatic sites. *Nat Rev Cancer* 2(8):563-72.
21. Chapman A, Fernandez del Ama L, [...] and Hurlstone A. 2014. Heterogeneous tumor subpopulations cooperate to drive invasion. *Cell Rep* 8(3):688-95.
22. Chavez KJ, Garimella SV, Lipkowitz S. 2010. Triple negative breast cancer cell lines: one tool in the search for better treatment of triple negative breast cancer. *Breast Dis* 32(1-2):35-48.
23. Chen L, De Menna M, [...] and Snaar-Jagalska BE. 2020. A NF- κ B-Activin A signaling axis enhances prostate cancer metastasis. *Oncogene* 39(8):1634-1651 – a.
24. Chen L, Boleslaw Olszewski M, Kruithof-de Julio M, and Snaar-Jagalska BE. 2020. Zebrafish microenvironment elevates EMT and CSC-like phenotype of engrafted prostate cancer cells. *Cells* 9(4):797 – b.
25. Chen X, Wang J, [...] and Cao Y. 2015. Invasiveness and metastasis of retinoblastoma in an orthotopic zebrafish tumor model. *Sci Rep* 5:10351.
26. Cheriya V, Glaser KB, [...] and Borden EC. 2007. G1P3, an IFN-induced survival factor, antagonizes TRAIL-induced apoptosis in human myeloma cells. *J Clin Invest* 117(10):3107-17.
27. Cheriya V, Kaur J, [...] and Gaddipati L. 2018. G1P3 (IFI6), a mitochondrial localised antiapoptotic protein, promotes metastatic potential of breast cancer cells through mtROS. *Br J Cancer* 119(1):52-64.
28. Cheriya V, Kuhns MA, [...] and Borden EC. 2012. G1P3, an interferon- and estrogen-induced survival protein contributes to hyperplasia, tamoxifen resistance and poor outcomes in breast cancer. *Oncogene* 31(17):2222-36.
29. Clevers H. 2011. The cancer stem cell: premises, promises and challenges. *Nat Med* 17(3):313-9.
30. Costa B, Estrada MF, Mendes RV and Fior R. 2020. Zebrafish avatars towards personalized medicine – A comparative review between avatar models. *Cells* 9(2):293 – a.
31. Costa B, Ferreira S, [...] and Fior R. 2020. Developments in zebrafish avatars as radiotherapy sensitivity reporters - towards personalized medicine. *EBioMedicine* 51:102578 – b.
32. Cross LM, Cook MA, [...] and Rubinstein AL. 2003. Rapid analysis of angiogenesis drugs in a live fluorescent zebrafish assay. *Arterioscler Thromb Vasc Biol* 23(5):911-2.
33. de Boeck M, Cui C, [...] and Ten Dijke P. 2016. Smad6 determines BMP-regulated invasive behaviour of breast cancer cells in a zebrafish xenograft model. *Sci Rep* 6:24968.
34. Dixit A, Parnas O, [...] and Regev A. 2016. Perturb-Seq: dissecting molecular circuits with scalable single-cell RNA profiling of pooled genetic screens. *Cell* 167(7):1853-1866.

35. Drabsch Y, He S, [...] and Ten Dijke P. 2013. Transforming growth factor- β signalling controls human breast cancer metastasis in a zebrafish xenograft model. *Breast Cancer Res* 15(6):R106.
36. Echeverria GV, Powell E, [...] and Piwnica-Worms H. 2018. High-resolution clonal mapping of multi-organ metastasis in triple negative breast cancer. *Nat Commun* 9(1):5079.
37. Eguiara A, Holgado O, [...] and Martin AG. Xenografts in zebrafish embryos as a rapid functional assay for breast cancer stem-like cell identification. *Cell Cycle* 10(21):3751-7.
38. Ellenbroek SI and van Rheenen J. 2014. Imaging hallmarks of cancer in living mice. *Nat Rev Cancer* 14(6):406-18.
39. Ellett F, Pase L, [...] and Lieschke GJ. 2011. *mpeg1* promoter transgenes direct macrophage-lineage expression in zebrafish. *Blood* 117(4):e49-56
40. Elston CW and Ellis IO. 1991. Pathological prognostic factors in breast cancer. I. The value of histological grade in breast cancer: experience from a large study with long-term follow-up. *Histopathology* 19(5):403-10.
41. Falkowska-Hansen B, Kollar J, [...] and Kirschner M. 2010. An inducible Tet-Off-H2B-GFP lentiviral reporter vector for detection and in vivo isolation of label-retaining cells. *Exp Cell Res* 316(11):1885-95.
42. Faucherre A, Taylor GS, [...] and Hertog Jd. 2008. Zebrafish *pten* genes have overlapping and non-redundant functions in tumorigenesis and embryonic development. *Oncogene* 27(8):1079-86.
43. Fazio M, Ablain J, [...] and Zon LI. 2020. Zebrafish patient avatars in cancer biology and precision cancer therapy. *Nat Rev Cancer* 20(5):263-273. .
44. Feitsma H and Cuppen E. 2008. Zebrafish as a cancer model. *Mol Cancer Res* 6(5):685-94.
45. Fior R, Póvoa V, [...] and Ferreira MG. 2017. Single-cell functional and chemosensitive profiling of combinatorial colorectal therapy in zebrafish xenografts. *Proc Natl Acad Sci U S A* 114(39):E8234-E8243.
46. Fitzpatrick DJ, Lai CS, [...] and Walsh DC. 2014. Time to breast cancer relapse predicted by primary tumour characteristics, not lymph node involvement. *World J Surg* 38(7):1668-75.
47. Follain G, Osmani N, [...] and Goetz JG. 2018, Using the zebrafish embryo to dissect the early steps of the metastasis cascade. *Methods Mol Biol* 1749:195-211 – b.
48. Follain G, Osmani N, [...] and Goetz JG. 2018. Hemodynamic forces tune the arrest, adhesion, and extravasation of circulating tumor cells. *Dev Cell* 45(1):33-52.e12 – a.
49. Galluzzi L, Bravo-San Pedro JM, [...] and Kroemer G. 2017. Pharmacological modulation of autophagy: therapeutic potential and persisting obstacles. *Nat Rev Drug Discov* 16(7):487-511.
50. Gameiro PA and Struhl K. 2018. Nutrient deprivation elicits a transcriptional and translational inflammatory response coupled to decreased protein synthesis. *Cell Rep* 24(6):1415-1424.
51. Gansner JM, Dang M, Ammerman M and Zon LI. 2017. Transplantation in zebrafish. *Methods in Cell Biology* Volume 138, Pages 629-647.
52. Gao H, Chakraborty G, [...] and Giancotti FG. 2012. The BMP inhibitor Coco reactivates breast cancer cells at lung metastatic sites. *Cell* 150(4):764-79.
53. Gao H, Korn JM, [...] and Sellers WR. 2015. High-throughput screening using patient-derived tumor xenografts to predict clinical trial drug response. *Nat Med* 21(11):1318-25.

54. Gao T, Li JZ, [...] and Li LH. 2016. The mechanism between epithelial mesenchymal transition in breast cancer and hypoxia microenvironment. *Biomed Pharmacother* 80:393-405.
55. Geyer FC, Weigelt B, [...] and Reis-Filho JS. 2010. Molecular analysis reveals a genetic basis for the phenotypic diversity of metaplastic breast carcinomas. *J Pathol* 220(5):562-73.
56. Ghajar CM, Peinado H, [...] and Bissell MJ. 2013. The perivascular niche regulates breast tumour dormancy. *Nat Cell Biol* 15(7):807-17.
57. Gilkes DM, Semenza GL and Wirtz D. 2014. Hypoxia and the extracellular matrix: drivers of tumour metastasis. *Nat Rev Cancer* 14(6):430-9.
58. Giuliano AE, Edge SB and Hortobagyi GN. 2018. Eighth edition of the AJCC cancer Staging manual: breast cancer. *Ann Surg Oncol* 25(7):1783-1785.
59. Grange C, Lanzardo S, [...] and Bussolati B. 2008. Sca-1 identifies the tumor-initiating cells in mammary tumors of BALB-neuT transgenic mice. *Neoplasia* 10(12):1433-43.
60. Greene HSN. 1938. Heterologous transplantation of human and other mammalian tumors. *Science* 88, 357-358.
61. Greene HSN. 1941. Heterologous transplantation of mammalian TUMORS: II. The transfer of human tumors to ALIEN species. *The Journal of Experimental Medicine* 73, 475-486.
62. Guo B, Zhang Q, [...] and Tao K. 2018. KCNQ1OT1 promotes melanoma growth and metastasis. *Aging (Albany NY)* 10(4):632-644.
63. Guy CT, Cardiff RD and Muller WJ. 1992. Induction of mammary tumors by expression of polyomavirus middle T oncogene: a transgenic mouse model for metastatic disease. *Mol Cell Biol* 12(3):954-61.
64. Hai P, Imai T, [...] and Wang LV. 2019. High-throughput, label-free, single-cell photoacoustic microscopy of intratumoral metabolic heterogeneity. *Nat Biomed Eng* 3(5):381-391.
65. Haramis AP, Hurlstone A, [...] and Clevers HC. 2006. Adenomatous polyposis coli-deficient zebrafish are susceptible to digestive tract neoplasia. *EMBO Rep* 7(4):444-9.
66. Hason M and Bartůněk P. 2019. Zebrafish models of cancer-new insights on modeling human cancer in a non-mammalian vertebrate. *Genes* 10(11):935.
67. He S, Lamers GE, [...] and Snaar-Jagalska BE. 2012. Neutrophil-mediated experimental metastasis is enhanced by VEGFR inhibition in a zebrafish xenograft model. *J Pathol* 227(4):431-45.
68. Hidalgo M, Amant F, [...] and Villanueva A. 2014. Patient-derived xenograft models: an emerging platform for translational cancer research. *Cancer Discov* 4(9):998-1013.
69. Holmes C and Stanford WL. 2007. Concise review: stem cell antigen-1: expression, function, and enigma. *Stem Cells* 25(6):1339-47.
70. Howe K, Clark MD, [...] and Stemple DL. 2013. The zebrafish reference genome sequence and its relationship to the human genome. *Nature* 496(7446):498-503.
71. Howlader N, Noone AM, [...] and Cronin KA (eds). 2019. SEER Cancer Statistics Review, 1975-2016 National Cancer Institute. Bethesda, MD. *SEER website*: https://seer.cancer.gov/csr/1975_2016/.
72. Hwang WY, Fu Y, [...] and Joung JK. 2013. Efficient genome editing in zebrafish using a CRISPR-Cas system. *Nat Biotechnol* 31(3):227-9.
73. Ignatius MS, Hayes MN, [...] and Langenau DM. 2018. *tp53* deficiency causes a wide tumor spectrum and increases embryonal rhabdomyosarcoma metastasis in zebrafish. *Elife* 7:e37202.

74. Iorns E, Drews-Elger K, [...] and Lippman M. 2012. A new mouse model for the study of human breast cancer metastasis. *PLoS One* 7(10):e47995.
75. Isakoff SJ. 2010. Triple-negative breast cancer: role of specific chemotherapy agents. *Cancer J* 16(1):53-61.
76. Johnson JR, Hammond WG, Benfield JR and Tesluk H. 1995. Successful xenotransplantation of human lung cancer correlates with the metastatic phenotype. *Ann Thorac Surg* 60(1):32-6; discussion 36-7.
77. Juric D, Castel P, [...] and Scaltriti M. 2015. Convergent loss of PTEN leads to clinical resistance to a PI(3)K α inhibitor. *Nature* 518(7538):240-4.
78. Kalluri R and Weinberg RA. 2009. The basics of epithelial-mesenchymal transition. *J Clin Invest* 119(6):1420-8.
79. Kaur J and Debnath J. 2015. Autophagy at the crossroads of catabolism and anabolism. *Nat Rev Mol Cell Biol*, 16(8):461-72.
80. Keklikoglou I, Cianciaruso C, [...] and De Palma M. 2019. Chemotherapy elicits pro-metastatic extracellular vesicles in breast cancer models. *Nat Cell Biol* 21(2):190-202.
81. Keller PJ, Lin AF, [...] and Kuperwasser C. 2010. Mapping the cellular and molecular heterogeneity of normal and malignant breast tissues and cultured cell lines. *Breast Cancer Res* 12(5):R87.
82. Khanna C and Hunter K. 2005. Modeling metastasis in vivo. *Carcinogenesis* 26(3):513-23.
83. Kim JB, Urban K, [...] and Lassota P. 2010. Non-invasive detection of a small number of bioluminescent cancer cells in vivo. *PLoS One* 5(2):e9364.
84. Kimmel CB, Ballard WW, [...] and Schilling TF. 1995. Stages of embryonic development of the zebrafish. *Dev Dyn* 203(3):253-310.
85. Klein CA. 2009. Parallel progression of primary tumours and metastases. *Nat Rev Cancer* 9(4):302-12.
86. Köhler S, Ullrich S, Richter U, Schumacher U. 2010. E-/P-selectins and colon carcinoma metastasis: first in vivo evidence for their crucial role in a clinically relevant model of spontaneous metastasis formation in the lung. *Br J Cancer* 102(3):602-9.
87. Kretzschmar K and Watt FM. 2012. Lineage tracing. *Cell* 148(1-2):33-45
88. Kurrey NK, Jalgaonkar SP, [...] and Bapat SA. 2009. Snail and slug mediate radioresistance and chemoresistance by antagonizing p53-mediated apoptosis and acquiring a stem-like phenotype in ovarian cancer cells. *Stem Cells* 27(9):2059-68.
89. Labelle M, Begum S and Hynes RO. 2011. Direct signaling between platelets and cancer cells induces an epithelial-mesenchymal-like transition and promotes metastasis. *Cancer Cell* 20(5):576-90.
90. Lacunza E, Rabassa ME, [...] and Abba MC. 2014. Identification of signaling pathways modulated by RHBDD2 in breast cancer cells: a link to the unfolded protein response. *Cell Stress Chaperones* 19(3):379-88.
91. Lam SH and Gong Z. 2006. Modeling liver cancer using zebrafish: a comparative oncogenomics approach. *Cell Cycle* 5(6):573-7.
92. Lam SH, Chua HL, [...] and Sin YM. 2004. Development and maturation of the immune system in zebrafish, *Danio rerio*: a gene expression profiling, *in situ* hybridization and immunological study. *Dev Comp Immunol* 28(1):9-28.
93. Lambert AW, Pattabiraman DR and Weinberg RA. 2017. Emerging biological principles of metastasis. *Cell* 168(4):670-691.
94. Langenau DM, Keefe MD, [...] and Zon LI. 2007. Effects of RAS on the genesis of embryonal rhabdomyosarcoma. *Genes Dev* 21(11):1382-95.
95. Langenau DM, Traver D, [...] and Look AT. 2003. Myc-induced T cell leukemia in transgenic zebrafish. *Science* 299(5608):887-90.

96. Lawson ND and Weinstein BM. 2002. *In vivo* imaging of embryonic vascular development using transgenic zebrafish. *Dev Biol* 248(2):307-18.
97. Lee HJ, Seo AN, [...] and Park SY. 2014. HER2 heterogeneity affects trastuzumab responses and survival in patients with HER2-positive metastatic breast cancer. *Am J Clin Pathol* 142(6):755-66.
98. Lee LM, Seftor EA, [...] and Hendrix MJ. 2005. The fate of human malignant melanoma cells transplanted into zebrafish embryos: assessment of migration and cell division in the absence of tumor formation. *Dev Dyn* 233(4):1560-70.
99. Lee MP, DeBaun MR, [...] and Feinberg AP. 1999. Loss of imprinting of a paternally expressed transcript, with antisense orientation to KvLQT1, occurs frequently in Beckwith-Wiedemann syndrome and is independent of insulin-like growth factor II imprinting. *Proc Natl Acad Sci U S A* 96(9):5203-8.
100. Lee SL, Rouhi P, [...] and Cao Y. 2009. Hypoxia-induced pathological angiogenesis mediates tumor cell dissemination, invasion, and metastasis in a zebrafish tumor model. *Proc Natl Acad Sci U S A* 106(46):19485-90.
101. Li CI, Uribe DJ and Daling JR. 2005. Clinical characteristics of different histologic types of breast cancer. *Br J Cancer* 93(9):1046-52.
102. Lin J, Zhang W, [...] and Munshi NC. 2016. A clinically relevant *in vivo* zebrafish model of human multiple myeloma to study preclinical therapeutic efficacy. *Blood* 14;128(2):249-52.
103. Liu L, Yang L, [...] and Wang SE. 2018. Chemotherapy induces breast cancer stemness in association with dysregulated monocytosis. *Clin Cancer Res* 24(10):2370-2382.
104. Liu Z, Gu S, [...] and Zhou Y. 2020. IFI6 depletion inhibits esophageal squamous cell carcinoma progression through reactive oxygen species accumulation via mitochondrial dysfunction and endoplasmic reticulum stress. *J Exp Clin Cancer Res* 39(1):144.
105. Lüönd F, Tiede S and Christofori G. 2021. Breast cancer as an example of tumour heterogeneity and tumour cell plasticity during malignant progression. *Br J Cancer* 125(2):164-175.
106. Ma D, Zhang J, [...] and Handin RI. 2011. The identification and characterization of zebrafish hematopoietic stem cells. *Blood* 118(2):289-97.
107. Malandrino A, Kamm RD and Moeendarbary E. 2018. In vitro modeling of mechanics in cancer metastasis. *ACS Biomater Sci Eng* 4(2):294-301
108. Malaney P, Nicosia SV and Davé V. 2014. One mouse, one patient paradigm: new avatars of personalized cancer therapy. *Cancer Lett* 344(1):1-12.
109. Malhotra GK, Zhao X, Band H and Band V. 2010. Histological, molecular and functional subtypes of breast cancers. *Cancer Biol Ther* 10(10):955-60.
110. Mani SA, Guo W, [...] and Weinberg RA. 2008. The epithelial-mesenchymal transition generates cells with properties of stem cells. *Cell* 133(4):704-15.
111. Mar KB, Rinkenberger NR, [...] and Schoggins JW. 2018. LY6E mediates an evolutionarily conserved enhancement of virus infection by targeting a late entry step. *Nat Commun* 9(1):3603.
112. Marjon PL, Bobrovnikova-Marjon EV and Abcouwer SF. 2004. Expression of the pro-angiogenic factors vascular endothelial growth factor and interleukin-8/CXCL8 by human breast carcinomas is responsive to nutrient deprivation and endoplasmic reticulum stress. *Mol Cancer* 22;3:4.
113. Marques IJ, Weiss FU, [...] and Bagowski CP. 2009. Metastatic behaviour of primary human tumours in a zebrafish xenotransplantation model. *BMC Cancer* 9,128.
114. Martelotto LG, Ng CK, [...] and Reis-Filho JS. 2014. Breast cancer intra-tumor heterogeneity. *Breast Cancer Res* 16(3):210.

115. Massagué J and Obenauf AC. 2016. Metastatic colonization by circulating tumour cells. *Nature* 529(7586):298-306.
116. Mitsuya K, Meguro M, [...] and Oshimura M. 1999. LIT1, an imprinted antisense RNA in the human KvLQT1 locus identified by screening for differentially expressed transcripts using monochromosomal hybrids. *Hum Mol Genet* 8(7):1209-17.
117. Mroz EA and Rocco JW. 2017. The challenges of tumor genetic diversity. *Cancer* 123(6):917-927.
118. Nagelkerke A, Bussink J, [...] and Span PN. 2013. Hypoxia stimulates migration of breast cancer cells via the PERK/ATF4/LAMP3-arm of the unfolded protein response. *Breast Cancer Res* 15(1):R2.
119. Naxerova K and Jain RK. 2015. Using tumour phylogenetics to identify the roots of metastasis in humans. *Nat Rev Clin Oncol* 12(5):258-72.
120. Nguyen AT, Koh V, Spitsbergen JM and Gong Z. 2016. Development of a conditional liver tumor model by mifepristone-inducible Cre recombination to control oncogenic kras V12 expression in transgenic zebrafish. *Sci Rep* 6:19559.
121. Nguyen-Chi M, Laplace-Builhe B, and [...] and Djouad F. 2015. Identification of polarized macrophage subsets in zebrafish. *Elife* 4:e07288.
122. Nguyen DX, Bos PD and Massagué J. 2009. Metastasis: from dissemination to organ-specific colonization. *Nat Rev Cancer*, 9(4):274-84.
123. Nicoli S and Presta M. 2007. The zebrafish/tumor xenograft angiogenesis assay. *Nat Protoc* 2(11):2918-23.
124. Nicoli S, Ribatti D, Cotelli F and Presta M. 2007. Mammalian tumor xenografts induce neovascularization in zebrafish embryos. *Cancer Res* 67(7):2927-31.
125. Nowell PC. 1976. The clonal evolution of tumor cell populations. *Science* 194(4260):23-8.
126. Padua D, Zhang XH, [...] and Massagué J. 2008. TGFbeta primes breast tumors for lung metastasis seeding through angiopoietin-like 4. *Cell* 133(1):66-77.
127. Palumbo JS, Talmage KE, [...] and Degen JL. 2007. Tumor cell-associated tissue factor and circulating hemostatic factors cooperate to increase metastatic potential through natural killer cell-dependent and-independent mechanisms. *Blood* 110(1):133-41.
128. Panagiotou G, Ghaly W, [...] and Mantzoros CS. 2021. Serum Follistatin is increased in thyroid cancer and is associated with adverse tumor characteristics in humans. *J Clin Endocrinol Metab* 106(5):e2137-e2150.
129. Pandey RR, Mondal T, [...] and Kanduri C. 2008. Kcnq1ot1 antisense noncoding RNA mediates lineage-specific transcriptional silencing through chromatin-level regulation. *Mol Cell* 32(2):232-46.
130. Patani N, Barbashina V, [...] and Reis-Filho JS. 2011. Direct evidence for concurrent morphological and genetic heterogeneity in an invasive ductal carcinoma of triple-negative phenotype. *J Clin Pathol* 64(9):822-8.
131. Patton EE, Widlund HR, [...] and Zon LI. 2005. BRAF mutations are sufficient to promote nevi formation and cooperate with p53 in the genesis of melanoma. *Curr Biol* 15(3):249-54.
132. Patton EE, Zon LI and Langenau DM. 2021. Zebrafish disease models in drug discovery: from preclinical modelling to clinical trials. *Nat Rev Drug Discov* 20(8):611-628.
133. Paul CD, Bishop K, [...] and Tanner K. 2019. Tissue architectural cues drive organ targeting of tumor cells in zebrafish. *Cell Syst* 9(2):187-206.e16.
134. Phillips JB and Westerfield M. 2014. Zebrafish models in translational research: tipping the scales toward advancements in human health. *Dis Model Mech* 7(7):739-43.

135. Polyak K and Marusyk A. 2014. Cancer: clonal cooperation. *Nature* 508(7494):52-3.
136. Pouliot N, Pearson HB and Burrows A. 2013. Investigating metastasis using in vitro platforms. In: *Madame Curie Bioscience Database*. Austin (TX): Landes Bioscience.
137. Póvoa V, Rebelo de Almeida C, [...] and Fior R. 2021. Innate immune evasion revealed in a colorectal zebrafish xenograft model. *Nat Commun* 12(1):1156.
138. Prat A, Parker JS, [...] and Perou CM. 2010. Phenotypic and molecular characterization of the claudin-low intrinsic subtype of breast cancer. *Breast Cancer Res* 12(5):R68.
139. Pruvot B, Jacquelin A, [...] and Solary E. 2011. Leukemic cell xenograft in zebrafish embryo for investigating drug efficacy. *Haematologica*, 96(4):612-6.
140. Pype C, Verbueken E, [...] and Van Cruchten SJ. 2015. Incubation at 32.5°C and above causes malformations in the zebrafish embryo. *Reprod Toxicol* 56:56-63.
141. Qian BZ, Li J, [...] and Pollard JW. 2011. CCL2 recruits inflammatory monocytes to facilitate breast-tumour metastasis. *Nature* 475(7355):222-5.
142. Rebelo de Almeida C, Mendes RV, [...] and Fior R. 2020. Zebrafish xenografts as a fast screening platform for bevacizumab cancer therapy. *Commun Biol* 3(1):299.
143. Ren J, Liu S, Cui C and Ten Dijke P. 2017. Invasive behavior of human breast cancer cells in embryonic zebrafish. *J Vis Exp* (122):55459 – a.
144. Ren K, Xu R, [...] and Shi W. 2017. Knockdown of long non-coding RNA KCNQ1OT1 depressed chemoresistance to paclitaxel in lung adenocarcinoma. *Cancer Chemother Pharmacol* 80(2):243-250 – b.
145. Renaud O, Herbomel P, Kissa K. 2011. Studying cell behavior in whole zebrafish embryos by confocal live imaging: application to hematopoietic stem cells. *Nat Protoc* 6(12):1897-904.
146. Renshaw SA, Loynes CA, [...] and Whyte MK. 2006. A transgenic zebrafish model of neutrophilic inflammation. *Blood* 108(13):3976-8.
147. Reymond N, d'Água BB and Ridley AJ. 2013. Crossing the endothelial barrier during metastasis. *Nat Rev Cancer* 13(12):858-70.
148. Risom T, Langer EM, [...] and Sears RC. 2018. Differentiation-state plasticity is a targetable resistance mechanism in basal-like breast cancer. *Nat Commun* 9(1):3815.
149. Ritsma L, Steller EJ, [...] and van Rheenen J. 2012. Intravital microscopy through an abdominal imaging window reveals a pre-micrometastasis stage during liver metastasis. *Sci Transl Med* 4(158):158ra145.
150. Roh-Johnson M, Shah AN, [...] and Moens CB. 2017. Macrophage-dependent cytoplasmic transfer during melanoma invasion *in vivo*. *Dev Cell* 43(5):549-562.
151. Rosen JN, Sweeney MF and Mably JD. 2009. Microinjection of zebrafish embryos to analyze gene function. *J Vis Exp* 9(25):1115.
152. Ruan S, Lin M, [...] and Li Q. 2020. Integrin β 4-targeted cancer immunotherapies inhibit tumor growth and decrease metastasis. *Cancer Res* 80(4):771-783.
153. Sacco A, Roccaro AM, [...] and Ghobrial IM. 2016. Cancer cell dissemination and homing to the bone marrow in a zebrafish model. *Cancer Res* 76(2):463-71.
154. Sadeghi M, Ordway B, [...] and Damaghi M. 2020. Integrative Analysis of breast cancer cells reveals an epithelial-mesenchymal transition role in adaptation to acidic microenvironment. *Front Oncol* 10:304.

155. Schreiber RD, Old LJ and Smyth MJ. 2011. Cancer immunoediting: integrating immunity's roles in cancer suppression and promotion. *Science* 25;331(6024):1565-70.
156. Schumacher D, Strilic B, [...] and Offermanns S. 2013. Platelet-derived nucleotides promote tumor-cell transendothelial migration and metastasis via P2Y2 receptor. *Cancer Cell* 24(1):130-7.
157. Seachrist DD, Sizemore ST, [...] and Keri RA. 2017. Follistatin is a metastasis suppressor in a mouse model of HER2-positive breast cancer. *Breast Cancer Res* 19(1):66.
158. Semenza GL. 2003. Targeting HIF-1 for cancer therapy. *Nat Rev Cancer* 3(10):721-32.
159. Shiozawa Y, Eber MR, Berry JE, Taichman RS. 2015. Bone marrow as a metastatic niche for disseminated tumor cells from solid tumors. *Bonekey Rep* 4:689.
160. Siegel RL, Miller KD and Jemal A. 2020 Cancer statistics, 2020. *CA Cancer J Clin* 70(1):7-30.
161. Soni A, Ren Z, [...] and Wei S. 2015. Breast cancer subtypes predispose the site of distant metastases. *Am J Clin Pathol* 143(4):471-8.
162. Spicer JD, McDonald B, [...] and Ferri LE. 2012. Neutrophils promote liver metastasis via Mac-1-mediated interactions with circulating tumor cells. *Cancer Res* 72(16):3919-27.
163. Spiegel A, Brooks MW, [...] and Weinberg RA. 2016. Neutrophils suppress intraluminal NK cell-mediated tumor cell clearance and enhance extravasation of disseminated carcinoma cells. *Cancer Discov* 6(6):630-49.
164. Sprooten J and Garg AD. 2020. Type I interferons and endoplasmic reticulum stress in health and disease. *Int Rev Cell Mol Biol*, 350:63-118.
165. Stewart RL and O'Connor KL. 2015. Clinical significance of the integrin $\alpha 6\beta 4$ in human malignancies. *Lab Invest* 95(9):976-86.
166. Stoletov K and Klemke R. 2008. Catch of the day: zebrafish as a human cancer model. *Oncogene* 27(33):4509-20.
167. Stoletov K, Montel V, [...] and Klemke R. 2007. High-resolution imaging of the dynamic tumor cell vascular interface in transparent zebrafish. *Proc Natl Acad Sci U S A* 30;104(44).
168. Streisinger G, Walker C, [...] and Singer F. 1981. Production of clones of homozygous diploid zebra fish (*Brachydanio rerio*). *Nature* 291, 293–296.
169. Subik K, Lee JF, [...] and Tang P. 2010. The expression patterns of ER, PR, HER2, CK5/6, EGFR, Ki-67 and AR by immunohistochemical analysis in breast cancer cell lines. *Breast Cancer (Auckl)*, 4:35-41. Erratum in: *Breast Cancer (Auckl)*, 2018, 12:1178223418806626.
170. Tahara E Jr, Tahara H, [...] and Tahara E. 2005. G1P3, an interferon inducible gene 6-16, is expressed in gastric cancers and inhibits mitochondrial-mediated apoptosis in gastric cancer cell line TMK-1 cell. *Cancer Immunol Immunother* 54(8):729-40.
171. Torre LA, Islami F, [...] and Jemal A. 2017. Global cancer in women: burden and trends. *Cancer Epidemiol Biomarkers Prev* 26(4):444-457.
172. Traver D, Winzeler A, [...] and Zon LI. 2004. Effects of lethal irradiation in zebrafish and rescue by hematopoietic cell transplantation. *Blood* 104(5):1298-305.
173. Trede NS, Langenau DM, [...] and Zon LI. 2004. The use of zebrafish to understand immunity. *Immunity* 20(4):367-79.
174. Tsuchida K, Nakatani M, [...] and Inokuchi K. 2009. Activin signaling as an emerging target for therapeutic interventions. *Cell Commun Signal* 7:15.
175. Tulotta C, Stefanescu C, [...] and Snaar-Jagalska BE. Inhibition of signaling between human CXCR4 and zebrafish ligands by the small molecule IT1t impairs

- the formation of triple-negative breast cancer early metastases in a zebrafish xenograft model. 2016. *Dis Model Mech* 9(2):141-53.
176. Usai A, Di Franco G, [...] and Raffa V. 2020. A model of a zebrafish avatar for co-clinical trials. *Cancers* 12(3):677.
 177. Varanda AB, Martins-Logrado A, Ferreira MG and Fior R. 2020. Zebrafish xenografts unveil sensitivity to olaparib beyond BRCA status. *Cancers* 12(7):1769.
 178. Vargas R, Gopal P, [...] and Abazeed ME. 2018. Case study: patient-derived clear cell adenocarcinoma xenograft model longitudinally predicts treatment response. *NPJ Precis Oncol* 2:14.
 179. Vaupel P, Mayer A, Briest S and Höckel M. 2005. Hypoxia in breast cancer: role of blood flow, oxygen diffusion distances, and anemia in the development of oxygen depletion. *Adv Exp Med Biol* 566:333-42.
 180. Vlashi E, Lagadec C, [...] and Pajonk F. 2014. Metabolic differences in breast cancer stem cells and differentiated progeny. *Breast Cancer Res Treat* 146(3):525-34.
 181. Volk-Draper L, Hall K, [...] and Ran S. 2014. Paclitaxel therapy promotes breast cancer metastasis in a TLR4-dependent manner. *Cancer Res* 74(19):5421-34.
 182. Wagner DE and Klein AM. 2020. Lineage tracing meets single-cell omics: opportunities and challenges. *Nat Rev Genet* 21(7):410-427.
 183. White E. 2012. Deconvoluting the context-dependent role for autophagy in cancer. *Nat Rev Cancer* 12(6):401-10.
 184. White R, Rose K and Zon L. 2013. Zebrafish cancer: the state of the art and the path forward. *Nat Rev Cancer* 13(9):624-36.
 185. White RM, Sessa A, [...] and Zon LI. 2008. Transparent adult zebrafish as a tool for in vivo transplantation analysis. *Cell Stem Cell* 2(2):183-9.
 186. Wu JQ, Zhai J, [...] and He MF. 2017. Patient-derived xenograft in zebrafish embryos: a new platform for translational research in gastric cancer. *J Exp Clin Cancer Res* 36(1):160.
 187. Xue Y, Lv J, [...] and Liu F. 2017. The vascular niche regulates hematopoietic stem and progenitor cell lodgment and expansion via klf6a-cc125b. *Dev Cell* 42(4):349-362.e4.
 188. Yan C, Brunson DC, [...] and Langenau DM. 2019. Visualizing engrafted human cancer and therapy responses in immunodeficient zebrafish. *Cell* 177(7):1903-1914.
 189. Yang H, Xu Z, [...] and Xiang Y. 2021. Integrin β 4 as a potential diagnostic and therapeutic tumor marker. *Biomolecules* 11(8):1197.
 190. Yang HW, Kutok JL, [...] and Look AT. 2004. Targeted expression of human MYCN selectively causes pancreatic neuroendocrine tumors in transgenic zebrafish. *Cancer Res* 64(20):7256-62.
 191. Yeo SK and Guan JL. 2017. Breast cancer: multiple subtypes within a tumor? *Trends Cancer* 3(11):753-760.
 192. Zhang H, Wong CC, [...] and Semenza GL. 2012. HIF-1-dependent expression of angiopoietin-like 4 and L1CAM mediates vascular metastasis of hypoxic breast cancer cells to the lungs. *Oncogene* 31(14):1757-70.
 193. Zhang K, Yan J, [...] and Hu H. 2019. High KCNQ1OT1 expression might independently predict shorter survival of colon adenocarcinoma. *Future Oncol* 15(10):1085-1095.